Effect of Surface Wettability, Morphology and Chemistry on the Biocompatibility of Laser Textured Titanium Surfaces

by

Xun Zhao

Thesis submitted to the University of Ottawa

In partial fulfillment of the requirements for the

MASTER OF APPLIED SCIENCE

Advanced Materials and Manufacturing

Faculty of Engineering

University of Ottawa

© Xun Zhao, Ottawa, Canada, 2021

Abstract

Titanium has been used in bio-medical implants for decades due to its superior biocompatibility. To improve the osseointegration of dental and orthopaedic implants, various surface modification techniques have been used including laser surface texturing. In particular, short-pulsed lasers, such as femtosecond and picosecond lasers, are widely used for surface modification.

In this thesis, commercially pure Ti surfaces are modified by a femtosecond laser to explore the relationship between surface topography, surface chemistry, surface wettability, and biocompatibility with the goal of improving the osseointegration of implants. The laser textured surfaces consist of 1μm wide grooves spaced 10 μm, 4.8 μm, 2.4 μm and 1.2 μm apart. Gradient configurations where the groove spacing varies are also investigated. Surface morphology was characterized using Optical Microscopy (OM), Scanning Electron Microscopy (SEM) and Atomic Force Microscopy (AFM).

A custom-build contact angle measurement apparatus is used to investigate the wettability of the laser textured surfaces using the sessile drop method. Freshly laser-treated commercially pure Ti surfaces are found to be super-hydrophilic and become hydrophobic over time when exposed to air. The presence of grooves can accelerate the evolution of the contact angle over time, and introduces anisotropy in the wetting behavior (along vs. across the grooves). The hydrophilicity of laser treated surfaces can be retained by storing samples in ethanol.

X-ray Photoelectron Spectroscopy (XPS) shows that the relative carbon content increases over time when Ti samples are exposed to air, which results in the subsequent evolution of the contact angle and cell response to laser textured Ti surfaces. Besides, laser treatment promotes the oxidation of pure Ti, and the product, TiO_2, is responsible for the better biocompatibility.

In vitro experiments using MG 63s osteoblast-like cells are implemented on laser-treated Ti surfaces and polished surfaces (control) with 1 day, 3 days and 7 days of cell culture. The best cell outcome was obtained by storing samples in air for 1 week, where storing for shorter or longer times resulted in the worst outcome, especially in the early stages of cell adhesion. There does not appear to be a direct link between wettability and the fate of cells on Ti

surfaces.

Indeed, while samples stored in air and ethanol have drastically different contact angle measurements (the former being hydrophobic and the latter hydrophilic), the cell behavior was unaffected.

In addition, while wettability and laser treatment can affect the early stages of cell adhesion, they do not have a strong effect on the number of cells at longer incubation times (3 and 7 days). Laser machining does however affect the cell morphology and alignment, where cells preferentially align themselves parallel to the direction of the laser machined grooves with an elongated morphology.

Keywords: Femtosecond laser texturing, Commercially pure titanium, Bio-implants, Surface Wettability, Biocompatibility, Osseointegration

Acknowledgement:

First of all, I would like to thank my supervisor Professor Arnaud Weck for his patient guidance and encouragement which give me confidence in pursuing my ideas and overcoming difficulties in master's studies.

I would like to thank my collaborators Dr. Fabio Variola and Dr. Alexandre Steeves from Surface Nanoengineering Lab (SNL), University of Ottawa, for their support in biological experiments and assisting me in analysis.

I want to thank all my colleagues at Fracture and Femtosecond Research Ottawa Group (FROG), especially, Xitong Xie and Katerina Luiza Monea, for their help in solving problems with devices and giving me advice when I faced problems.

Lastly, I am very thankful to my boyfriend, Wenchao Ruan, and my family for support and understanding throughout the master's life. And a great thanks to all my friends in Ottawa, especially my roommate, Siyuan Shen.

Table of Contents

List of Figures

List of Tables

List of Abbreviations

AES	Auger Electron Spectroscopy
AFM	Atomic Force Microscopy
BBO	Beta barium borate
BCC	Body-centered cubic structure
BIC	Bone-to-implant contact
BSC	Biological safety cabinet
CB	Cassie-Baxter
CCM	Complete culturing media
Cp	Commercial pure
CW	Continuous wave
DMEM	Dulbecco's modified eagle media
EDM	Electrical discharge machining
FBS	Fetal bovine serum
Fs	Femtosecond
FWHM	Full width at half maximum
HAZ	Heat affected zone
HCP	Hexagonal closed packed crystal structure
HFLS	High spatial frequency LIPSS
LIPSS	Laser induced periodic surface structure
Ns	Nanosecond
OM	Optical Microscopy
OPS	Colloidal silica suspension
PBS	Phosphate buffered saline solution
Ps	Picosecond
ROI	Regions of interest
SAMs	Self-assembled monolayers
SBF	Simulated body fluid
SEM	Scanning Electron Microscopy

Ti	Titanium
UV	Ultraviolet
XPS	X-ray Photoelectron Spectroscopy

1. Introduction

1.1 Background

Advanced technologies promote the development of surgical implants and the extension of their service life to improve the quality of patients' lives. The market demand for implants is growing rapidly due to the aging population, more bad habits and accidents [1][2]. Due to the considerable progress achieved in recent years, the lifespan of dental and orthopaedic implants is more than 15 years, but it still limited and depends on individual and the type of implants [3]. For dental implants, several studies indicate that the long-term survival of dental implants is up to 20-year span [4]. As for the knee and hip implants, studies show that the implants can be expected to function well at least 15-20 years in more than 75% to 85% of patients [5][6]. However, some implants can fail at some point. The common causes of implant failure are inflammation, infection, allergy, corrosion, wear, fatigue, and the lack of osseointegration, which is the most concerning for researchers [3]. Osseointegration is experimentally defined as the close contact between bone and implant material in the histological section, and clinically defined as the stability and rigidity of the implant in the bone (joint fusion) [7]. The failure of the implant surface to integrate with bone or tissue may lead to micromotion, which eventually results in the loosening of implants.

Due to the current limitations of implants and the growing market demand, osseointegration-related research is required. According to previous research, cell behavior can be improved by endowing the surfaces of implants with new features, since cells can recognize and respond to nano- or micro-scale features by changing morphology and behavior [5][6]. Currently, research developments of biomaterials focus on cell-targeted surface modification techniques that mimic extracellular environments to control cell behaviors, such as attachment, growth, migration, proliferation and differentiation. The aim of these techniques is to tune the surface topography and chemical composition of implant surfaces in order to promote controlled, targeted and rapid healing, thus improving the performance and longevity of implants [10].

Nowadays, commonly used surface modification techniques are plasma spraying, grit blasting, acid etching and photolithography, to name a few. These techniques suffer from surface contamination and often modify the structure and properties of the implant material [8][9]. Some of these techniques are also too expensive to be implemented in an industrial process. Conversely, the femtosecond laser surface direct writing technique has emerged as a simple, high resolution, controlled, reproducible, contactless, fast and single-step method that has been applied on a wide class of materials including metals, polymers, ceramics, and composites [13]. Titanium has been widely used in biomedical, aerospace and other industries due to its high biocompatibility, corrosion resistance and strength to weight ratio [3][4].

1.2 Research objectives

The main goals of this thesis are to explore the possibility and reproducibility of micro-scale surface features generated by femtosecond laser on commercially pure Ti surfaces and the effect of surface topography and chemistry on surface wettability and cell behavior. The specific research objectives of this thesis are listed below:

1. Generating micro-scale surface features by laser surface texturing on cp Ti surfaces and comparing their microstructure.
2. Controlling the laser process parameters to create different surface roughness.
3. Investigating the effect of surface morphology and chemistry on surface wettability and cell response.
4. Investigating the effect of storage conditions and time on surface chemistry, wettability and cell adhesion.
5. Exploring the relationship between surface chemistry, wettability, and cell adhesion.

1.3 Organization of the thesis

Chapter I is an introduction to the field of dental and orthopedic implants highlighting recent innovative developments to improve the performance and longevity of implants.

In chapter II, a detailed literature review is presented that includes work on biomaterials selection, biomaterials requirements and limitations, surface modification methods,

femtosecond laser surface direct writing technique, surface wettability and dynamics of cell-biomaterials interaction.

In chapter III, the design of all experiments including laser surface texturing, contact angle measurements, and cell culture procedures are described. The methods for characterizing surface morphology, roughness, and wettability, as well as cell behavior are explained.

In chapter IV, the experimental results are presented, and the relationship between surface topography, surface chemistry, surface wettability and cell response are discussed.

In chapter V, a conclusion from the research is drawn from the experimental results and discussion in chapter IV.

In chapter VI, some suggestions for future work are summarized and provided.

1.4 Contribution

The main purpose of this thesis is to evaluate the potential of periodic surface structures with uniform grooves and gradients on commercially pure Ti surfaces to improve the osseointegration of dental and orthopedic implants. The transition of surface wetting behavior from hydrophilicity to hydrophobicity was induced by absorption of carbon from the air over time. Laser treatment promoted the oxidation of cp Ti while storage in ethanol slowed down the oxidation process. Surface roughness and wettability were shown to be affected by cell adhesion on laser treated surfaces, but the competing phenomena, i.e. carbon contamination and TiO_2 formation, led to the fluctuation in contact angle and number of adhered cells over time. Moreover, the laser treatment reduced the number of adhered cells compared to polished surfaces.

2. Literature Review

2.1 Biomaterials for dental and orthopaedic implants

A given material needs to fulfil many requirements to be considered as a suitable in the body for implantation. It is important to realize that no one material can meet all these requirements. There are two main factors that affect the biocompatibility of biomaterials: the host response, induced by the implant material, and the degradation of biomaterial in the body [3][14]. Biomaterials are mainly divided into four general classes, which are metal, polymer, ceramic, and composites. Depending on the interaction between the biomaterial and the surrounding tissues, the biomaterials can be classified as bio-tolerant (no negative immune response from the body), bio-active (promote cells adhesion, proliferation and bone growth) and bio-absorbable (resorbs in the body as new bone is growing) [3].

2.1.1 Metallic materials

Metal was the material of choice in the past to replace damaged bone due to its strength and toughness. Pure metals are sometimes used, but their mechanical properties limit their use in applications where high strength is required. Therefore, alloys (metals containing two or more elements) provide better mechanical properties such as strength, corrosion resistance and toughness [15]. The main and most dangerous problem of using these alloys is the release of ions which may be toxic to human tissues. The criteria for selecting pure metals and alloys are their biocompatibility, mechanical properties, corrosion resistance, toughness and cost [3][4].

Currently, the main metallic biomaterials used in the biomedical field are cobalt chromium alloy (CoCrMo), titanium (Ti) and its alloys, 316L stainless steel, gallium (Ga), and tantalum (Ta), which dominate many biomedical implants applications [16]. However, some metals have proved to have lower success rates over time, and these materials are now obsolete. For example, Plecko et al. indicated that the osseointegration of cobalt-chromium and stainless steel is lower than that of other metals [17]. Gallium is a group III metal that is known to interact with hydroxyapatite and the cellular components of bone [18]. Bockman et al. showed that Ga can hinder bone resorption to a certain extent [18].

2.1.2 Non-metallic materials

Polymers used as biomaterials have been investigated by many researchers due to their excellent mechanical properties, decent corrosion and wear resistance and long-term non-toxicity and stability. Among them, poly-ether-ether-ketone (PEEK) has been already used to replace metallic implants in orthopedics [19]–[21] and traumatology [22]. However, PEEK is biologically inert, which is not conducive to cell adhesion [23]. The easiest and most effective way to solve this problem is to coat PEEK surfaces with bioactive elements. A Ti coating was added on a PEEK surface to improve the biocompatibility. The initial cell attachment, cell growth and spread all improved compared to the pure PEEK substrate, where the level of in vitro cellular responses more than doubled after Ti was coated onto the PEEK substrate, as shown in Figure 2-1 [24].

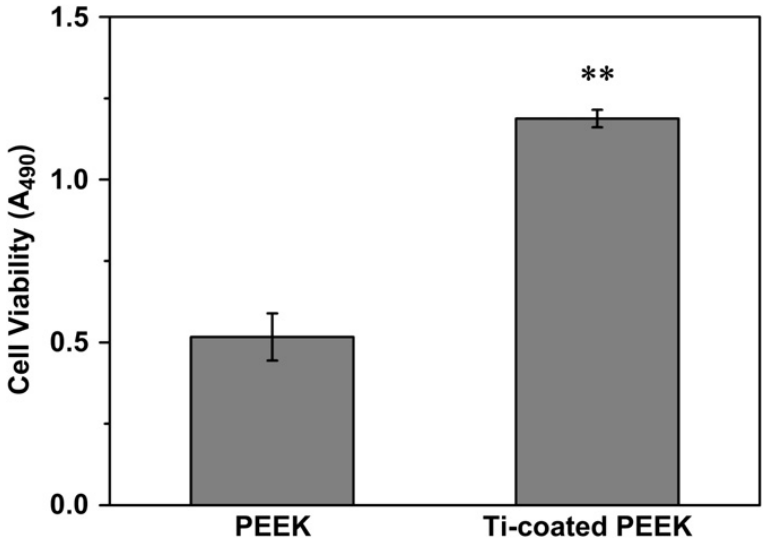

Figure 2-1 Cell viability of the MC3T3-E1 cells cultured on bare and Ti-coated PEEK for 5 days [24].

Another class of biomaterials, ceramics, are commonly used to repair or replace bone or tissue. Their success is attributed to their stable attachment to connective tissue. The mechanism of tissue attachment depends on the tissue response between the tissue and the implant interface [25]. Bio-ceramics are suitable because of their structure, which is composed of ions. These ions can be found in the physiological environment and have limited toxicity to human tissues [25]. Ceramic materials have been used as dental implants for decades. Currently, the commonly used material is yttria-stabilized tetragonal zirconia due to its excellent mechanical and tribological properties, and biocompatibility. However,

researchers are still worried about the long-term durability of this material because of some reports of in vivo failure caused by the low-temperature degradation of zirconia. To solve this problem, Mussano et al. [25] have developed improved oxide-based materials, alumina-toughened zirconia (ATZ) and zirconia-toughened alumina (ZTA) to evaluate the influence of surface roughness on biological response. The osteogenesis of MC3T3 cells was enhanced when the surfaces were rough treated by phosphoric acid under hydrothermal conditions, as shown in Figure 2-2.

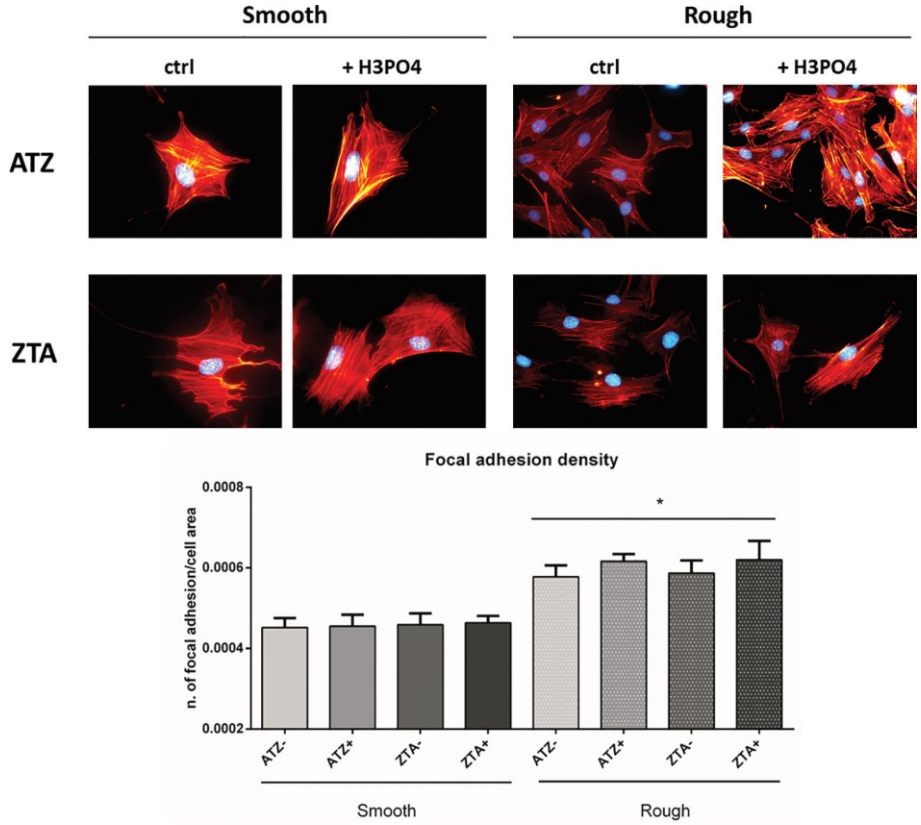

Figure 2-2 MC3T3 cell morphology and quantification of focal adhesion density on different surfaces of ATZ and ZTA [25].

2.1.3 Essential requirements for orthopedic and dental implants

There are some essential requirements when materials are used as orthopedic and dental implants. The most important one is biocompatibility, and the success rate of osseointegration plays an important role. In addition, appropriate mechanical properties, high corrosion and fatigue resistance are necessary.

2.1.3.1 Mechanical properties

As a replacement for human bone, the implant materials should meet the general requirements of strength, hardness and ductility [26]. It is expected that the materials for replacing human bone has a Young's modulus similar to that of human bone. The Young's modulus of human bone is ranging from 4 to 30 GPa depending on the type of bone, its working position and the measurement direction [27]. Besides, to achieve long-term success or long service lifetimes, implants are expected to have a high fatigue strength in order to endure repeated periodic loads or strains commonly found when chewing, walking and running. The phenomenon where implants fail due to poor strength and mechanical properties or mismatch between implants and bone is referred to bio-mechanical incompatibility.

Current implant materials have higher stiffness than human bones, thereby preventing the required stress from being transmitted to adjacent bones, which may cause bone resorption around implants and further cause the loosening of implants [26][27]. This bio-mechanical incompatibility resulting in bone resorption is called the stress shielding effect. Therefore, the materials with an excellent combination of high strength, low Young's modulus (closer to that of human bone) and high fatigue strength can be used to avoid any loosening of implants, which needs further exploration.

2.1.3.2 Corrosion and wear resistance

As implants are used in the body for a long time, high corrosion resistance and wear resistance are necessary [2]. The lifetime of an implant is determined by its corrosion and wear resistance performances. Metal ions, or metallic fragments from implant materials can be released due to the interactions between implants with low resistance to corrosion and wear and body fluid, which causes allergic or toxic reaction and removal of implants [30]. Therefore, implant materials surfaces need to acquire high wear and corrosion resistance to avoid allergic or toxic reactions and provide a safe usage.

2.1.3.3 Biocompatibility

Biocompatibility has been defined as " the ability of a material to perform with an appropriate host response in a specific environment" [31]. It is expected that materials used as

implants are highly non-toxic, non-carcinogenic, and will not cause any inflammation or allergic reactions in the human body that may lead to cell death or impaired cell and tissue function [32]. The success of biomaterials mainly depends on the human body's responses to implants, which determines the biocompatibility of materials [33].

2.1.3.4 Osseointegration

Osseointegration is defined as "the direct structural and functional contact between ordered, living bone and the surface of the load-carrying implant, without intervening soft tissue" by Per-Ingvar Branemark [34]. The degree of integration between implants and surrounding bone determines the outcome of implant surgeries [1]. A higher degree of osseointegration allows for higher mechanical stability and lower probability of implant loosening and failure. In contrast to fibrous cysts, bone formation on the surface of implants is considered as a positive outcome. From a physicochemical point of view, osseointegration is considered to be the results of reactions to foreign bodies. Surgical trauma caused by implantation may cause severe oxidation stress, leading to excessive production and attachment of free radicals and oxidized derivatives on implant surfaces, which results in thickening of the oxide layer [35]. The adhesion of cells to implant surfaces and the reduction of micro-movements are critical to successful osseointegration and are affected by physicochemical properties and micro- and nano-scale topography [35].

2.2 Titanium and its alloys

Titanium has been regarded as one of the most important metal in the biomedical industry for many years. Over the past two decades, the implant manufacturing techniques for titanium and its alloys have matured more than for other structural materials.

Titanium exists in two allotropic forms. At lower temperature, it has a hexagonal closed packed crystal structure (HCP), which is usually called the α-phase. At the temperature of 882.5°C, it has a body-centered cubic structure (BCC), β-phase. The α to β transformation temperature of pure Ti is controlled by the addition of other alloying elements. Alloying elements, such as Al, O, N, C, tend to stabilize the α-phase, which are called α stabilizers. The addition of these elements can increase the transition temperature of the β-phase. Elements

like V, Mo, Nb, Ta, Fe, Cr, W, Si, Co, Mn and H are known as β stabilizers, where the addition of such elements can decrease the transition temperature of the β-phase.

2.2.1 Biomedical application of pure Ti and its alloys

Cp Ti is favored as a biomedical implant material due to the limited content of other elements that may cause an immune response of the human body and more tissue ingrowths and high corrosion resistance compared with stainless steel, but its usage in medical applications is confined because of lower strength and unfavorable wear resistance [36]. Therefore, many researchers focused on synthesizing Ti alloys by adding alloying elements to change its microstructure and properties. In the 1970s, a specific Ti alloy, Ti6Al4V, was used in dental implants due to its better tissue tolerance, high strength and superior corrosion resistance [36]. However, more debris was found in the human body after implantation due to poor wear resistance unless proper surface treatment was applied [37]. In order to replace the V in titanium alloys to reduce toxicity, Nb was added in Ti alloys to form Ti6Al7Nb. Cui et al. [38] tested the mechanical properties of Ti6Al7Nb alloy using tensile tests and hot compression tests. When the Ti6Al7Nb was hot deformed at around 750-850°C, the phases recrystallized with a strain rate of less than 1 s^{-1}. Lee et al. demonstrated that Ti6Al7Nb alloys had excellent deformability and higher resistance to flow [39]. Currently, titanium alloys with different chemical compositions with low toxicity, long-term stability, low elastic modulus and a strength matching that of human bones are being explored [27][37][38].

Though Ti implants have high osseointegration rates, proper contact between bone and implant surfaces usually takes at least 3 weeks after implantation. Therefore, Ti and its alloys are now being developed to decrease time for osseointegration. Lijian et al. deduced an interaction mechanism between cp Ti implant surfaces and bone at the anatomic and molecular level, as shown in Figure 2-3 [42]. Region (a) shows the contact area between the periosteal layer and the implant surface, region (b) shows the clear association between the tissue and the implant surface, and region (c) shows the bone marrow [43]. From the investigation, it is concluded that there is both physical and chemical integration occurring between titanium and bone after implantation, and cannot be decoupled.

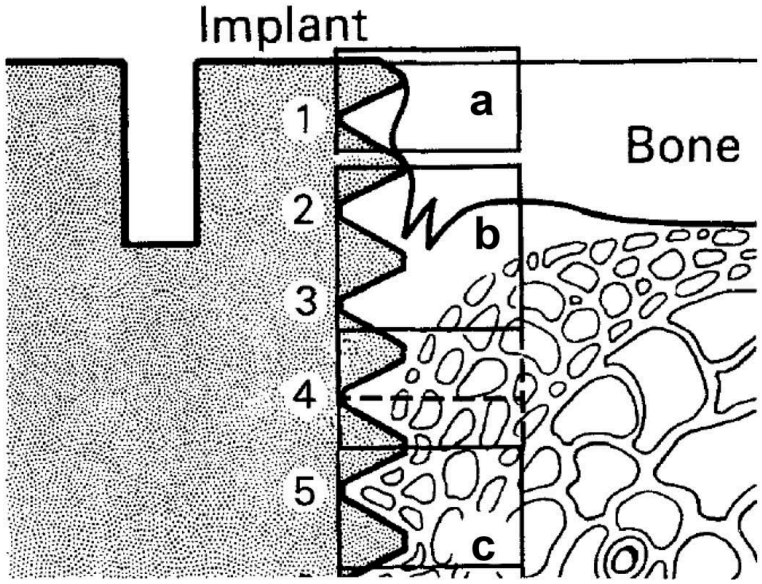

Figure 2-3 Scheme of bone tissue interaction with Ti implant surface [43].

Development of new Ti alloys by adding alloying elements like zirconium (Zr), tantalum (Ta), niobium (Nb) and nickel (Ni) focuses on obtaining better biocompatibility. For example, TiNb alloys have a higher corrosion resistance compared with cp Ti in fluorine-containing and fluorine-free solutions [42][43]. NiTi alloy was shown to have lower Young's modulus and higher strength than stainless steel [44][45]. However, Chrzanowski et al. [48] demonstrated that some surface treatments cannot result in enhancing bioactivity of NiTi alloy surface when it is immersed in simulated body fluid (SBF), which limits its usage. Although titanium and its alloys are widely used as dental implants, they cannot be used as metal wires for fixing bones due to their low torsional strength (torque). Due to its low fluidity, high reactivity to molds and high melting point, Ti was initially a difficult material to be used in dentistry [49].

2.2.2 Titanium oxides

The formation of TiO_2 oxide layer is related to the biocompatibility of the implant surface, where the interface between implant surface and cells is shown in Figure 2-4 [50]. Usually, Ti spontaneously forms a 6-10 nm thick layer of titanium oxide within microseconds when exposed to ambient environment [51]. Moreover, if the oxide layer is disrupted mechanically, the underlying metal reacts with the atmospheric oxygen to reform the oxide layer. The formation of the oxide layer can be varied due to different manufacturing methods. A comparison between machined cp Ti and cast Ti implants showed that both formed similar

oxide layers, yet the surface integrity varied. Due to this variation, the interaction between bone and the implant surface will vary as well to some extent [52].

In addition, understanding the composition of the oxide layer can help explain the interaction between the implant surface and the biological environment. As previously mentioned, the oxide layer generally consists of the more thermodynamically stable titanium oxide, TiO_2. However, titanium may have multiple valence states in its oxides and other oxides with different Ti and O ratios may exist, such as Ti_2O_3, TiO, Ti_3O, Ti_3O_2, Ti_3O_5 and Ti_2O_2 [36]. The transition of Ti valence may affect the surface wettability and interaction between oxide layer and human cells.

Another important point is the change in oxide layer when Ti implants interact with biological environments after implantation. Using Auger Electron Spectroscopy (AES), McQueen et al. [53] studied the change in composition of Ti implant surfaces during implantation, and observed that the oxide layer formed on the implant surface grows and takes up minerals during implantation. Liedberg et al. [54] showed that phosphate ions were absorbed on implant surfaces after protein absorption by Fourier Transform Infrared Reflection Absorption Spectroscopy (FTIRRAS). Hanawa et al. [49] demonstrated that the oxides on titanium and Ti6Al4V alloys are transformed into complex phosphates of titanium and calcium containing hydroxyl groups using XPS.

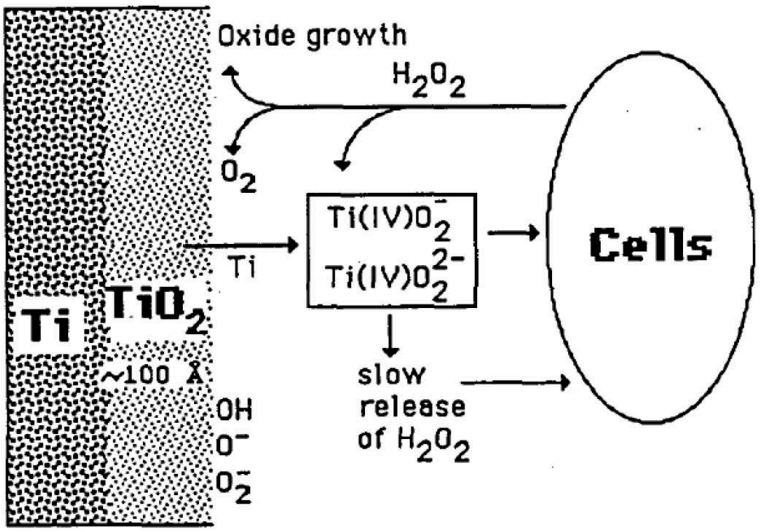

Figure 2-4 Interface between Ti implant surface and human cells [50].

2.2.3 Titanium toxicity

Although titanium and its alloys are considered to be the most biocompatible implant materials due to their excellent biochemical properties, wear and corrosion can still occur, especially in extreme environments such as the oral cavity. The released particles can come from the titanium coating or the titanium implant itself. It is well known that titanium dioxide forms and covers the surface of the implant, which makes it highly resistant to corrosion. However, in recent studies, implant particles were found in the tissue surrounding the implant, which may strongly indicate that corrosion has occurred on the titanium implant. The influence of different environmental factors on dental implants was also studied. It has been reported that corrosion is obvious under the conditions of low pH or high fluoride concentration [55]–[57]. In an in vitro study, Strietzel et al. [55], detected the influence of the presence of fluorine on the corrosion of titanium. Corrosion is further enhanced at lower pH values and is less affected by organic acids and their pH values. Schiff et al. [57] tested the effects of fluorine and pH on titanium and titanium alloys, and found that fluorine ions can destroy and corrode the passivation layer of titanium and titanium alloys.

2.3 Surface modification for titanium implants

It is widely accepted that the surface of materials is of vital significance in the cell response to artificial medical devices. Various surface parameters, such as roughness, thickness of oxide layers, chemical composition, wettability and electrical charge influence the responses of host tissue [58]. For most titanium implants, general manufacturing processes often lead to oxidized and contaminated surfaces, and such surfaces are not appropriate to medical applications and some surface modification methods need to be considered. The goal of this research field is to improve the quality and quantity of osseointegration by promoting bone healing and increasing bone anchoring to implant surfaces.

Two different approaches are usually employed on titanium surfaces, physical and/or biochemical surface treatments. In the first approach, bone nodule anchoring and bone-implant contact will be improved by rough surfaces rather than smooth surfaces. Bone cell migration, adhesion proliferation and differentiation will be facilitated by increasing the

surface area and surface energy. Biochemical surface modification is mainly about coating the surface with bone-like compounds, such as calcium phosphate. By using this approach, protein and other organic molecules on the surfaces will lead to decent cell and tissue responses. Various surface modification methods will be discussed in the following sections.

2.3.1 Pioneering methods for topography modification

Methods that are commercially applied by implant manufacturers, are described in this section; they are grit blasting, acid-etching, plasma spraying and anodization. They are used for promoting interlocking between tissue and implant surface by changing the surface topography and roughness.

2.3.1.1 Grit blasting

This technique is about blasting implant surfaces with hard ceramic particles, such as alumina (Al_2O_3), titania (TiO_2) and hydroxyapatite (HA), at high velocities using compressed air [27]. The surface roughness (Ra) is different according to the particle sizes. Several studies revealed that the bone-to-implant contact (BIC) value is remarkably enhanced by grit blasting with TiO_2 particles. Besides, implant surfaces blasted by calcium phosphate particles present higher BIC value than machined surfaces, as shown in Figure 2-5 [59].

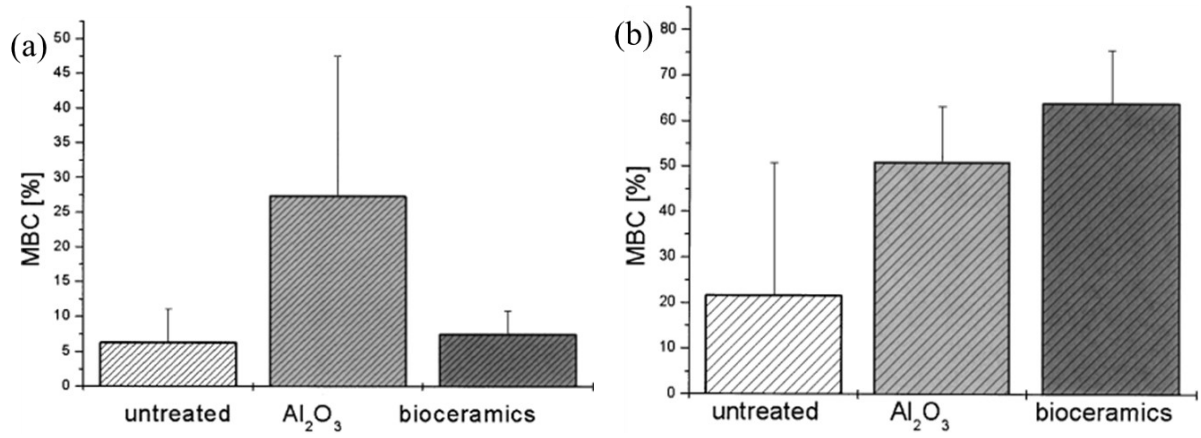

Figure 2-5 Metal–bone contact after (a) 28 days and (b) 84 days as a function of the surface modification between Al2O3-treated and bioceramic-treated as well as untreated specimens. [59].

2.3.1.2 Acid-etching

This method consists in immersing Ti samples in strong acids, such as H_2SO_4, HCl, HNO_3, HF, after which the surface is eroded and the oxide layers and some underlying materials are

removed to produce homogeneous microporous rough surfaces with pits ranging from 0.5 μm to 2 μm in diameter [60]. The success of this method is controlled by acid concentration, temperature and immersion time. An example of surface morphology by acid etching is shown in Figure 2-6 [61]. Compared with sandblasting, this chemical treatment produces a surface without contaminations. Acid etching always follows sandblasting to help remove the blasting particles. In addition, the mixture of several acids is capable of producing micro rough surfaces which promote cell adhesion and thereby bone formation. However, this may reduce mechanical properties. For example, some micro cracks are generated which reduces the fatigue resistance of implants. Acid-etched surfaces are easily damaged by stress generated by bone-implant during surgical implant placement [61].

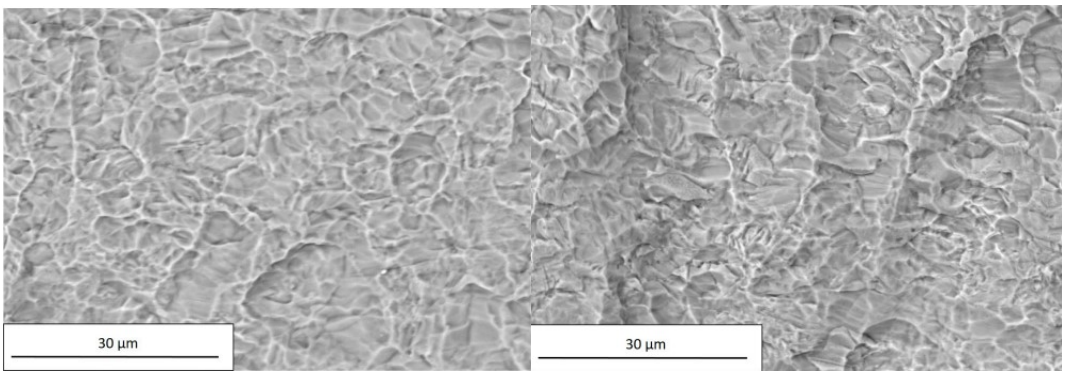

Figure 2-6 SEM observation of acid etched pure Ti surfaces of dental implant made by Biotech Dental. (a) 3.6 mm in diameter; (b) 4.2 mm in diameter [61].

2.3.1.3 Plasma spraying

Another technique applied in surface modification is plasma spraying in which a plasma, such as titanium powder and calcium phosphate powder, is used to melt and spray the sample surface at high temperature in vacuum or ambient environment or inert gas [27]. The thickness of the coatings ranges from 30 μm to 50 μm. The density, temperature of plasma beam and velocity are critical to the formation of the coating. The advantage of this technique lies in the high surface quality obtained, but the coatings tend to present low cell adhesion and are vulnerable to delamination or resorption.

Some studies on the fabrication of coatings on implant materials reveal that proper coating materials are beneficial to improve surface wettability and biocompatibility for dental and orthopaedic implants. Wang et al. deposited tantalum (Ta) on the surface of TiO_2 nanotubes by

plasma spraying to enhance cytocompatibility (Figure 2-7) [62]. Beneficial roughness and hydrophilic characteristics were obtained. MC3T3-E1 cell cultures on Ta/TiO_2 nanotube composite coatings showed improved cell behavior in terms of adhesion, proliferation, differentiation, mineralization, and bone regeneration [62].

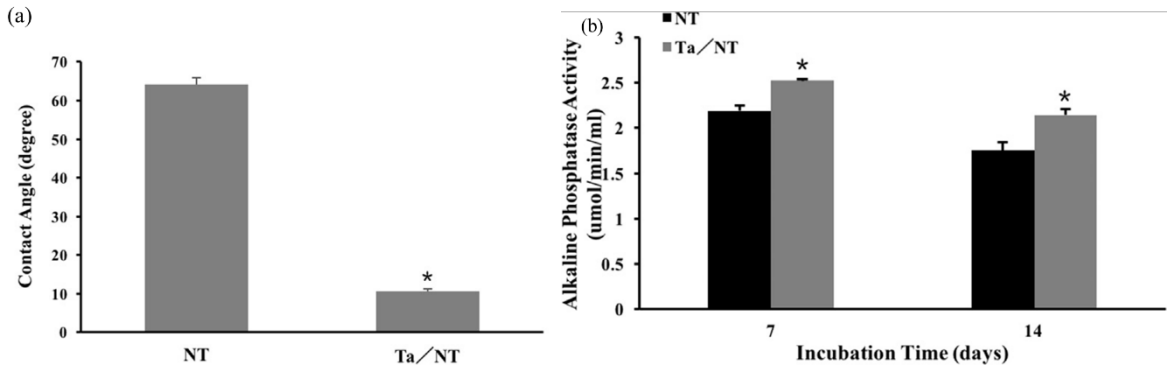

Figure 2-7 (a) Contact angles of the NT and Ta/NT groups and (b) ALP activity of MC3T3-E1 cells on NT and Ta/NT substrates after 7 and 14 days of culture [62].

2.3.1.4 Anodization

In this technique, the implant serves as the anode in an electrochemical cell, and a strong acid serves as the electrolyte. After some time at high current density or potential, an oxide layer over 1μm thick is deposited on the sample surface in the form of microscale or nanoscale TiO_2 nanotubes. Some important anodization parameters include current density, acid type and concentration, electrolyte temperature, oxidation duration. Anodized surfaces show improvement in cell attachment and proliferation. Compared with machined surfaces, anodized surfaces can enhance bone healing and osseointegration in the environment around the implant [63]. The bone-like structure is shown in Figure 2-8, where TiO_2 nanotubes are synthetized and calcium (Ca) and phosphorous (P) are doped on the surface by anodization [28]. The bone-like TiO_2/Ca and TiO_2/P structure presented high corrosion resistance, improved MG63 cell adhesion and proliferation compared to smooth surfaces.

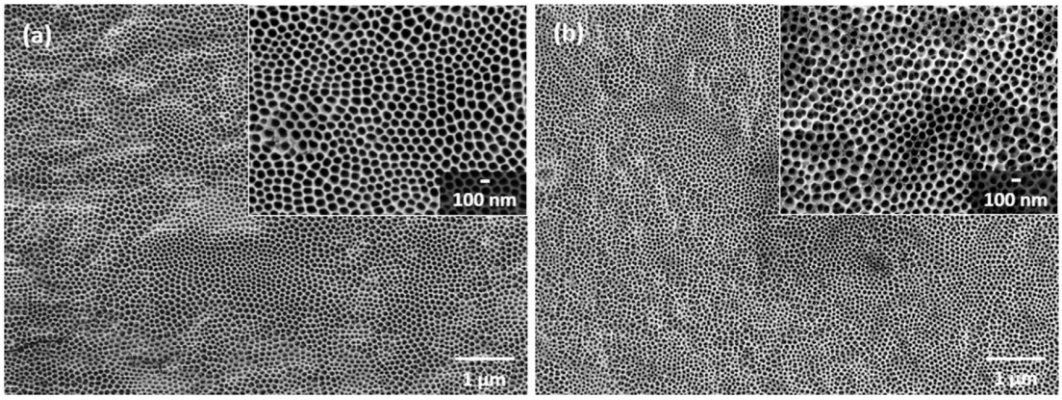

Figure 2-8 SEM micrographs of TiO_2 nanotubes doped with Ca and P [28].

2.3.2 Advanced methods for topography modification

In order to improve the drawbacks inherent to the surface modification methods presented in the previous sections, advanced methods are described in this section, namely photolithography, and e-beam lithography. These techniques are not employed by industries yet. However, they can produce well-defined surfaces, precisely controlled surface chemistries and are highly reproducible. The methods introduced in this section are analogous to "surface patterning" and have been mostly applied for semiconductors and polymers. The application of these advanced methods is still limited, especially the application in improving the osseointegration, which is used most in the lab or for precise devices and needs further deeper exploration.

2.3.2.1 Photolithography

This is generally used for semiconductors as a surface patterning technique. It utilizes an exposure of light-sensitive polymer (photo-resist) to UV light to define a desired pattern [64]. In the exposed areas, the polymer chains of the photoresist are broken, making it more soluble in a chemical solution called a developer. Subsequently, the exposed photoresist is removed by the developer to form a desired photoresist pattern. Figure 2-9 depicts a schematic illustration of the main steps in lithography [65]. The patterned photoresist can be used as a protective layer in a subsequent etching or deposition process to establish a topography on the substrate. However, this technique is not suitable for non-polar patterns, and is limited to nanopatterns due to the resolution limit.

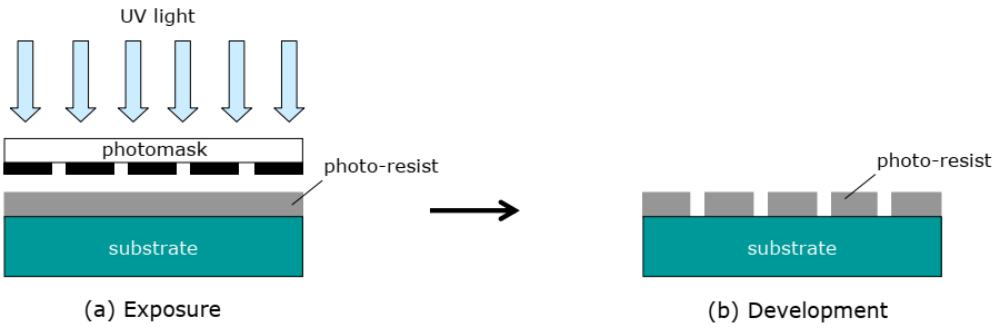

Figure 2-9 Schematic illustration of main steps in photolithography [65].

2.3.2.2 E-beam lithography

E-beam lithography [66] uses accelerated electron beams focused on electron-sensitive resist [52][53] for exposure. Subsequently, electron beam spots as small as a few nanometers in diameter are scanned on the resist surface in a point-to-point manner to sequentially generate patterns as shown in Figure 2-10 [65]. The advantage of using an electron beam, not light, is that it is maskless which allows for direct writing on surfaces. However, lack of production capacity limits its application in research and manufacturing. Therefore, this technology is often used to make prototypes of nanoscale structures and devices. So far, due to the difficulty in developing a practical electron beam source, application toward creating large scale and complex dimensional structures is limited as well [69].

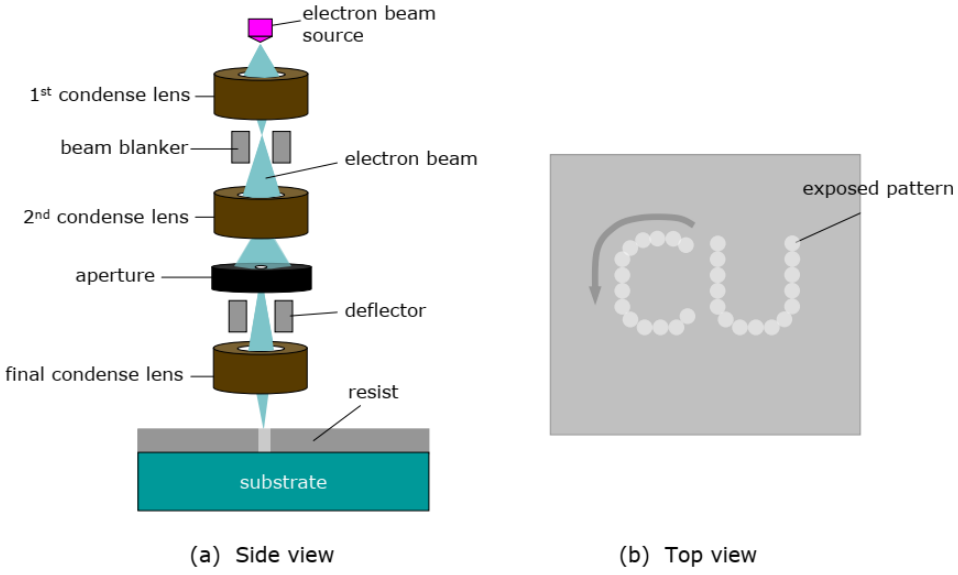

Figure 2-10 Schematic illustration of e-beam lithography [65].

2.4 Laser surface texturing of Ti surfaces

Laser technique has been used in various fields for decades to cut or texture surfaces. Recently, ultrafast laser surface texturing (picosecond and femtosecond) has become a simple, high-resolution, fast, controllable, reproducible, non-contact processing technology, suitable for metals, polymers, and semiconductors. It is possible to fabricate various microscale and nanoscale features over a large area, which makes it a very promising surface modification technology, which can be scaled to industrial production. By changing laser process parameters, such as energy density, wavelength, pulse number, scanning speed, laser polarization, incident angle and environment, different patterns can be generated on the surface of the material [70]. Through ultrafast laser structuring, the optical, mechanical, wetting, chemical and biological properties of the solid surface can be controlled, and novel materials can be manufactured, which can be widely used in photonics, plasma, micro/nano fluids, wetting and biomedical applications [60].

2.4.1 Femtosecond laser surface direct writing technique

The interaction between laser and substrate leads to laser ablation, which is defined as the removal of materials from the surface under irradiation above the ablation threshold, ultimately leading to the formation of microstructure and nanostructure. The ablation threshold is the minimum energy required to initiate the materials' removal process. The mechanism of laser-material interaction and ablation depends on the nature of the materials and laser parameters, such as the energy density, wavelength and pulse duration [71].

In recent years, by using femtosecond (1 fs = 10^{-15} s) laser direct writing technology, various micro- and nano-scale features have been demonstrated on a variety of materials. It is a maskless single-step process, which can texture materials in an ambient environment without the requirement for a vacuum or controlled atmosphere [72]. Compared with other longer pulsed laser (e.g. nano- or picosecond lasers), the main advantage is its high peak intensity pulse within a short time frame, which enables a precise surface texturing and a small heat affected zone (HAZ). A 1.5 μm wide HAZ was measured on Al after laser ablation with duration of 200 fs, compared with a 20 μm wide HAZ measured after 8 ns laser ablation.

As the pulse is Gaussian-shaped, the intensity changes over the length of pulse where it is at the highest in the center of pulse [73]. The laser ablation threshold is expressed by the term of peak fluence, which can be defined as [74]:

$$F = \frac{2E}{\pi {r_0}^2} = \frac{8E}{\pi {\omega_0}^2}$$

where E is single pulse energy, and r_0 and ω_0 are beam radius and diameter, respectively. For a Gaussian laser beam, the beam radius is typically defined by $1/e^2$ (13.5%), and the single pulse energy can be calculated as:

$$E = \frac{P}{f}$$

where P is the average power of the laser beam and f is the repetition rate (frequency) of the laser.

The parameters of laser processing can be classified in four categories: (1) laser beam parameters, (2) sample parameters, (3) scanning parameters and (4) processing parameters [74]. By varying laser beam parameters such as pulse energy, beam polarization, laser beam power and the number of pulses, as well as scanning parameters (e.g. scan speed) and processing parameters (e.g. processing environments), a variety of surface structures can be reproducibly produced [71]. Micron and nano-scale surface structures can be generated by this direct writing method, such as laser induced periodic structures (LIPSS), grooves, nanoholes, circles and various irregular structures [75].

2.4.2 Laser induced surface structure

Laser induced surface structures can be classified into two types: nanostructures (e.g. random and periodic structures) and microstructures (e.g. groove, hole and columnar structures).

2.4.2.1 Periodic nanostructures

Laser induced periodic surface structures (LIPSS) are periodic parallel ripples or waves features that cover the surface. These ripples can be generated by continuous wave (CW) or pulsed laser irradiation on various types of materials (such as metals, ceramics, polymers, and semiconductors) under specific laser processing conditions [25][32]. LIPSS are similar to the common periodic patterns in nature, such as sand dunes and the bottom of oceans, lakes and

rivers [12], as shown in Figure 2-11. However, although ripples formed in nature are large-scale features, LIPSS is a micron or nanoscale structure with periodicity and height in the micron or sub-micron range.

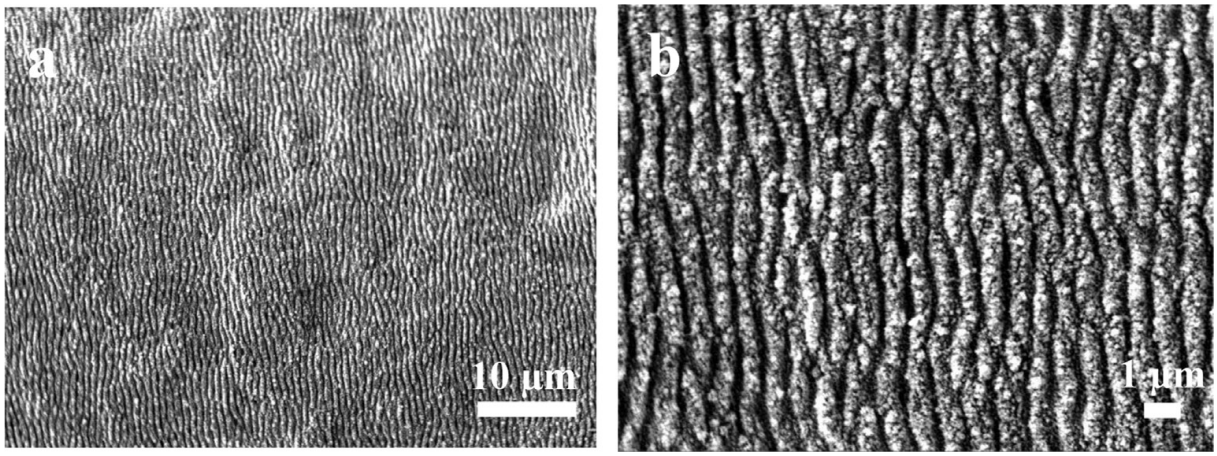

Figure 2-11 SEM images of microstructure of LIPSS [75].

2.4.2.2 Groove structures

Periodic microgrooves are also observed on various metals. These grooves can become wider and deeper with an increase in fluence or an increase in number of pulses, which can be achieved by decreasing the scanning speed or increasing the overlap in a path [74]. LIPSS may be superimposed on these groove structures. Figure 2-12 shows the parallel microgrooves on glass surfaces [13] and crossed grooves on Ti alloy [76]. The formation mechanism of periodic groove structures can be described as the spatial energy distribution generated by the interaction between the laser beam and surface wave that may be caused by LIPSS [77]. Bizi-Bandoki et al. [78] observed that the periodicity of grooves increased with an increased in the number of pulses on TA6V and SS316 surfaces. Groenendijk et al. [79] reported that the groove increased in size by decreasing the scanning speed at constant fluence, and eventually disappeared with the forming of trench and columnar structures at lower scanning speed.

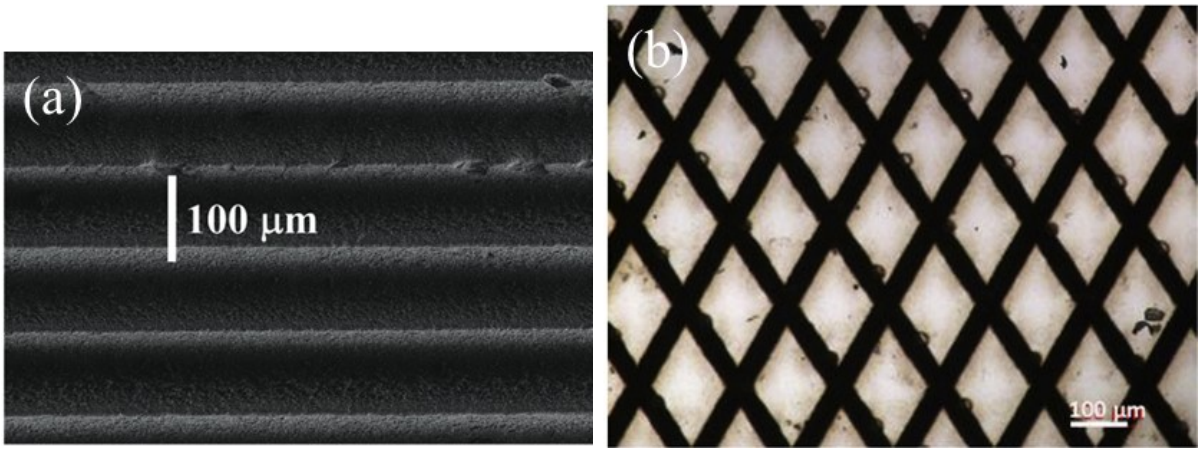

Figure 2-12 Surface structure of (a) parallel microgrooves on glass [13], (b) crossed grooves on Ti alloy [76].

2.4.2.3 Other structures

Other novel and complicated surface structures, such as holes, dimples (Figure 2-13 (a)) and concentric circles (Figure 2-13 (b)), can be observed on various metals now by controlling the laser beam parameters and scanning parameters, which expands the application of this technique in various fields.

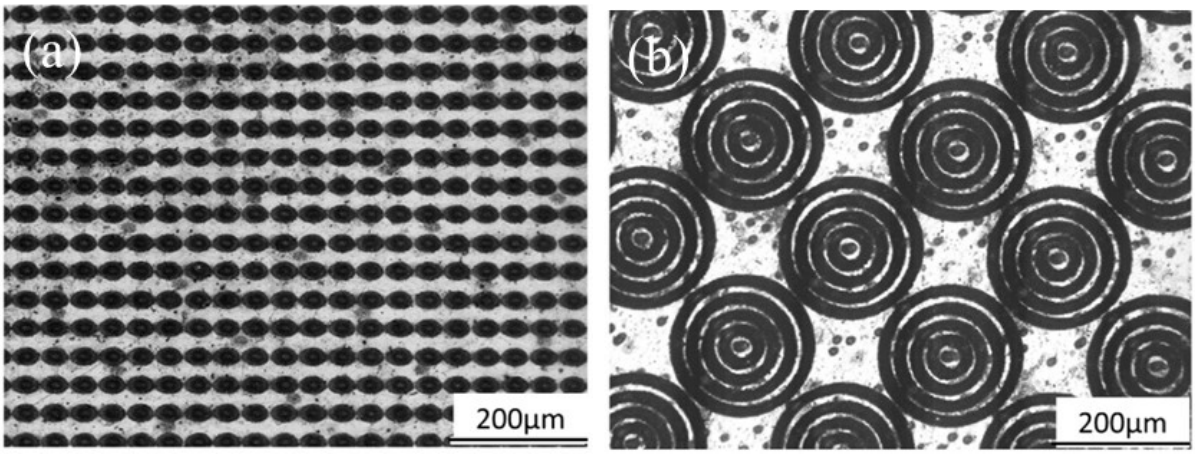

Figure 2-13 Surface structure of (a) an array of dimples, (b) concentric circles on Al alloy [80].

2.5 Surface wettability

The surface wettability is the degree of liquid spreading on the surface of a solid, which is an important property for describing solid surfaces [81]. Controlling surface wettability is an important issue for implant materials since it can affect the absorption of protein and cells, and has been a focus of research in the last decade. The wettability of a solid surface depends on the surface topography and chemistry [82].

2.5.1 Young's model

The wetting behavior of solid surfaces can be devided into six categories, superwetting/superwicking ($\theta_W \approx 0°$), superhydrophilic ($\theta_W < 10°$), hydrophilic ($10° < \theta_W < 90°$), hydrophobic ($90° < \theta_W < 150°$), superhydrophobic lotus leaf effect ($\theta_W > 150°$), and superhydrophobic rose petal effect ($\theta_W > 150°$) [81].

Young's equation is a simple analytical model to describe the equilibrium condition of a droplet staying on an ideal flat surface:

$$\cos(\theta_W) = \frac{\gamma_{SA} - \gamma_{SL}}{\gamma_{LA}}$$

where θ_W is the static contact angle in equilibrium, γ_{SA} is the interfacial tension between solid and air that indicates the energy of unit surface area of interface, γ_{SL} is the interfacial tension between solid and liquid, and γ_{LA} is the interfacial tension between liquid and air.

The use of this equation is very limited, since it requires ideal flat surfaces that are smooth, chemically uniform, rigid, and non-reactive, as shown in Figure 2-14(a). Since all real surfaces are not ideally flat, Young's equation can only provide a basic knowledge of the static contact angle and interfacial tensions.

2.5.2 Wetting theories of rough surfaces

Because surfaces are not flat, two models, one by Wenzel and the other by Cassie-Baxter (CB) equations, describe the effect of roughness on the surface wetting behavior.

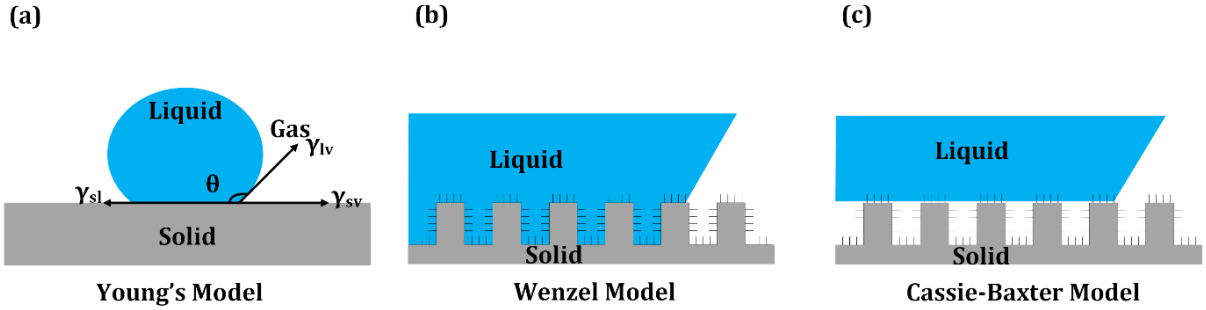

Figure 2-14 Wetting models, (a) Young's model; (b) Wenzel model; (c) Cassie-Baxter model [81].

2.5.2.1 Wenzel theory

In the Wenzel model, the actual interfacial surface area between liquid and solid is increased due to the roughness, and the liquid completely wets the structure, as shown in

Figure 2-14(b). Therefore, the hydrophobicity level and hydrophilicity level are increased compared with smooth surfaces, which means that the hydrophilic surfaces become more hydrophilic and hydrophobic surfaces become more hydrophobic. The apparent contact angle (θ^*) is proposed as:

$$\cos(\theta^*) = r_f \frac{\gamma_{SA} - \gamma_{SL}}{\gamma_{LA}} = r_f \cos(\theta_Y)$$

where, r_f (r_f>1) is the roughness factor defined as the ratio of the actual surface area to the smooth surface area, θ_Y is the static contact angle from Young's equation, γ_{SA}, γ_{SL}, and γ_{LA} represents the interfacial tension between solid and air, solid and liquid and liquid and air, respectively.

2.5.2.2 Cassie-Baxter theory

In the Cassie-Baxter model, some air is trapped by the surface roughness so that the liquid cannot penetrate that roughness, as shown in Figure 2-14(c). Therefore, the liquid-solid interface is the combination of liquid-solid interface and air-solid interface. The apparent contact angle (θ^{**}) is proposed as:

$$\cos(\theta^{**}) = r_f f \cos(\theta_Y) + f - 1$$

where θ_Y is the static contact angle on smooth surfaces, r_f is the roughness factor, and f is the fraction ($0 < f < 1$) of the wet solid part under the droplet.

2.5.3 Wettability controlled by ultrafast laser

Many engineering methods that focus on improving surface wettability try to control surface chemistry and surface micro-/nanostructure.

In the past decades, laser-based surface treatment methods have become one of the broad research areas of top-down methods to create micro-/nanostructures on material surfaces. Remarkable progress has been made in recent years to explore the fundamental knowledge of laser processes and advanced surface modification methods.

Laser induced periodic surface structure, also known as LIPSS, are commonly fabricated on the material surface. It was shown by Hourieh, et al. [75] that a titanium surface covered by LIPSS is superhydrophilic right after laser machining, and the long-time exposure to air has an extreme influence on the surface wettability. After 1-year exposure to air, the contact

angle of a textured titanium surface is about 153°, while it was about 0° right after laser machining and increased up to 136° after 45-day exposure in air. Wu et al. [83] found that microscale cone-shape spikes covered with LIPSS on stainless steel surfaces improved the wetting behavior compared with the only the LIPSS nanostructure.

Raimbault et al. [84] and Yu et al. [85] observed anisotropic wetting behavior on a laser grooved Ti6Al4V alloy surface. They showed that the groove array created by laser increased the hydrophobicity of textured surfaces, and the droplets mainly spread along the groove orientation. The contact angle measured parallel to the groove orientation is generally larger than that perpendicular to the groove direction. Besides, the ratio of line spacing and line depth also affect the wetting behavior of material surfaces textured using laser machining.

2.6 Dynamics of interaction between cells and biomaterials

2.6.1 Osteoblast cells

Osteoblasts are the main functional cells of bone formation, responsible for the synthesis, secretion and mineralization of bone matrix.

Bone is constantly undergoing reconstruction. The process of bone reconstruction includes osteoclasts attaching to the old bone area, secreting acidic substances to dissolve minerals, secreting proteases to digest bone matrix, and forming bone resorption lacuna; then, osteoblasts migrate to be absorbed at the site, the bone matrix is secreted, and the bone matrix is mineralized to form new bone [64][65]. The balance between the acting of osteoclasts and osteogenesis is the key to maintaining normal bone mass.

2.6.1.1 Origin of osteoblasts

Osteoblasts originate from the interstitial cells of the pluripotent bone marrow stromal cells. In addition to osteoblasts, stromal cells can also differentiate into chondrocytes, fibroblasts, adipocytes or muscle cells, where the differentiation of osteoblast cells lineage is shown in Figure 2-15. The source lineages of osteoblasts are as follows [88]:

(1) Bone marrow colony forming unit,

(2) Osteogenic progenitor cells, which can differentiate into pre-osteoblasts and

pre-chondrocyte lineages, are often located in the bone marrow cavity and have strong self-proliferation abilities,

(3) Pre-osteoblasts, the nearest osteogenic precursors, can differentiate into osteoblasts and have the ability to synthesize and proliferate.

Osteoblasts develop from pluripotent mesenchymal stem cells under the regulation of various regulatory factors in the body. The main regulatory factors are BMP-2, which can induce the differentiation of stromal cells into osteoblasts, specifically inducing the differentiation of mesenchymal stem cells to form osteoprogenitor cells and then form pre-osteoblasts.

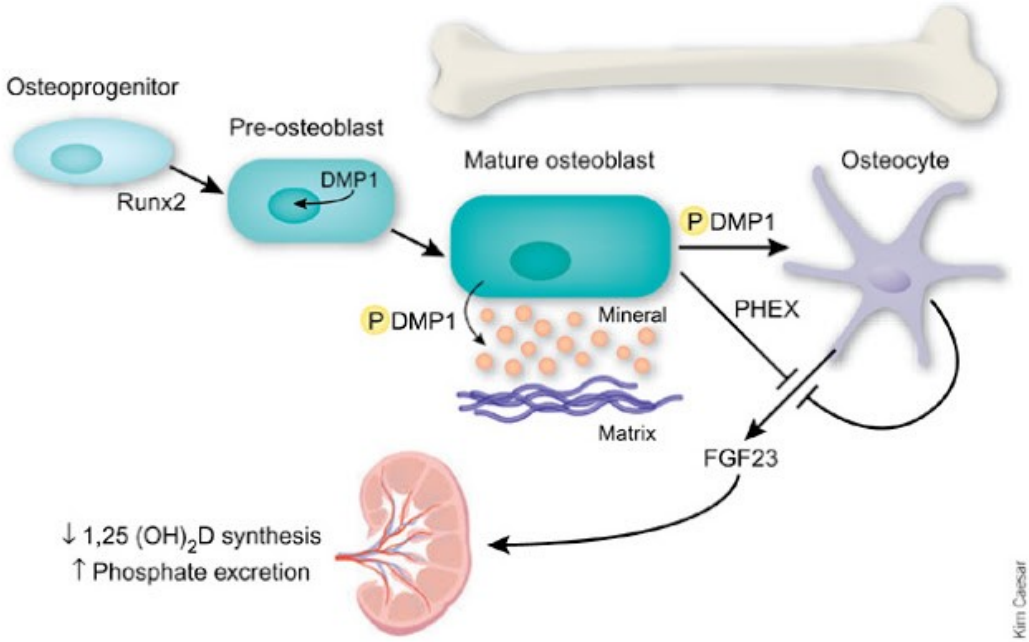

Figure 2-15 Scheme of differentiation of osteoblast cells lineage [89].

2.6.1.2 Osteoblast development stage and bone formation mechanism

Osteoblasts undergo four stages in the process of bone formation: osteoblast proliferation, extracellular matrix maturation, extracellular matrix mineralization, and osteoblast apoptosis [90]. Many factors can adjust these stages and ultimately regulate bone formation.

During the proliferation of osteoblasts, the number of osteoblasts increases to form multi-layered cells, and synthesize and secrete type I collagen so that they can eventually be mineralized to form bone nodules. The regulation of osteoblast proliferation is specifically the regulation of the cell cycle. The latter includes the regulation mechanism of cell replication

and cell division under the action of mitogens. The schema of basic explant culture is shown in Figure 2-16 [91].

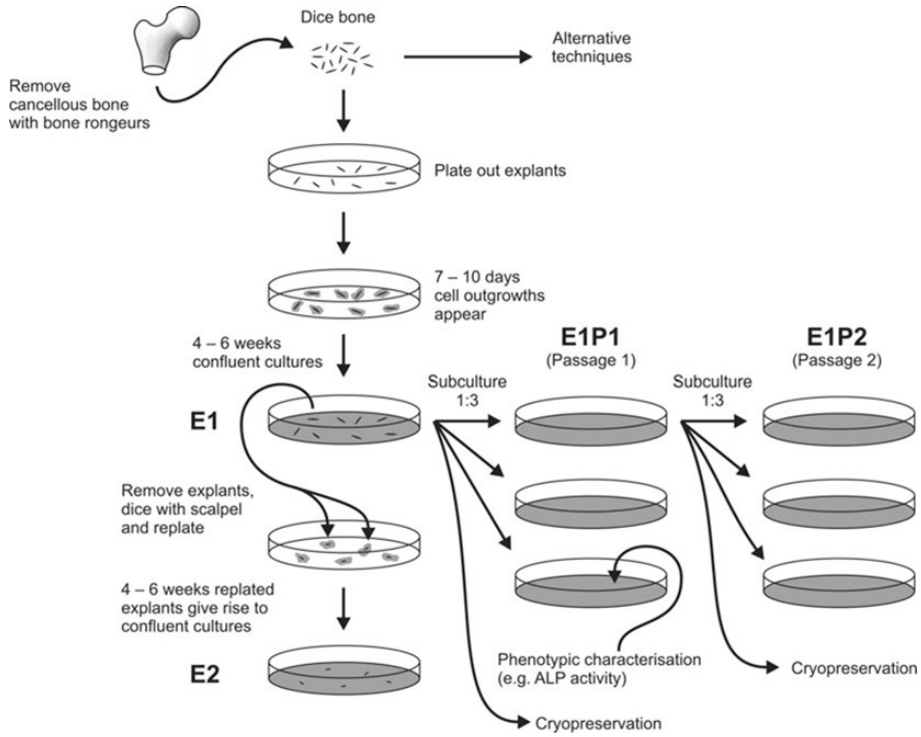

Figure 2-16 Schematic representation of the technique used to isolate human bone-derived cell (HBDCs) from explanted cancellous bone [91].

2.6.2 Effect of surface roughness on cell fate

The macroscopic behavior of the material is significantly affected by the morphology of the surface [53]. The influence of surface morphology on biological reactions remains to be understood. At the cellular level, biological reactions, such as the direction and migration of cells and the production of cells in the cytoskeleton arrangement of tissues, are directly affected by surface topography [92]. There is evidence that suitable surface roughness on nano and micro scales can successfully achieve osseointegration of titanium implants. The differentiation, proliferation and matrix production of osteoblasts and the production of local growth factors and cytokines are affected by surface roughness.

Particularly, there are several surface treatments that have been performed to optimize the surface topography of titanium implants in bone-contact applications. Most extended treatments are sandblasting and acid etching [93]. The main purpose of these tissue treatments is to achieve greater contact between the bone and the implant to reduce healing time and

accelerate integration into the host tissue [94]. The texturing of dental implants can improve the mechanical adhesion to bone, but at the same time, roughness and grooves may be the preferred locations for protein adsorption [95].

2.6.3 Effect of wettability on cell fate

The adsorption of biomolecules on the implant surface "in vivo" is indeed a dynamic process, driven by the physical and chemical interaction between the adsorbent surface and the macromolecules[96]. This precursor process creates a "regulatory membrane" that will regulate the cellular host response. Free surface energy is a factor that can explain the wetting behavior of surfaces, which is further related to the interactions between cells and biomaterial surfaces. Therefore, the wettability of the implant can determine the adsorption of proteins, which in turn determines the adhesion of cells [65][73][75]. For example, hydrophobic surfaces may reduce major interactions with aqueous biological systems. Therefore, it is usually reported that the surface of biomaterials that has moderate hydrophilicity leads to improved cell growth and higher biocompatibility [98]. However, as the wettability of the implant becomes more hydrophobic, cell adhesion will decrease. This indicates that there is a series of optimal surface energies [99]. Also, the "in vivo" interface reaction will change the relevant physical and chemical surface parameters, such as surface energy, thereby affecting the long-term stability of the implant [100].

Numerous studies have demonstrated that the surface wettability of biomaterials plays a vital role in regulating important physiological processes, such as protein adsorption, cell attachment and adhesion and cell proliferation [75][84]. The wettability of implants will affect the spreading of biological fluids on the surface of implants and the attachment of some important molecules in the early stages of bone formation [87]. Since the cells do not directly interact with the surfaces of implants, but with the protein layer that is previously adsorbed on it, the adsorption of extracellular matrix proteins, such as fibronectin and vitronectin, on the surface of implants will affect cell adhesion and further cell fate, Figure 2-17 [26].

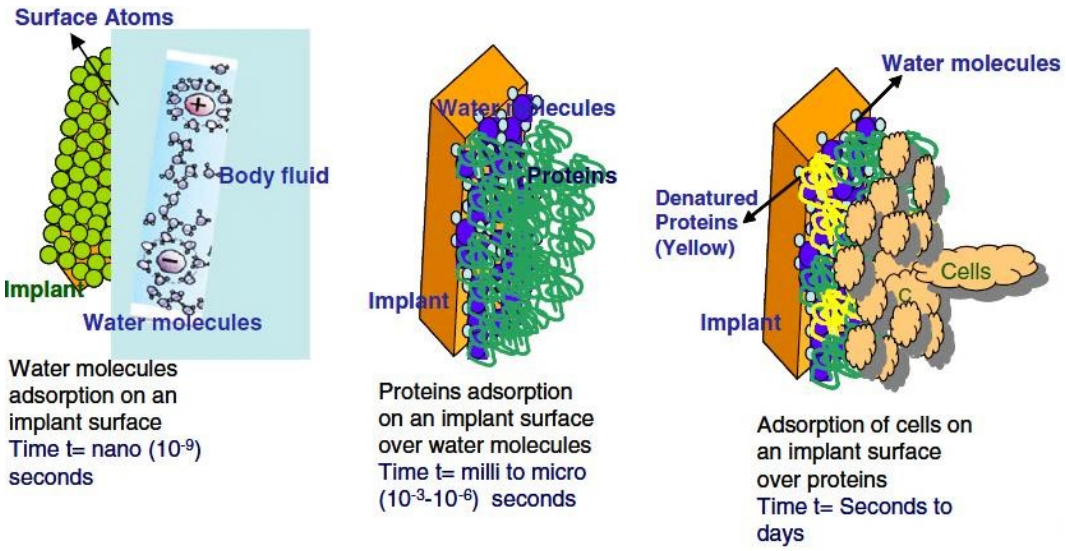

Figure 2-17 Cell adhesion on implant surface at early stages, where wettability plays a crucial role [26].

2.6.4 Effect of surface chemistry on cell fate

Changes in the physical and chemical surface properties of biological materials can improve the interaction with cells. All studies have demonstrated that changes in surface chemistry have a major impact on cell function. Zreiqat et al. recently studied this on a molecular scale [101]. They used Western Blot Analysis to prove that the intracellular signal conduction is different in human primary bone cells cultured on titanium alloy modified by ion beam implantation of Mg or Zn ions.

Due to the development of new technologies, it is now possible to customize surface chemistry through synthetic tools and nanofabrication techniques [80][81]. In particular, self-assembled monolayers (SAMs) have recently emerged as one promising tool to create surfaces with better biocompatibility and less interference from substrate. In recent years, SAMs have been widely used to clarify the effects of surface chemistry on cell adhesion, mainly because of their ease of processing [103]. Keselowsky et al. [104] proved that due to SAMs, the surface with -OH and NH_2 groups (hydrophilic surfaces) increased osteoblast-specific gene expression compared to surfaces with CH_3 groups (hydrophobic surfaces), and alkaline phosphatase enzyme activity and matrix mineralization (all signs of osteoblast differentiation). Barbosa et al. [105] demonstrated that the thickness of the fibrous capsule around the implant covered by the CH_3-terminated SAMs was significantly increased

compared with the COOH and OH-terminated SAMs.

2.7 Summary of literature review

In summary, there are three main factors that can affect the biocompatibility of implant materials, which are surface roughness, surface energy and surface chemistry. By controlling the surface roughness, the surface energy can be changed. And various environments during processing and storage can lead to different chemical properties of surfaces. The three factors cannot be decoupled, and it is the combination of the three factors that affects the protein adsorption and cell behaviors, as shown in Figure 2-18 [106].

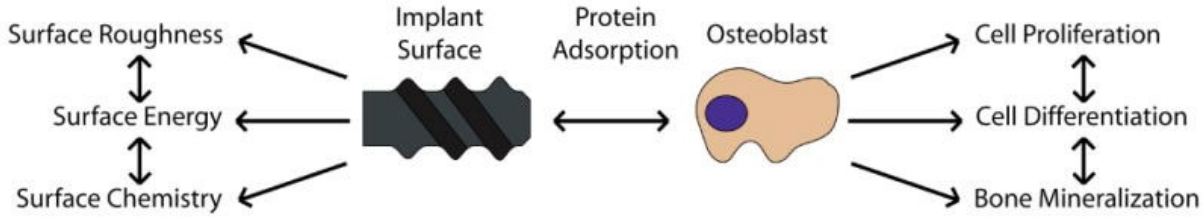

Figure 2-18 Diagram showing the direct and indirect interactions between surface properties (e.g., surface roughness, surface energy, surface chemistry) and biological events, such as protein adsorption and osteoblast response (e.g., proliferation, differentiation, bone mineralization) [106].

3. Methodology

The methodology section of this thesis is divided into three parts.

In part one, the laser surface texturing technique, the supporting techniques during laser processing and the characterization methods of textured surfaces and their chemical composition are described.

In part two, the contact angle measurement procedure and the characterization of surface wetting behavior are presented.

In part three, the biological experiment process for assessing surface biocompatibility and characterizing cell response on laser textured surfaces are presented.

3.1 Laser surface texturing process

3.1.1 Preparation of commercially pure titanium samples

Square samples of commercially pure titanium with dimensions of 10 x 10 mm^2, and thickness of 250 μm and 900 μm respectively, were cut by electrical discharge machining (EDM). The chemical composition and mechanical properties of pure titanium are given in Table 3-1 according to the American Society for Testing and Materials (ASTM) Standards. Samples were prepared before laser texturing as shown in the flowchart Figure 3-1.

Before laser texturing, samples were ultrasonically cleaned in 99% ethanol for 10 minutes to remove oil or dust that may have been present on the sample surfaces. Samples were polished with a colloidal silica suspension (OPS) to smooth the samples and remove the oxide layer resulting from sample preparation (EDM cutting) and long-time exposure to air.

Table 3-1 Chemical compositions and mechanical properties of cp Ti

Chemical Composition (wt%)						Mechanical Properties			
Ti	C	Fe	H	N	O	Elastic modulus (MPa)	Yield strength (MPa)	Tensile strength (MPa)	Elongation (%)
Balance	0.10	0.30	0.015	0.03	0.25	104	483	550	15

Figure 3-1 Flow chart describing procedures of pre-treatment before laser texturing on Ti.

3.1.2 Laser surface texturing process

Surface texturing of titanium samples was carried out using a femtosecond laser direct writing technique. By controlling the laser process parameters and conditions, various surface patterns can be created reproducibly via material ablation. A Yb: KWG laser system with a central wavelength of 1030 nm and a laser pulse duration of 300 femtosecond was used. A green laser with a wavelength of 515 nm was obtained by a nonlinear frequency doubling beta barium borate (BBO) crystal for laser texturing on Ti surfaces. The Ti samples were mounted on a computer-controlled X-Y-Z stage, and the laser texturing processing was monitored by a CCD camera from above the samples.

The femtosecond laser texturing setup is shown in Figure 3-2. The laser process parameters and related conditions are presented in Table 3-2. Since the high magnification lens is very sensitive to changes in surface heights (i.e. it becomes unfocused), a Prima chromatic confocal point sensor is used to ensure the sample surface remains on the laser focal plane. Surface inhomogeneities are transferred into numerical data by the sensor and transferred to

the laser controller before laser machining. A fume extractor was also employed during the laser machining process to remove formed and ejected debris for improving the quality of grooves.

Two surface patterns were designed consisting of uniform grooves and gradients. The line spacings for uniform grooves were chosen to be 10 μm, 4.8 μm, 2.4 μm and 1.2 μm, and the line spacings of gradients varied from 1.2 μm, 2.4 μm, 3.6 μm, 4.8 μm to 6 μm. The rationale selection was based on the size of cells used in biological experiments, which are about 20 μm in diameter. The optimal laser beam power was found to be 2 mW. Other laser process parameters remained unchanged, including repetition rate of 200 kHz, pulse energy of 30 uJ and scanning speed of 20 mm/s. All samples were machined in ambient atmosphere at room temperature. To test the effect of storage environment after laser machining, samples were placed in air, 99% ethanol or in a rough vacuum right after laser machining. The selection of ethanol and vacuum storage environment was to prevent the contamination from air and O_2 and to explore if the wetting behavior of samples does not change for targeted storage environment.

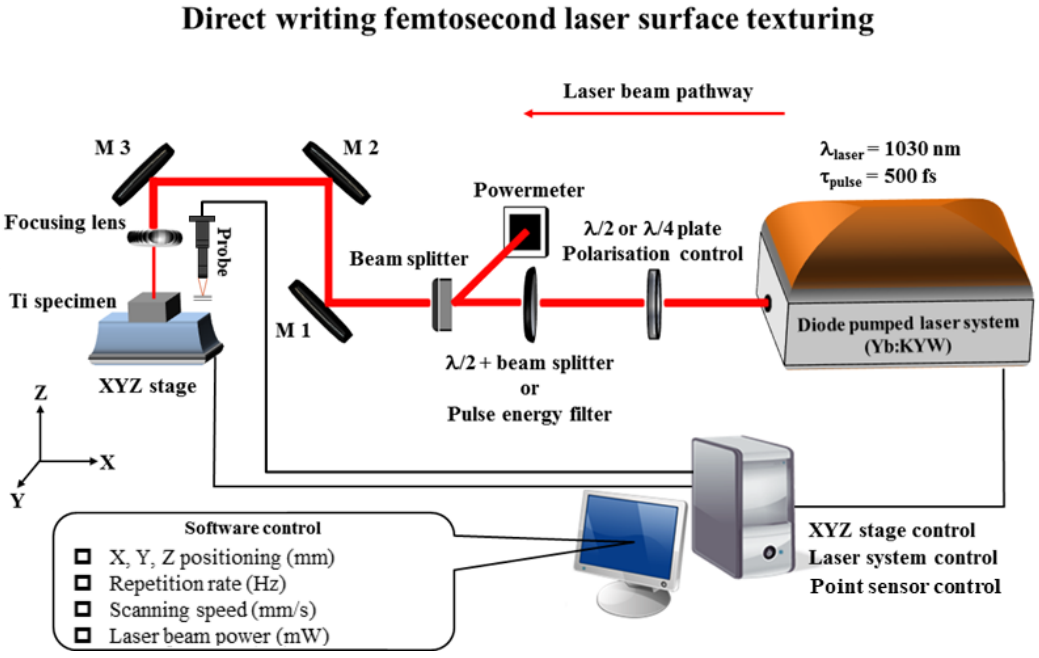

Figure 3-2 Schematic setup of femtosecond laser surface direct writing method with chromatic confocal point sensor (adapted from [1]).

Table 3-2 Main laser process parameters used in laser texturing on cp Ti surfaces

Laser process parameters	
Laser beam power	2 mW
Repetition rate	200 kHz
Pulse energy	30 uJ
Scanning speed	20 mm/s
Working atmosphere	In ambient air at room temperature with fume extractor
Other instruments	Point sensor
Line Spacing	Uniform grooves: 10 μm, 4.8 μm, 2.4 μm, 1.2 μm
	Gradients: 1.2 μm, 2.4 μm, 3.6 μm, 4.8 μm, 6 μm
Storage Environments	Air, Vacuum, Ethanol

3.1.3 Characterization of textured surfaces

The textured surfaces were characterized by Optical Microscopy (OM, Olympus OM), and Scanning Electron Microscopy (SEM, Zeiss Gemini SEM 500) from the lowest magnification of 5kx to the highest of 30kx. Under the highest magnification, the inner microstructure of grooves can be visualized. An Atomic Force Microscopy (AFM, Park NX10) was employed to analyze the surface roughness. The AFM images were processed using XEI software.

Surface chemistry of laser treated cp Ti surfaces was investigated using X-ray Photoelectron Spectroscopy (XPS, Kratos Axis Ultra DLD) using Al K_α radiation at 1486.69 eV (150 W, 10 mA). Adventitious C 1s peak at binding energy of 284.8 eV was used as a reference for all XPS spectra. Survey spectra and high resolution spectra for O 1s, Ti 2p, and C 1s were recorded. Fitting of survey spectra and high resolution spectra was performed using the CasaXPS software. Due to the difficulty of transportation and cost, one sample of each condition was analyzed.

3.2 Surface wettability measurements of textured surfaces

3.2.1 Contact angle measurement

Surface wettability was measured using the sessile drop method, where distilled water was chosen as the testing medium and the testing environment was room temperature. All samples were ultrasonically cleaned in ethanol for 5 minutes to remove debris from the laser machining. Samples were dried with a paper towel (Kimi wipes) and left in air for about 30 s before the measurement. The contact angle of these samples was therefore measured right after laser machining and cleaning which corresponds to a 0-day test in this thesis. After machining, samples were also stored in air, ethanol and rough vacuum, and contact angle measurements were carried out at specific time points, namely 1 day, 3 days, 5 days, 7 days, 2 weeks, 3 weeks, and 4 weeks. The contact angle measurement (CAM) experimental setup is shown in Figure 3-3.

The contact angle measurement was performed by depositing a 1 uL droplet of distilled water with a computer controlled microsyringe on the surface of samples placed on the stage at room temperature. The droplet was approached to the surface by a constant depositing speed until it touched the surfaces. Images of droplets were acquired by a high-magnification camera when the droplet was stable on the surfaces, approximately several seconds after the droplet deposited on the surface, both in the direction of the laser machined grooves and in the direction perpendicular to the grooves. The droplet was deposited in the center area of each sample for better measurement. For each condition, 3 samples were used, and on each sample, there were at least 2 drops deposited one by one. Between every depositing of one drop, the surface was dried by Kimi wipes.

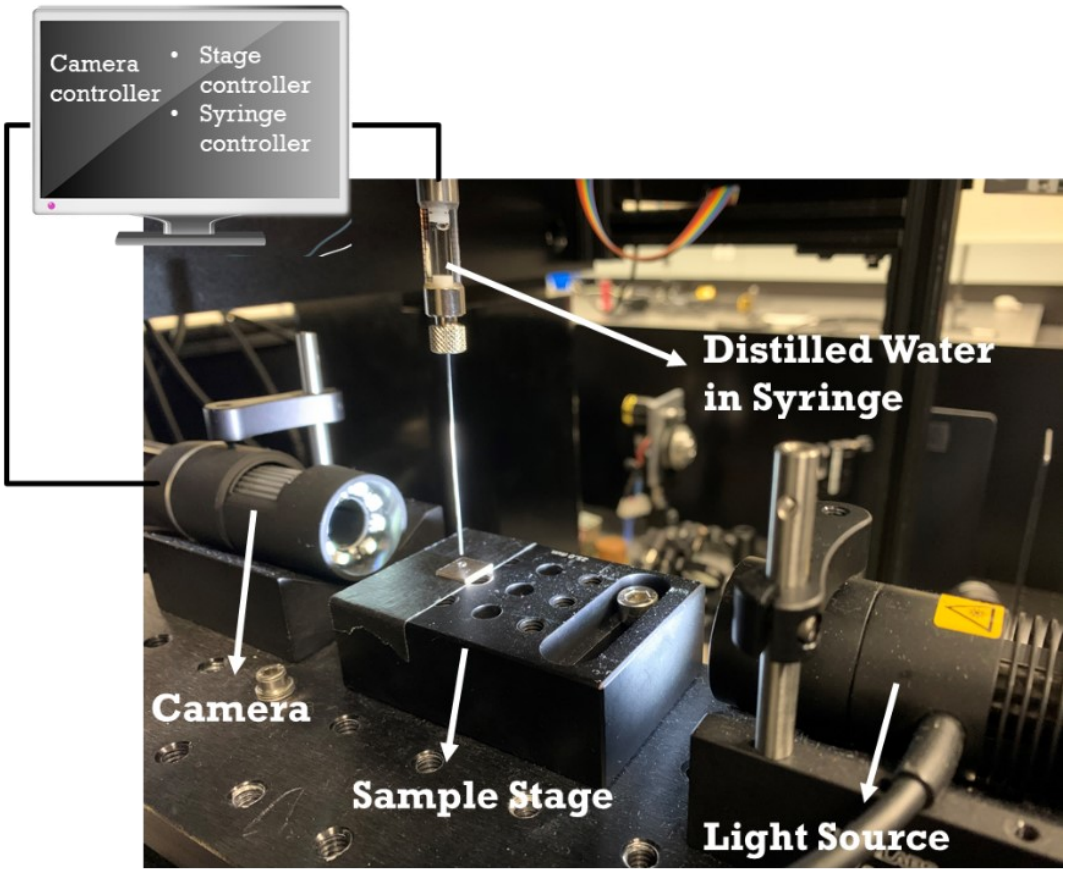

Figure 3-3 Experimental setup of contact angle measurement with light source and computer-controlled video camera and syringe.

3.2.2 Contact angle data analysis methods

All images of contact angle were analyzed using ImageJ software with the contact angle plugin, as shown in Figure 3-4. The white curves are the fitted circle or ellipse based on the size of the droplet. The contact angle on the right and left side of droplets was obtained. In order to verify the reliability of data, the error bars of standard deviation were calculated based on 2 to 3 samples per laser parameter and per storage parameter, and introduced in charts.

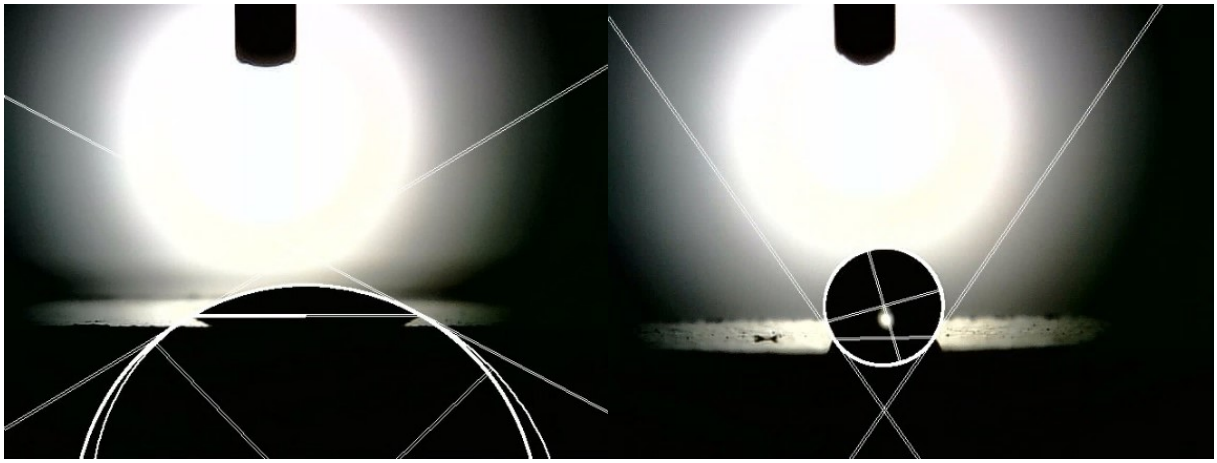

Figure 3-4 Examples of CA images processing by ImageJ.

3.3 Biocompatibility of laser textured surface

The general procedures for estimating the biocompatibility of laser textured titanium surfaces are listed in the flow charts in Figure 3-5. The flow chart on the left in Figure 3-5 introduces the major steps of the cell culture, while the flow chart on the right presents the design of all experiments. In these experiments, human osteoblast-like cells - MG 63s were used. They exhibit numerous characteristics of osteoblasts that are unique to relatively immature osteoblasts, including stimulation of alkaline phosphatase activity and osteocalcin synthesis [90]. Therefore, they are the preferred models to examine the early stage of osteoblast differentiation.

For the first set of experiments, all surface patterns, uniform grooves and gradients, as well as control (polished) samples were tested and cultured for 1, 3 and 7 days after being immersed in 99% ethanol for 1 day or exposed to ambient air for 7 days, respectively. For the second set of experiments, groove spacings of 4.8 μm and 2.4 μm, irregular surface structure (gradients) and the control sample were cultured for 1 and 3 days after exposure to air for 10 days. Samples used in the second set were cultured for only one day after being exposed to air for 21 days. There were at least three samples prepared per surface pattern per condition in each set of experiments to test for repeatability.

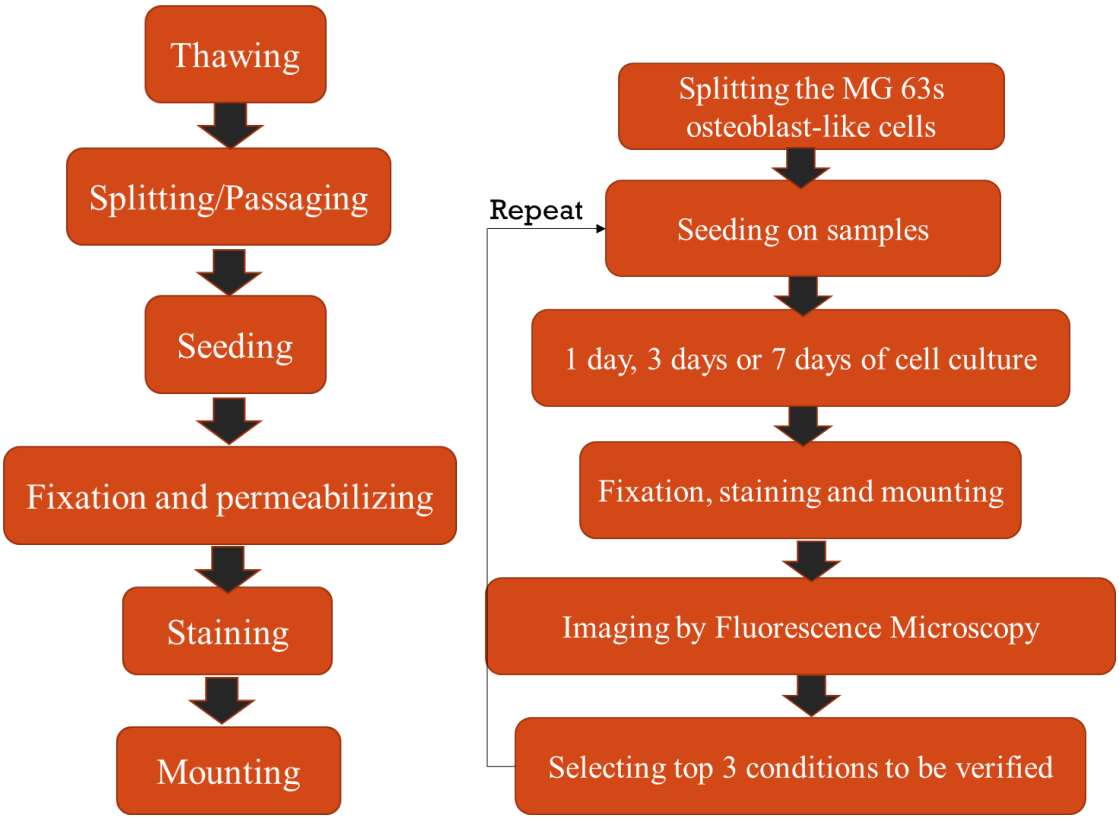

Figure 3-5 Flow charts of (left) Procedures of cell culture and (right) Design of biological experiments.

3.3.1 Cell culture

The experiments of cell culture including thawing, splitting and seeding were carried out by Dr. Alex Steeves at the surface nanostructure lab (SNL), University of Ottawa. Since the cell manipulation was implemented in a biological safety cabinet (BSC), the BSC was properly disinfected and sterilized with 70% ethanol and 30-second UV light in order to avoid contamination during the cell culture. Prior to cell culture, the cp Ti specimens were cleaned in a 70% ethanol bath for 2 hours. Then, the samples were deposited on 24-well plates and washed twice with a sterile phosphate buffered saline solution (1x, PBS).

All experiments were performed by using MG 63s osteoblast-like cells, which were acquired from Surface Nanoengineering Lab (SNL), University of Ottawa. Cell were thawed and transferred into a fresh 15 mL Falcon tube with enough volume of complete culturing media (CCM). CCM was mixed with Dulbecco's modified eagle media (DMEM) containing L-glutamine, non-essential amino acids, penicillin and streptomycin, and 10% fetal bovine serum (FBS). The cell suspension was transferred to a fresh 75 cm^2 cell culture flask and put

in the incubator at 37°C. Confluence of cells was verified by optical microscopy. The cells were detached by using Trypsin-EDTA (0.25%) and incubated for 6 to 8 minutes. When the cells were detached, CCM and triturate were added to prevent cells from clumping, and to obtain a homogenous cell suspension. The concentration of cells was counted using a hemocytometer, and the mother suspension of cells was diluted to a specific concentration for the experiments.

For all experiments, MG 63s cells were seeded at a density of about 5 x 10^4 cells/cm^2 on each well plate and incubated at 37°C in a humidified 5% CO_2 atmosphere for 24h (1 day), 72h (3 days) and 7 days. The culture media was replaced every three days. Cell adhesion was evaluated after 24h (1 day), and cell proliferation was evaluated after 72h (3 days) and 7 days. The experiments were performed in triplicate, in which there were 3 specimens per group.

3.3.2 Cell fixation and staining

After the samples were cultured for experiment-specific times, samples were removed from the incubator. The medium was removed from the wells with much care not to disturb the cells, and 1 x PBS was immediately added into the wells by using the side of the well to reduce shear across the surface containing the cells. The specimens were incubated at room temperature for 10 minutes and washed three more times using PBS. The 0.25% Triton X-100 solution mixed with PBS was prepared and added into the wells. The wells were incubated for 10 minutes at room temperature.

Staining of F-actin fiber filaments and cell nuclei is obtained by mixing PBS with DAPI and Rhodamine. The 0.25% TX-100 solution was removed from the wells, and the dying solution was immediately added into the wells. After that, the samples were incubated for at least 45 minutes as room temperature. Aluminum foil was used to protect samples from light since the dyes are photosensitive. After 45 to 60 minutes, the solution was removed from the wells, and the wells were cleaned twice with PBS before mounting. Rectangular coverslips were used and cleaned with Kimi wipes to remove any dust. Vectashield Hardset (mounting media) was added to the surface of the coverslips, and then one sample was taken from the well without extra liquid by dabbing its edge lightly on a paper towel (Kimi wipes) and inverted onto the Hardset. By using tweezers to push the samples down, the excess liquid or

air bubbles were squeezed out from between the sample-glass coverslip. All mounted samples were labeled and cured overnight at room temperature without any light.

3.3.3 Characterization of osteoblast cells and data analysis

The characterization of cell morphology was implemented using a Nikon Ni-U Radiometric Fluorescence Microscopy with Dual Excitation Sources which belongs to the Cellular Imaging and Cytometry Facility, University of Ottawa. Three Ti samples in each group were collected and up to three images were taken in the central area of the samples and the average cell number and area were calculated. Based on the excitation wavelength of DAPI and Rhodamine, the blue circular-like particles are cell nuclei, and F-actin fibers filaments are shown in red. Two magnifications are used during imaging, which are 10x for analysis of cell number and area and 20x for cell morphology. All images are in RGB scale.

Image processing was accomplished using the free software ImageJ, where the cell number and cell nuclei area were analyzed. The specific operation process is shown in Figure 3-6. After an image showing cell nuclei was opened in ImageJ, it was transformed from an RGB color image into a 16-bit black and white image. To do, so a threshold was applied and adjusted in order to clearly separate the regions of interest (ROI) from the background. The function “Analyse Particles” was used for automatic quantification of various parameters, such as cell number, cell nuclei area and percentage of cell nuclei area. Since the incubation time is as long as 7 days, cells accumulated together, therefore some cell nuclei were shown to be connected with each other in images, which may result in errors in automatically counting particles. Because of this, cell nuclei area and percentage of cell nuclei area were extracted as well to explain the proliferation and growth of cells as they are independent of whether cell nuclei are touching or not. As for the statistical analysis of results, the error bar of standard errors was calculated based on at least three samples and used in all bar charts.

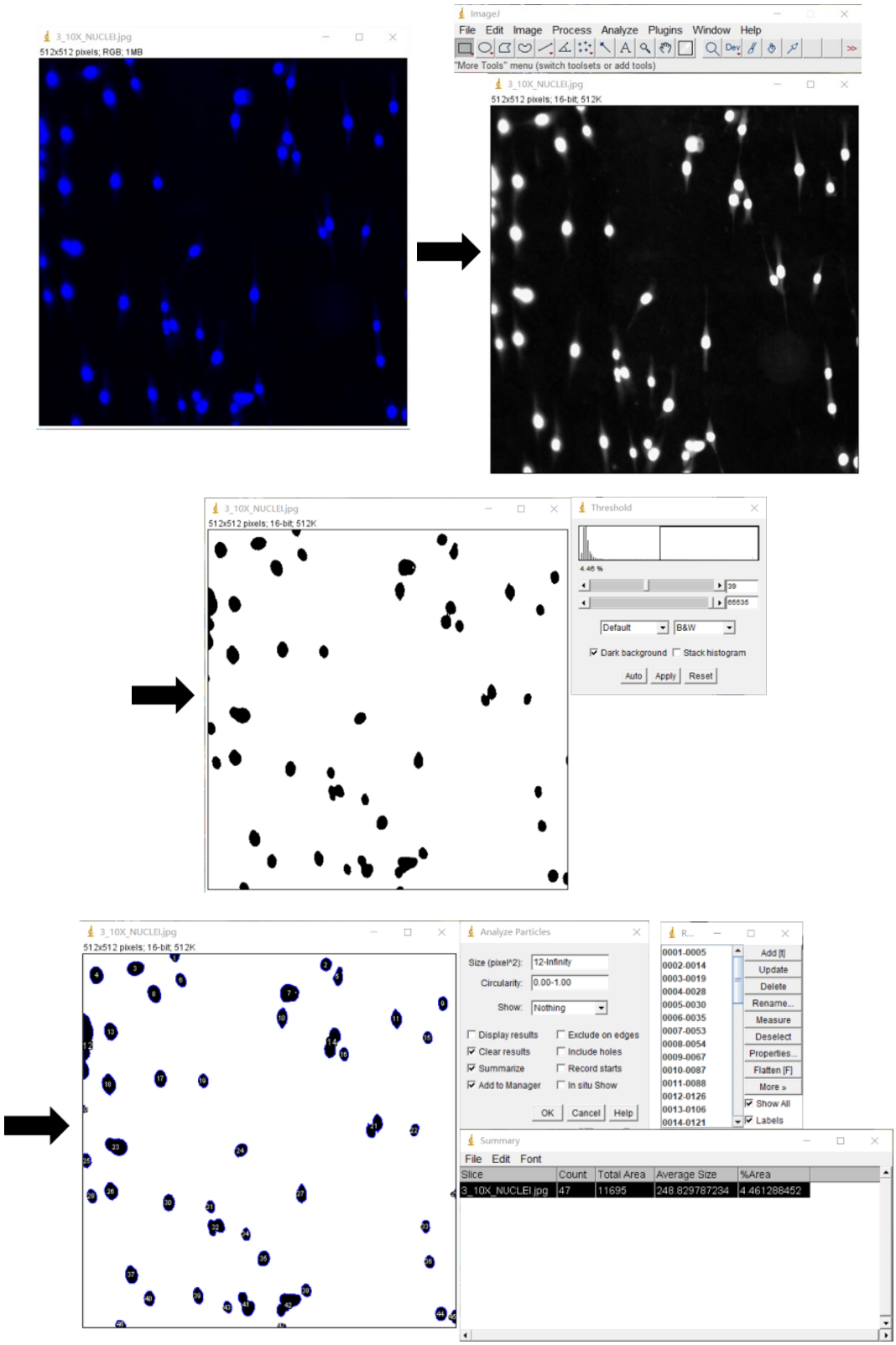

Figure 3-6 Procedures of analyzing cell number by ImageJ software.

4. Results and Discussion

This section is divided into four parts according to the order in which the experiments were carried out:

1. Morphology of laser textured surfaces. The microstructure and surface roughness are presented, and the effect of laser process parameters on surface topography is discussed.
2. Effect of storage environment, time, and laser texturing parameters on chemical composition. XPS spectra of laser treated cp Ti samples are presented. High resolution images of titanium and carbon are analyzed. The three storage conditions investigated were ethanol for 1 day, air for 7 days and air for 4 weeks. The effect of storage environment and aging time is discussed.
3. Effect of storage environment, time, and laser texturing parameters on surface wettability. The evolution of contact angle over time on laser textured Ti surfaces is investigated. Contact angle measurements were also carried out on samples stored in different environments (air, ethanol, and rough vacuum). The link between surface chemistry and wettability is also investigated.
4. MG 63s osteoblast-like cells response. Fluorescence images of cell morphology and statistics of cell number and cell area caused by surface topography, storage conditions and incubation time are described. The effect of surface roughness, wettability and chemistry on cell behavior is discussed.

4.1 Surface topography

In this section, the effect of two major laser process parameters: laser beam power and line spacing, on surface morphology and roughness are discussed. These experiments were aimed at studying the relationship between laser process parameters and surface topography and to identify optimal morphologies for subsequent cell culture.

4.1.1 Surface morphology

One of the design criteria for the surface morphologies to be created on the Ti samples is the groove width, which needs to be no more than 1um in order to allow for closely spaced grooves. Since gradients included various line spacing from narrow to wide, the gradient configuration was selected for identifying the best combination of laser process parameters. A repetition rate of 200 kHz and scanning speed of 20 mm/s was chosen due to constraints in terms of sample dimensions and resulting machining time. Laser power was the first parameter investigated and gradients were produced with a laser beam power in the range from 2 mW to 5 mW at a repetition rate of 200 kHz. It should be noted that a 1 μm line spacing was close to the resolution of the microscope objective used and therefore, energies close to the ablation threshold were required. OM images of laser-induced gradients on titanium surfaces are presented in Figure 4-1. When the laser beam power was low at 2 mW (Figure 4-1 (a)), the sides of the grooves were clearly visible, and the line width is only 0.6 μm, but more breakpoints and unmachined areas were present on the surface. When the laser power was increased to 2.5 mW (Figure 4-1 (b)), the sides were still visible and the groove width was also increased to 1μm. Increasing the laser power from 3 mW to 5 mW (Figure 4-1 (c), (d) and (e)), the groove width increased to 1.2 μm and 1.6 μm respectively, resulting in grooves that were difficult to discern at the narrowest spacings (grooves are overlapping each other). However, the grooves were now continuous. Therefore, there were two values of laser beam power that met the requirements, which were 2 mW and 2.5 mW.

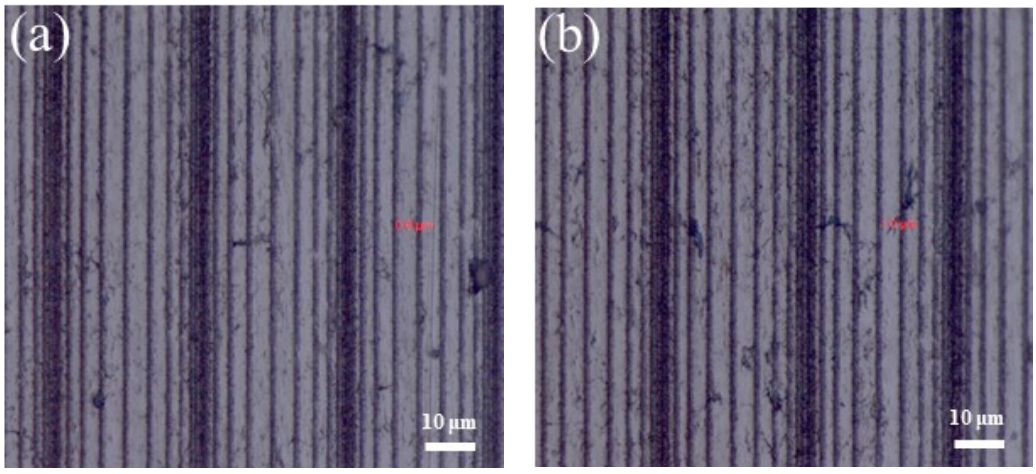

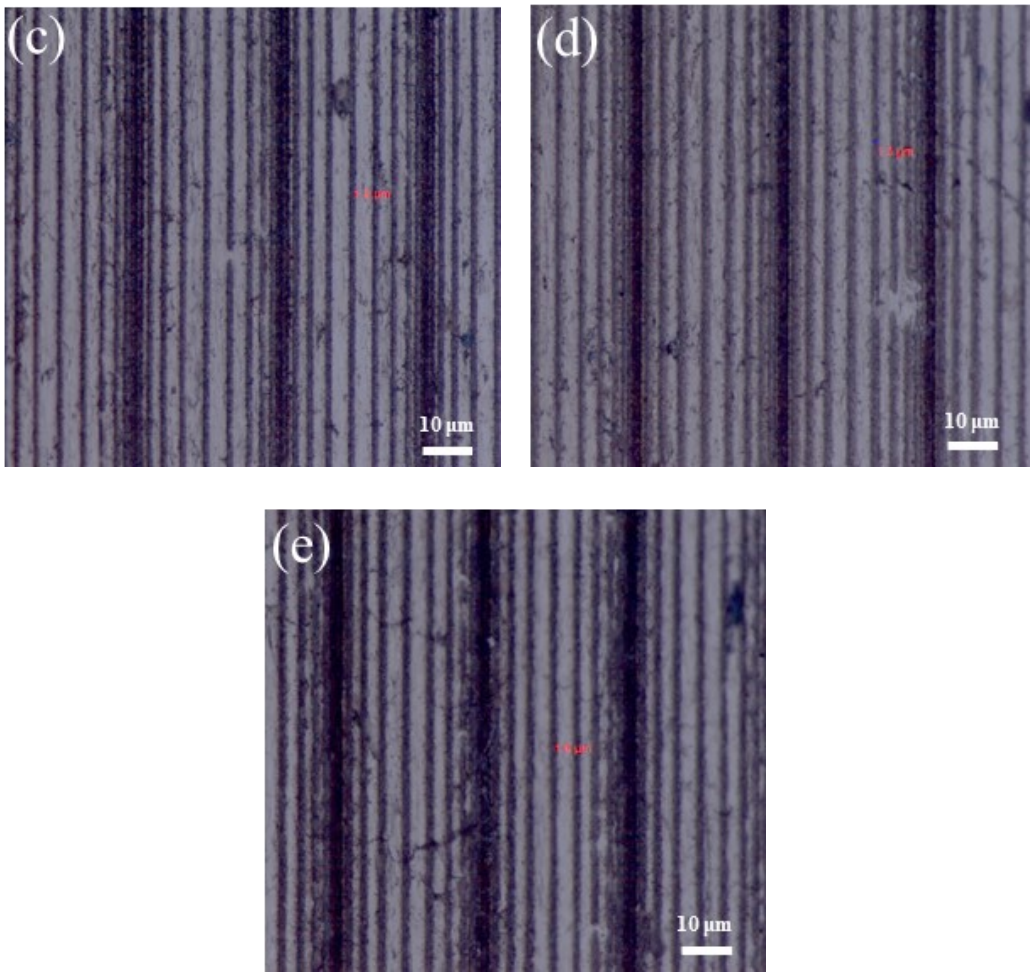

Figure 4-1 Optical microscopic images on different laser power; a) 2 mW, b) 2.5 mW, c) 3 mW, d) 4 mW, e) 5 mW.

In order to further verify the combination of laser beam power and line spacing, the two selected values of laser beam power (2 mW and 2.5 mW), and irregular surface structures with varying line spacing, from 1.2 µm to 6 µm and from 1.3 µm to 6.5 µm, were tested again, as shown in Figure 4-2. When the initial line spacing was 1.2 µm (Figure 4-2 (a) and (c)), the edges of grooves were clearly seen both at 2 mW or 2.5 mW when the line spacing was the narrowest. Although in some areas, the sides of two adjacent lines were tightly connected at the laser beam power of 2.5 mW. When the initial line spacing was increased to 1.3 µm, the performance was as good as that at line spacing of 1.2 µm when the laser beam power was 2 mW. When the laser beam power was 2.5 mW, there appeared to be more debris on the edges of the grooves. The requirements of surface microstructure were to use the narrowest line spacing, reduce the laser ablated area and thickness of the oxide layer, and create shallow

groove depth. Therefore, the line spacing of 1.2 μm was confirmed as the narrowest groove spacing for regular surface structure and initial groove spacing for gradients, and the laser beam power of 2 mW was chosen.

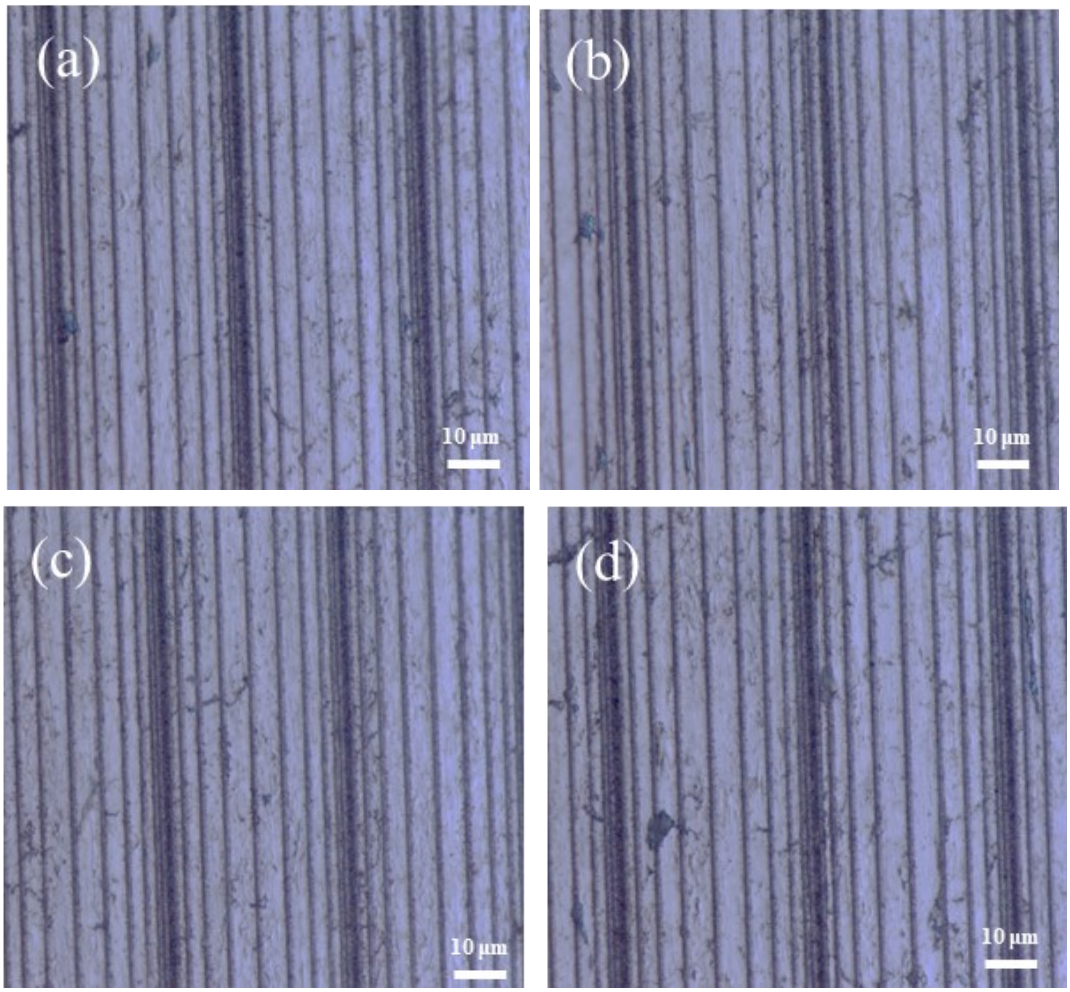

Figure 4-2 OM images of different line spacing and laser power. a) 1.2 μm line spacing with laser power of 2 mW, b) 1.3 μm line spacing at 2 mW, c) 1.2um line spacing at 2.5 mW, d) 1.3 μm line spacing at 2.5 mW.

The microstructure of uniform grooves and gradients induced by femtosecond laser surface texturing is presented in Figure 4-3. The percentage of surface area covered by laser textured grooves is calculated in Table 4-1. The percentage of machined area was calculated by the area of each groove with an average width of 1 μm and length of 9.7 mm and the total number of grooves on the surfaces. For grooves at line spacing of 10 μm (Figure 4-3 (a1), (a2)), the distribution of each line was very uniform, the rate of repeatability was higher, and about 9.7±0.2% surface was covered with grooves. It is clear that the debris was accumulated at the edges of lines, and more was deposited at the bottom of each line according to the internal

microstructure at high magnification (Figure 4-3 (a2)). Most importantly, there were still some high spatial frequency LIPSS (HFLS) formed at the bottom of grooves. Unmachined area between two grooves was relatively clean without much debris. The surface microstructure of other regular surface features and gradients was similar or almost the same. The main difference was the percentage of machined area, which was 20.21±0.4%, 40.41±0.8% and 80.83±1.6% at line spacing of 4.8 μm, 2.4 μm and 1.2 μm, respectively, as well as 29.57±0.6% for gradients.

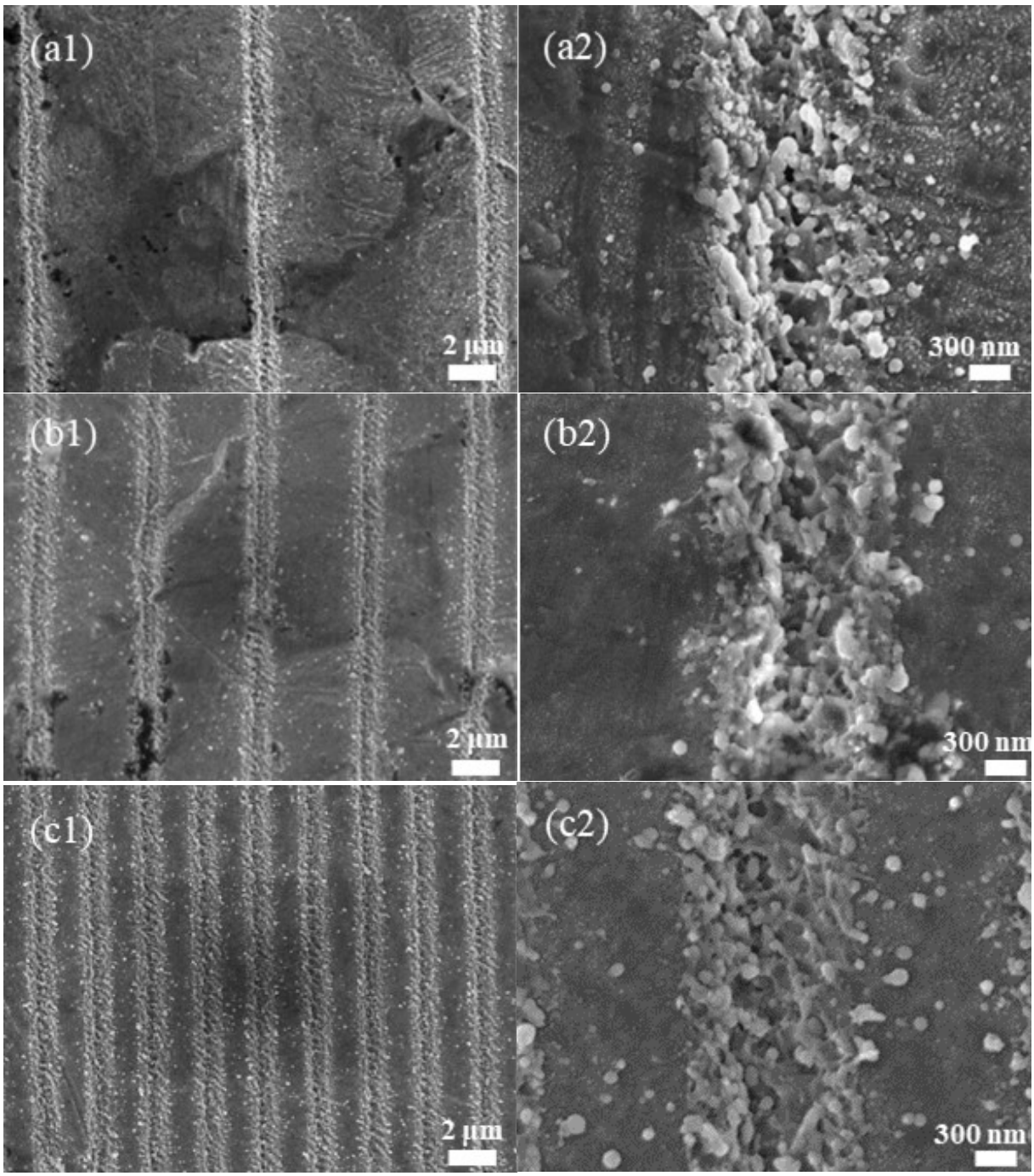

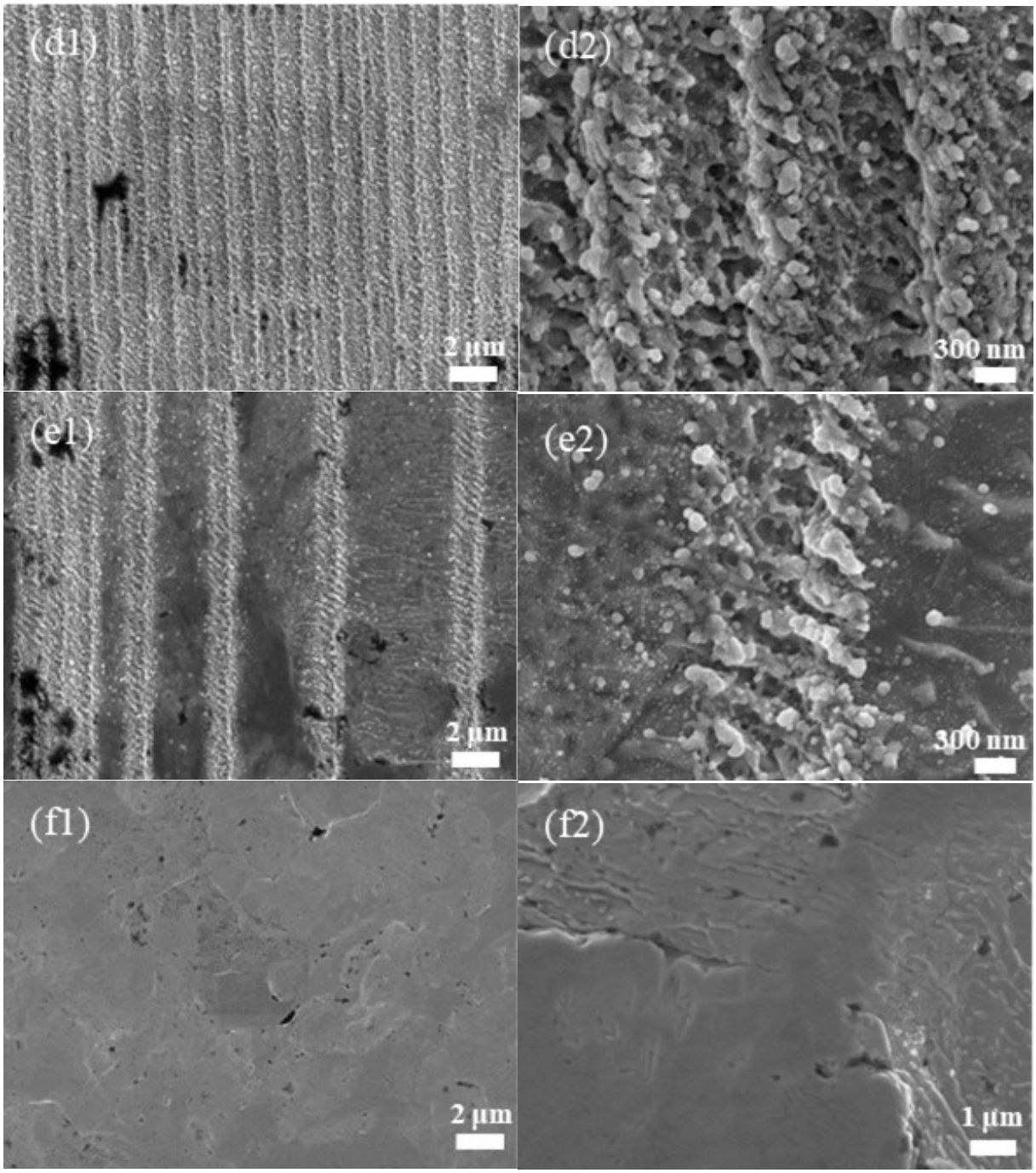

Figure 4-3 SEM images of laser treated surface microstructure at lower magnification of 5 kx and higher magnification of 30kx; (a1)(a2) 10 µm; (b1)(b2) 4.8 µm; (c1)(c2) 2.4 µm; (d1)(d2) 1.2 µm; (e1)(e2) gradients; (f1)(f2) polished.

Table 4-1 Percentage of surface coverage of laser textured area on cp Ti surfaces with different surface structures

Line Spacing (um)	Surface Coverage (%)
10	9.7±0.2
4.8	20.21±0.4
2.4	40.41±0.8
1.2	80.83±1.6
Gradients	29.57±0.6

Overall, the grooves were uniformly distributed on the surface, and the morphology of the grooves were very similar, which attested to the reproducibility of the femtosecond laser texturing process. The internal microstructure consisted of deposited nanoparticles and other ablated debris with the presence of some ripples at the bottom of the grooves. The surface coverage of the laser textured area increased with decreasing line spacing.

4.1.2 Surface roughness

The surface roughness of samples covered with uniform grooves and gradients was measured by AFM, and a typical 3D model of the surface structure is presented in Figure 4-4. The width of the grooves was unchanged when changing line spacing, and was approximately 1 μm. As shown in Figure 4-4, when the line spacing was 10 μm, the average groove depth of this surface structure was about 220 nm. With decreasing line spacing, the grooves are deeper and reach a depth of more than 250 nm. Another phenomenon that could be deduced was that the surface topography is smoother, and the machined area is larger with the lower line spacing.

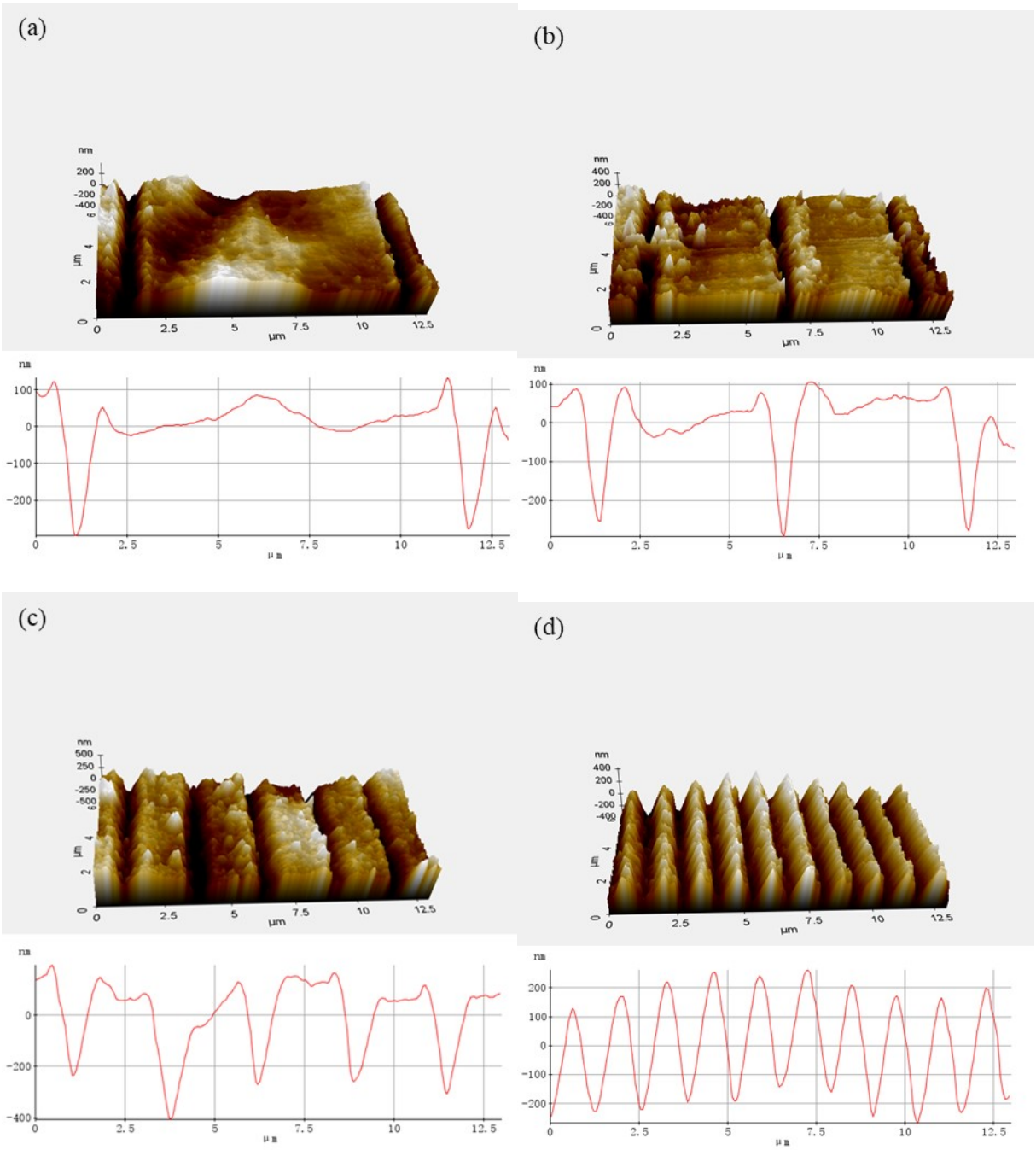
(a)
(b)
(c)
(d)
nm
µm
µm

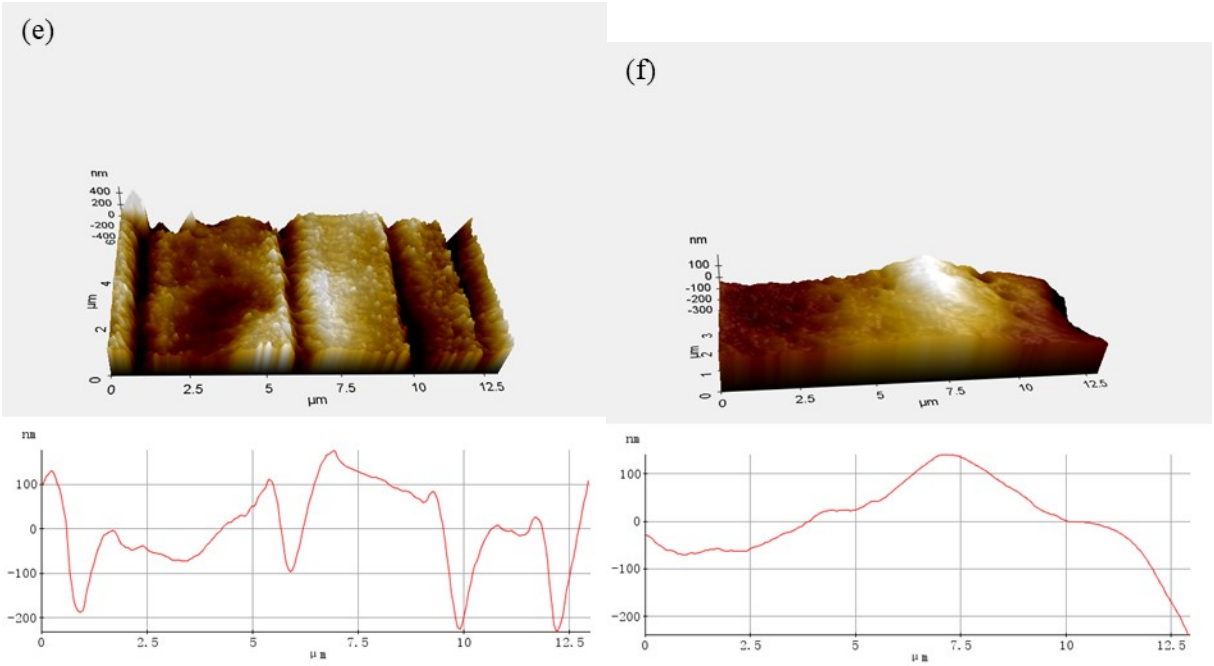

Figure 4-4 Surface topography of different laser parameters; (a) 10 μm; (b) 4.8 μm; (c) 2.4 μm; (d) 1.2 μm; (e) gradients; (f) polished.

Table 4-2 presents several surface roughness parameters extracted from the AFM scans. Ra, Rq and Rz parameters are given according to scanned areas of each condition. The parameter Ra indicates the arithmetic mean roughness, and Rq provides the roughness of root mean square, while the Rz presents average peak-valley results (distance from the highest point of peak to the lowest point of valley). It is obvious that the narrower the groove spacing was, the rougher the textured surface was. The surface roughness of grooves at 4.8 μm was close to that of gradients since the middle value of line spacing was 3.6 μm. Even though, from Figure 4-4 (f), the surface topography of 1.2 μm was smoother, the large number of grooves resulted in the highest surface roughness.

Table 4-2 Surface roughness parameters of laser textured Ti surfaces

Laser Parameters	Ra (nm)	Rq (nm)	Rz (nm)
10 μm	31.9±6.7	46.7±4.3	140.6±16.6
4.8 μm	46.2±8.9	74.3±11.1	156.7±28.1
2.4 μm	79.6±8.4	104.0±5.3	193.1±20.0
1.2 μm	103.5±23.5	118.7±28.4	239.9±29.4
Gradients	38.2±3.4	55.7±6.1	217.6±20.1
Polished	2.4±0.9	2.9±0.9	8.4±1.5

Therefore, both surface topography and surface roughness were affected by the line spacing whereby smaller line spacings resulted in deeper grooves and smoother areas between grooves.

4.1.3 Discussion

Firstly, the laser beam power was confirmed by designed line width, which ensured the consistent structure of the grooves. Since the ablated depth was shallow, at about 100-200 nm, and the line width was narrow, at about 1um, the amount of removed material was small compared to the entire volume of samples.

According to the Gaussian laser beam profile, the change in the intensity was spatially dependent, where it changed over the length of pulse and peaked in the center of the pulse. Therefore, the material removal also followed this pattern. Since the energy in the central area of the laser spot was higher, it led to a deeper position below the surface of the material [107], and the cross-section of laser machined grooves was triangular (Figure 4-5).

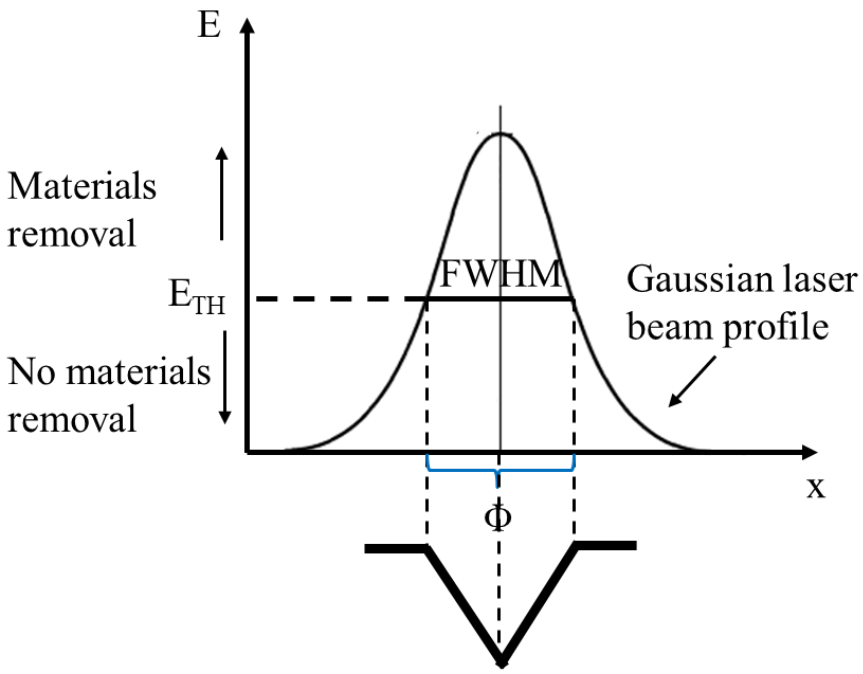

Figure 4-5 Scheme of Gaussian laser beam profile and cross-section shape of laser textured groove (E - Intensity, E_{TH} – Energy ablation threshold, Φ – Beam diameter).

The depth of the groove was affected by the groove spacing, as shown in Figure 4-6. There was an increase of groove depth with the decrease of groove spacing and reached the maximum when the groove spacing was 2.4 μm. The principle of laser surface texturing is to ablate the surface area in order to vaporize material to remove or form removable particles with the help of a fume extractor and subsequent ultrasonic cleaning. When the material is ablated, most of it is vaporized, while some is solidified into particles. These particles were ejected during the laser process; however, some were redeposited at the bottom of the grooves and next to the grooves, which resulted in the shallower grooves. Although, the heat affected zone (HAZ) was smaller in this research due to the lower laser beam power and because a femtosecond laser was used, the machined area and unmachined area could still be affected by a HAZ. This HAZ, which was expected to be only around a micron deep, would especially affect the smallest groove spacing. As for the depth of the machined area, debris and nanoparticles accumulated in the grooves during processing created roughness which would then absorb more of the incident laser beam which in turn would ablate more material and create deeper grooves. So, the closer together the grooves were, the more material was ablated and redeposited in the grooves, the more laser energy was absorbed by the nanoparticles and

debris in the groove, and the deeper the groove became. But when the groove spacing was too narrow, there were more debris accumulated on the edges of grooves, where the laser ablated the debris first and caused the shallower grooves, such as the groove spacing of 1.2 μm. Besides, when the two laser passes were too close, there was some overlapped area.

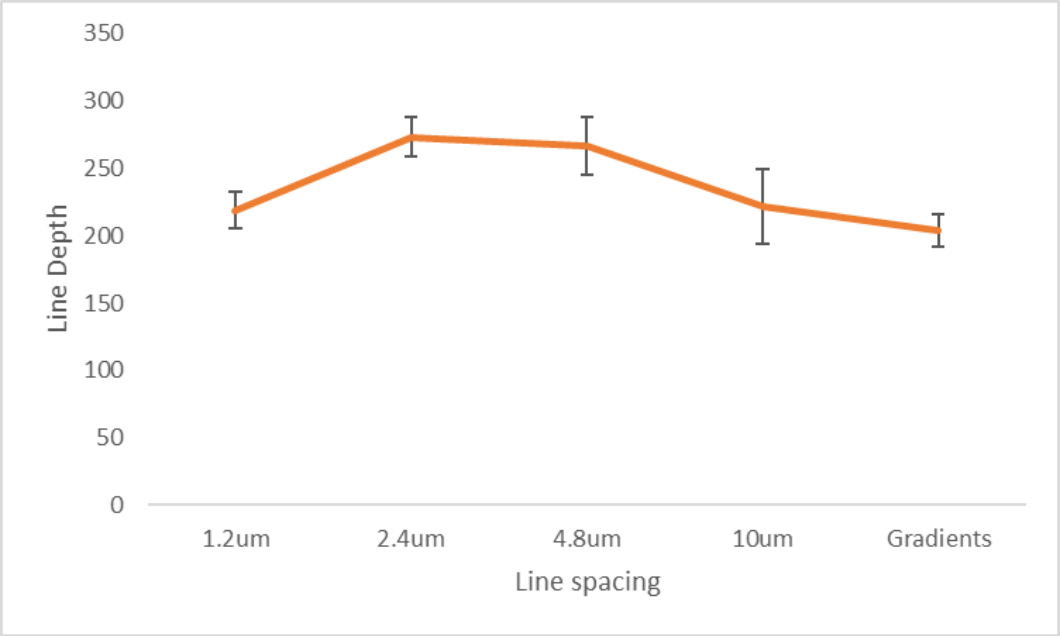

Figure 4-6 The change of line depth due to the increase of line spacing.

4.1.4 Summary

The main conclusion of this part can be summarized as followed:

1. The microstructure of each groove was uniform and reproducible.
2. There was a relationship between line depth and line spacing where closer lines accumulated more ablated material, resulting in more laser energy absorbed, more material ablated and thus deeper grooves.

4.2 Chemical composition of surface oxide layers

In this section, the effect of laser parameters and storage environment on surface chemistry is discussed. Surface chemistry is important as it may influence surface wettability and cell behavior.

The chemical composition of the laser-induced oxide layer, the oxide chemical state, and the relative abundance of other elements on the cp Ti sample surface when stored in different

environments was analyzed by XPS. The laser surface patterns investigated include uniform grooves at a line spacing of 4.8 μm and the gradient, as well as a polished surface. The storage conditions investigated include ethanol for 1 day, and air for 7 days and 4 weeks.

4.2.1 XPS survey spectra

Figure 4-7 presents XPS survey spectra of selected laser treated Ti samples. The dominant peaks of the survey spectra were C 1s peak, Ti 2p peak and O 1s peak at binding energies of 284.8 eV, 458 eV and 530 eV, respectively. The C 1s peak is mainly attributed to the presence of organic compounds absorbed from the air or from ethanol on the surface. The relative amount of titanium, oxygen and absorbed carbon was determined by the XPS survey spectra as shown in Table 4-3. The relative carbon content for samples stored in air for 7 days was the lowest, with 25%, 33%, 36% for the polished surface, irregular structure and regular structure, respectively. But it increased to about 50% when the samples were exposed to air for 4 weeks. The change in relative content of titanium was opposite that of carbon, with a decrease with storage time. The highest relative content of titanium was 20% detected on the polished surface after storage in air for 7 days, while the lowest value was 9.5% for the surface with gradients after immersion in ethanol for 1 day. The relative oxygen concentration on the laser treated surface also decreased over time. For instance, oxygen content decreased from 48% to 40% on the surface with regular structures when increasing storage time in air from 7 days to 4 weeks.

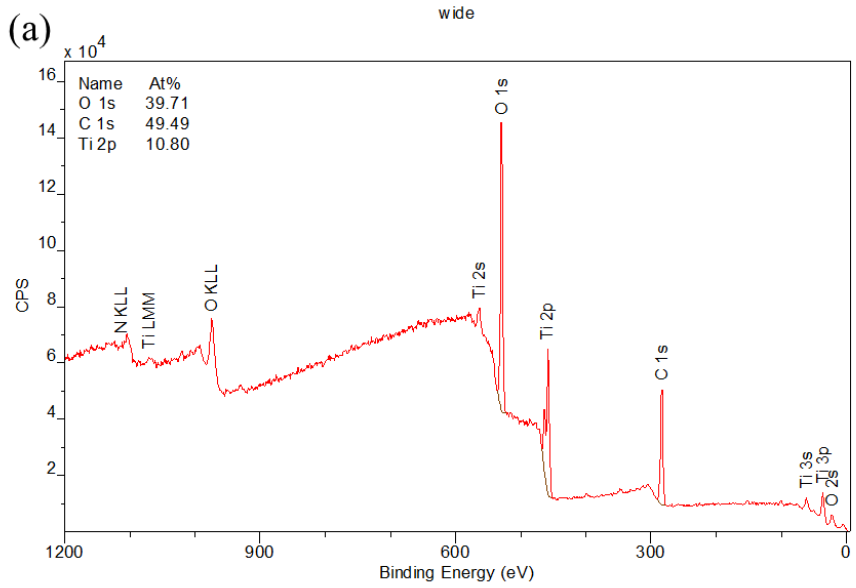
(a)
wide
x 10^4
Name At%
O 1s 39.71
C 1s 49.49
Ti 2p 10.80
CPS
N KLL
Ti LMM
O KLL
Ti 2s
O 1s
Ti 2p
C 1s
Ti 3s
Ti 3p
O 2s
Binding Energy (eV)

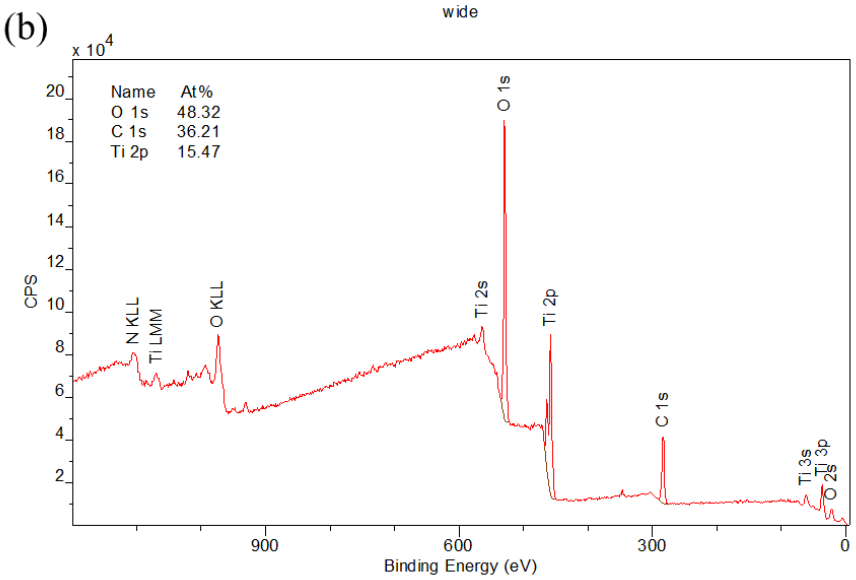
(b)
wide
x 10^4
Name At%
O 1s 48.32
C 1s 36.21
Ti 2p 15.47
CPS
N KLL
Ti LMM
O KLL
Ti 2s
O 1s
Ti 2p
C 1s
Ti 3s
Ti 3p
O 2s
Binding Energy (eV)

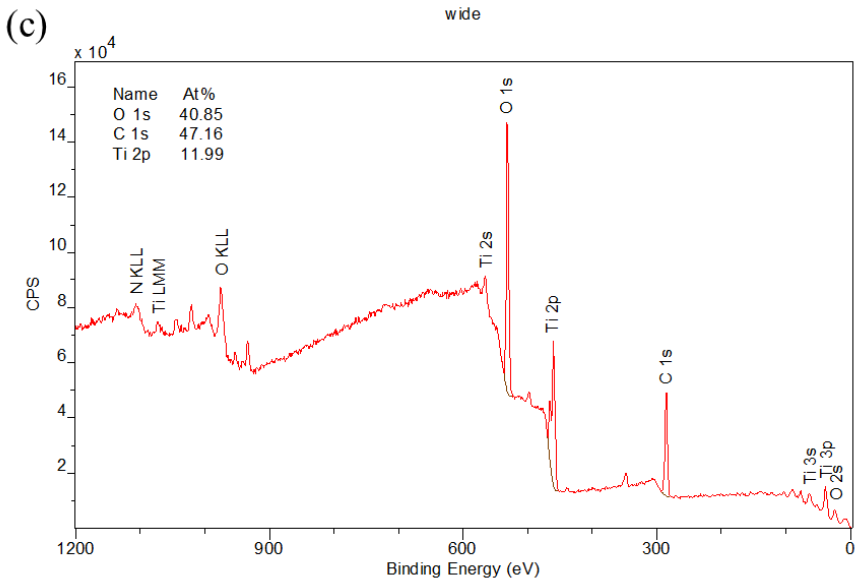

Figure 4-7 XPS survey spectra of laser treated Ti samples at line spacing of 4.8 µm that were stored (a) in air for 4 weeks (b) in air for 7 days, and (c) in ethanol for 1 day.

Table 4-3 Atomic percentage of elements in XPS survey spectra.

Elements/At%	Surface patterns and storage conditions							
	Air 4w		Air 7d			Ethanol 1d		
	4.8	G	4.8	G	P	4.8	G	P
C	49.49	53.73	36.21	33.38	25.03	47.16	47.30	52.77
Ti	10.80	9.89	15.47	17.52	20.04	11.99	9.48	12.92
O	39.71	36.37	48.32	49.10	54.39	40.85	43.22	34.31

In general, carbon content for laser treated Ti surfaces was the highest when they were stored in air for 4 weeks. Besides, the carbon content increased with increasing storage time in air, which corresponded to a decrease in oxygen and titanium.

4.2.2 Change in carbon content

In order to analyze the qualitative variations of chemical composition on Ti surfaces before and after laser machining in more detail, high resolution spectra of the C 1s region is shown in Figure 4-8. Adventitious carbon contamination is often used as a charge reference for XPS spectra. The C 1s spectra for contamination typically contains functional groups hydrocarbon chains (C-C, C-H), alcohols/ether (C-OH, C-O-C), aldehydes/ketones (C=O) and

carboxyl/ester (O-C=O) at binding energies of 284.8 eV, 286.3 eV, 287.8 eV and 288.8 eV, respectively [108]. The C-C/H functional group is considered non-polar and contributes to hydrophobicity, while the other three functional groups are highly polar and contribute to hydrophilicity [78]. Therefore, the relative concentration of C-C/H bonds on the surface can be used as an indicator to explore the surface wettability. Besides, the observed carbon may be related to other non-polar functional groups including methylgroup-CH_3 and/or graphite carbon contributing to hydrophobicity [109]. The collective effect of C-C/H bonds and CH_3 bonds are responsible for the hydrophobicity of laser treated Ti surfaces over time.

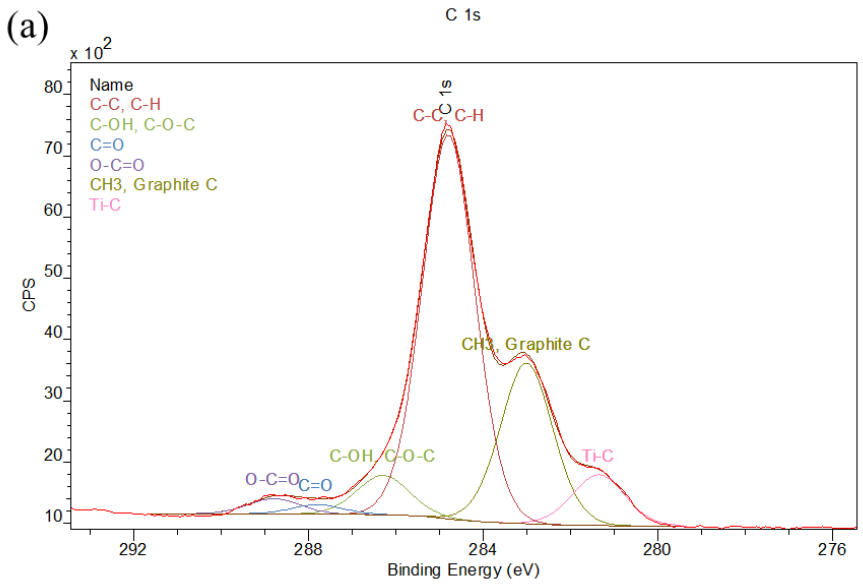

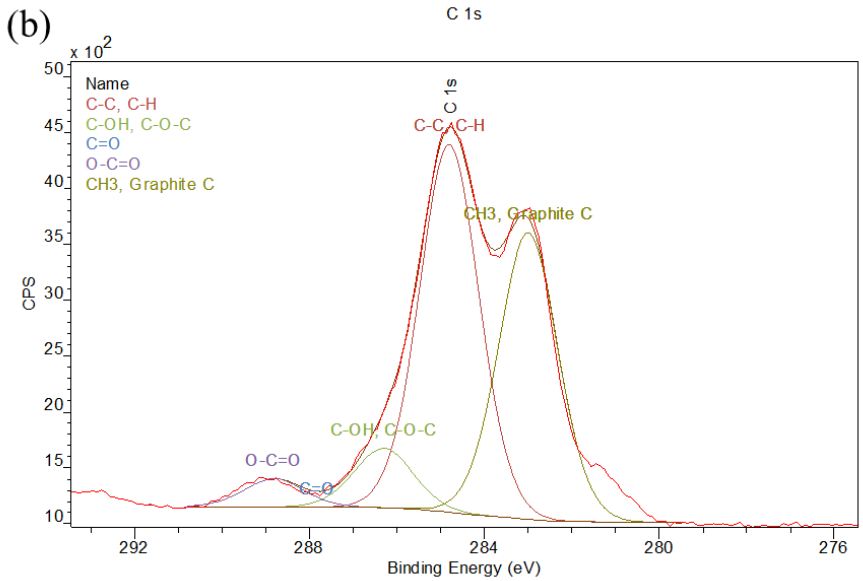

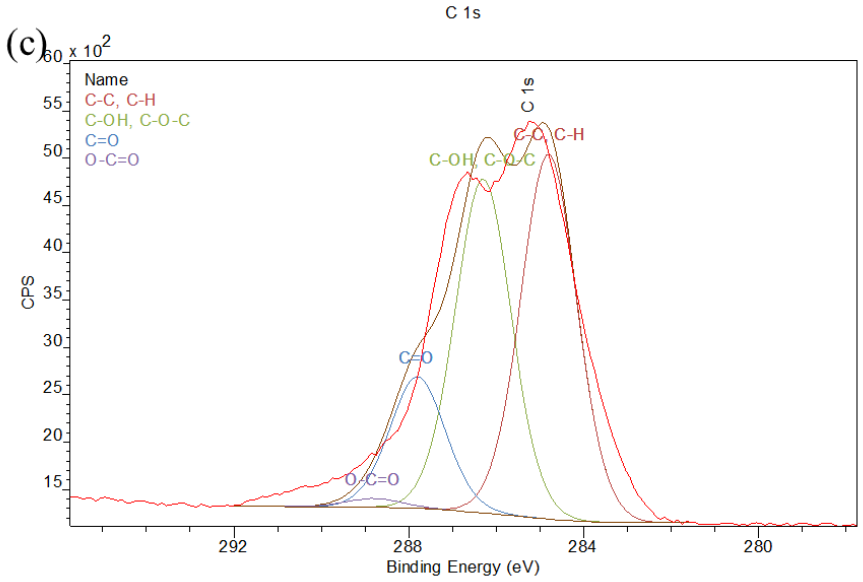

Figure 4-8 High resolution XPS spectra of C 1s region for laser treated Ti samples at line spacing of 4.8 μm that were stored (a) in air for 4 weeks (b) in air for 7 days, and (c) in ethanol for 1 day.

The percentage of these functional groups in the C 1s region obtained by XPS are summarized in Table 4-4. For samples stored in air, the functional group C-C/H was the most abundant, with 82% observed on the polished surface after exposure to air for 7 days. The concentration of C-C/H groups on laser treated surfaces (50%~64%) was much smaller because of the presence of other functional groups, -CH_3 and graphite C, which contributed to 39% and 22% on surfaces with uniform grooves and gradients, respectively. After a longer period of exposure to air, another bond, C-Ti, appeared on the laser treated surfaces, with 8% and 11% for laser treated surfaces with uniform grooves and gradients, respectively. The total amount of functional groups that contributed to hydrophilic behavior decreased over storage time in air, going from 14% to 5% for gradient structure and from 12% to 10% for regular surface structure. The dominant groups were C-OH or C-O-C when samples were stored in ethanol, where the total amount of these hydrophilic functional groups contributed to 68%, 76% and 57% for the polished surface, gradients and regular surface structures, respectively.

Table 4-4 Percentage of functional groups in XPS C 1s high resolution spectra

Functional Groups/At%	Surface patterns and storage conditions							
	Air 28d		Air 7d			Ethanol 1d		
	4.8	G	4.8	G	P	4.8	G	P
C-OH, C-O-C	5.99	2.69	8.74	8.62	7.18	30.09	37.81	26.38
C=O	1.44	0.27	0	0	4.52	30.11	31.26	41.91
O-C=O	2.34	2.25	3.77	5.25	5.87	16.42	5.99	0
C-C, C-H	58.21	58.80	46.33	61.07	82.43	23.39	24.94	31.71
-CH_3, Graphite C	24.32	25.24	36.37	20.29	-	-	-	-
C-Ti	7.70	10.75	4.80	4.76	-	-	-	-

In general, the laser treatment reduced the C-C/H concentration on the surfaces. The dominant functional group was C-C/H bond under air storage conditions, while C-OH or C-O-C bonds dominated on the surface under ethanol storage conditions. There was no clear trend for the change in C-C/H, -CH_3 and graphite C concentration over time. Besides, laser treatment increased the presence of C-Ti bonds as well as CH_3 and/or graphite C components.

4.2.3 Titanium valence transition

The XPS high resolution spectra of Ti 2p region for laser treated Ti samples is presented in Figure 4-9, which is related to the surface patterns of uniform grooves. Four Ti 2p doublets with a spin-orbit of 5.72 eV or 6.05 eV for oxide or metal were fitted. The main components of major doublets were Ti $2p_{3/2}$ and Ti 2p1/2 of Ti^{4+} in TiO_2, which were centered at 458.8 eV and 464.22 eV. Other doublets centered at 457.1 eV and 462.82 eV can be assigned to Ti $2p_{3/2}$ and Ti $2p_{1/2}$ of Ti^{3+} in Ti_2O_3, and the other at binding energies of 455.3 eV and 461.02 eV assigned to the Ti $2p_{3/2}$ and Ti $2p_{1/2}$ peaks of Ti^{2+} in TiO. In addition, two components centered at 453.55 eV and 459.60 eV can be assigned to Ti $2p_{3/2}$ and Ti $2p_{1/2}$ of metallic Ti.

(a)

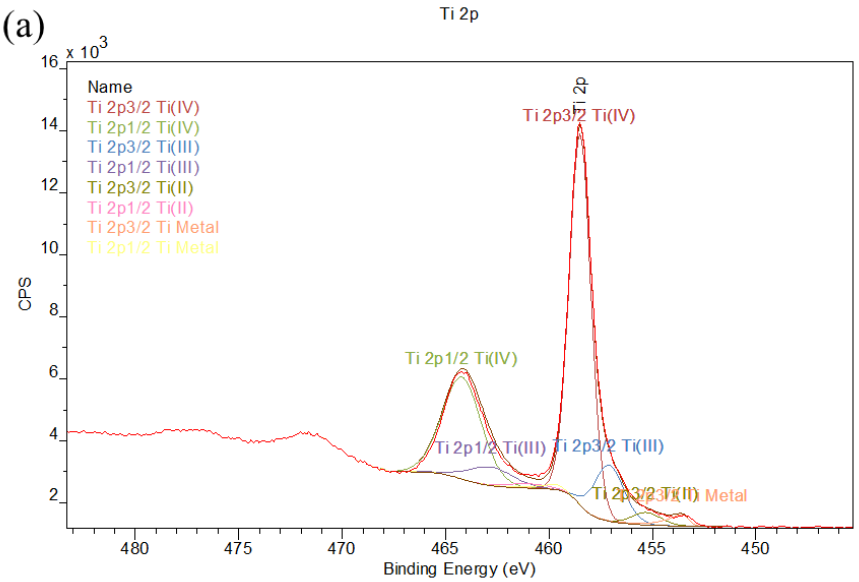
Ti 2p
x 10^3
Name
Ti 2p3/2 Ti(IV)
Ti 2p1/2 Ti(IV)
Ti 2p3/2 Ti(III)
Ti 2p1/2 Ti(III)
Ti 2p3/2 Ti(II)
Ti 2p1/2 Ti(II)
Ti 2p3/2 Ti Metal
Ti 2p1/2 Ti Metal
CPS
Ti 2p
Ti 2p3/2 Ti(IV)
Ti 2p1/2 Ti(IV)
Ti 2p1/2 Ti(III)
Ti 2p3/2 Ti(III)
Ti 2p3/2 Ti(II)
Ti 2p3/2 Ti Metal
Binding Energy (eV)

(b)

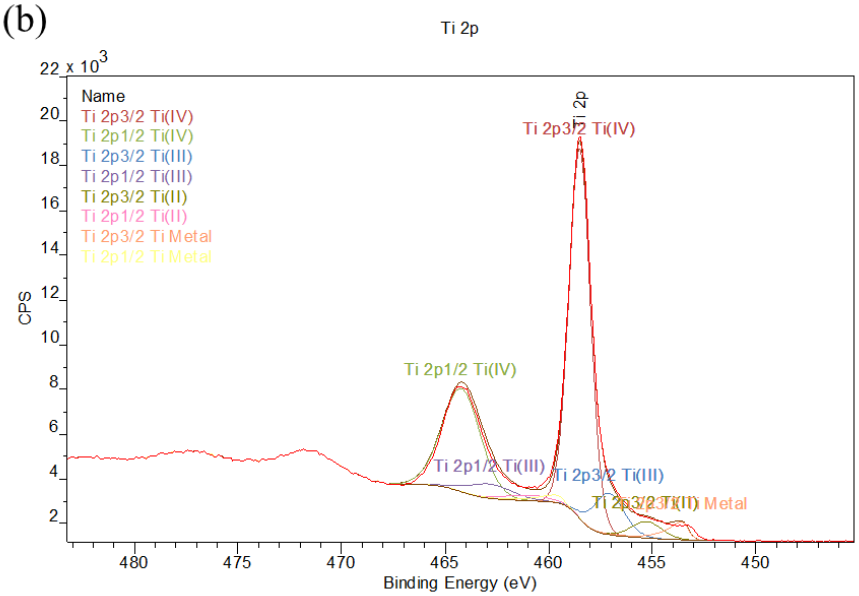
Ti 2p
22 x 10^3
Name
Ti 2p3/2 Ti(IV)
Ti 2p1/2 Ti(IV)
Ti 2p3/2 Ti(III)
Ti 2p1/2 Ti(III)
Ti 2p3/2 Ti(II)
Ti 2p1/2 Ti(II)
Ti 2p3/2 Ti Metal
Ti 2p1/2 Ti Metal
CPS
Ti 2p
Ti 2p3/2 Ti(IV)
Ti 2p1/2 Ti(IV)
Ti 2p1/2 Ti(III)
Ti 2p3/2 Ti(III)
Ti 2p3/2 Ti(II)
Ti 2p3/2 Ti Metal
Binding Energy (eV)

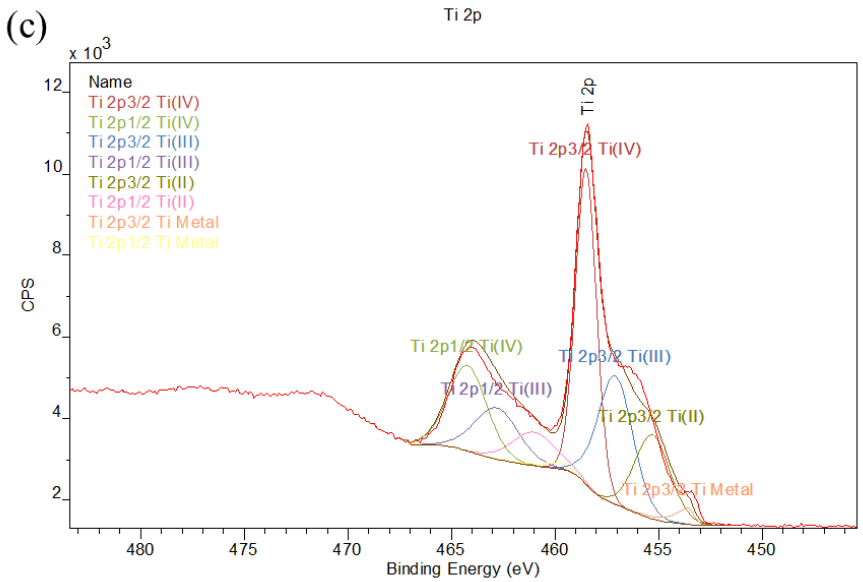

Figure 4-9 High resolution XPS spectra of Ti 2p region for laser treated Ti samples at line spacing of 4.8 μm that were stored (a) in air for 4 weeks (b) in air for 7 days, and (c) in ethanol for 1 day.

The percentage of titanium in different valence states obtained by XPS is summarized in Table 4-5. In general, the concentration of metallic Ti for polished surfaces was higher, 17% and 7% under ethanol and air storage respectively, compared with laser treated Ti surfaces. Under the ethanol storage environment, the Ti^{4+} concentration was lower; 46% for uniform grooves and 42% for gradients, compared with those under air storage. The concentration of Ti^{4+} increased a little bit when exposed to ambient environment over time, for example, from 77% to 81% for gradient surface structure. There was a slight change in Ti^{4+} concentration and an obvious increase in Ti^{3+} concentration with a decrease in concentration of Ti^{2+} and metallic Ti for surfaces with uniform grooves.

Table 4-5 Percentage of titanium in different valence state

Valence/At%	Surface patterns and storage conditions							
	Air 4w		Air 7d			Ethanol 1d		
	4.8	G	4.8	G	P	4.8	G	P
Ti^{4+}	77.39	80.61	78.06	77.04	81.25	45.57	42.27	74.68
Ti^{3+}	16.12	11.52	12.37	13.71	9.39	31.33	24.02	12.77
Ti^{2+}	3.60	2.40	5.06	5.74	2.51	20.50	27.70	1.71
Metallic Ti	2.89	5.46	4.52	3.50	6.85	2.60	6.01	10.84

In general, laser treatment helped to promote the transformation of Ti valence states on the Ti surfaces. And long-term exposure in ambient environment were able to further oxidize the Ti surfaces, while ethanol storage environment slowed down the transformation of Ti valence states.

4.2.4 Oxygen content

Regarding the O 1s region, three components can be found for all spectra at 530 eV, 531.3 eV and 532.9 eV, which can be assigned to lattice oxide (O^{2-}), hydroxides (-OH) and organic oxide (O-C=O), respectively, as shown in Figure 4-10. The relative percentage of these functional groups on the tested Ti surfaces is summarized in Table 4-6. In the air storage environment, the O^{2-} concentration was higher due to the oxidation of pure titanium. For example, surfaces with 4.8 um line spacing had 91% of O^{2-} when exposed to air for 4 weeks. However, the O^{2-} concentration was only 39% for the surface immersed in ethanol for 1 day but with 51% hydroxides and 10% absorbed water and/or organic O. The phenomenon was the opposite to that of the polished surface, where O^{2-} component was dominant whether stored in air or in ethanol. In general, the relative concentration of absorbed hydroxyl group and O-C=O was higher when the samples were immersed in ethanol. Therefore, laser treatment increased the possibility of absorption of -OH and O-C=O components when immersed in ethanol.

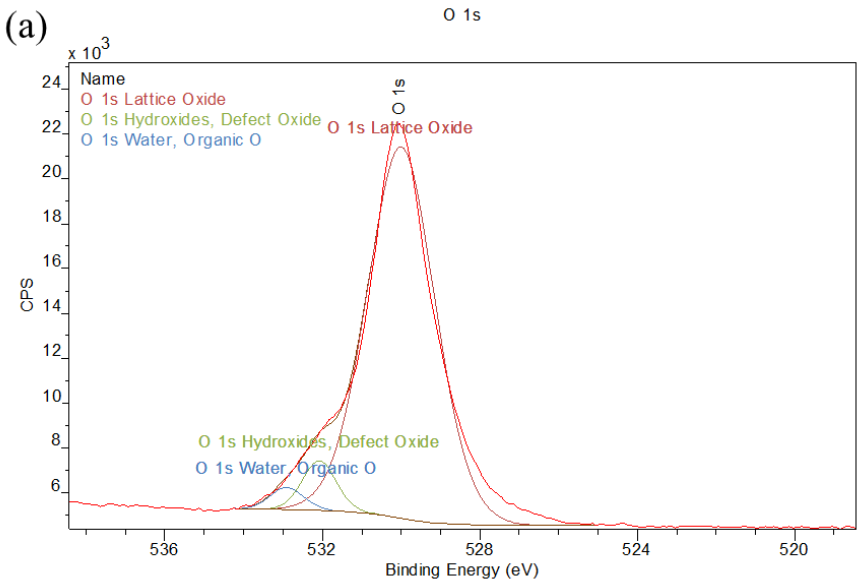

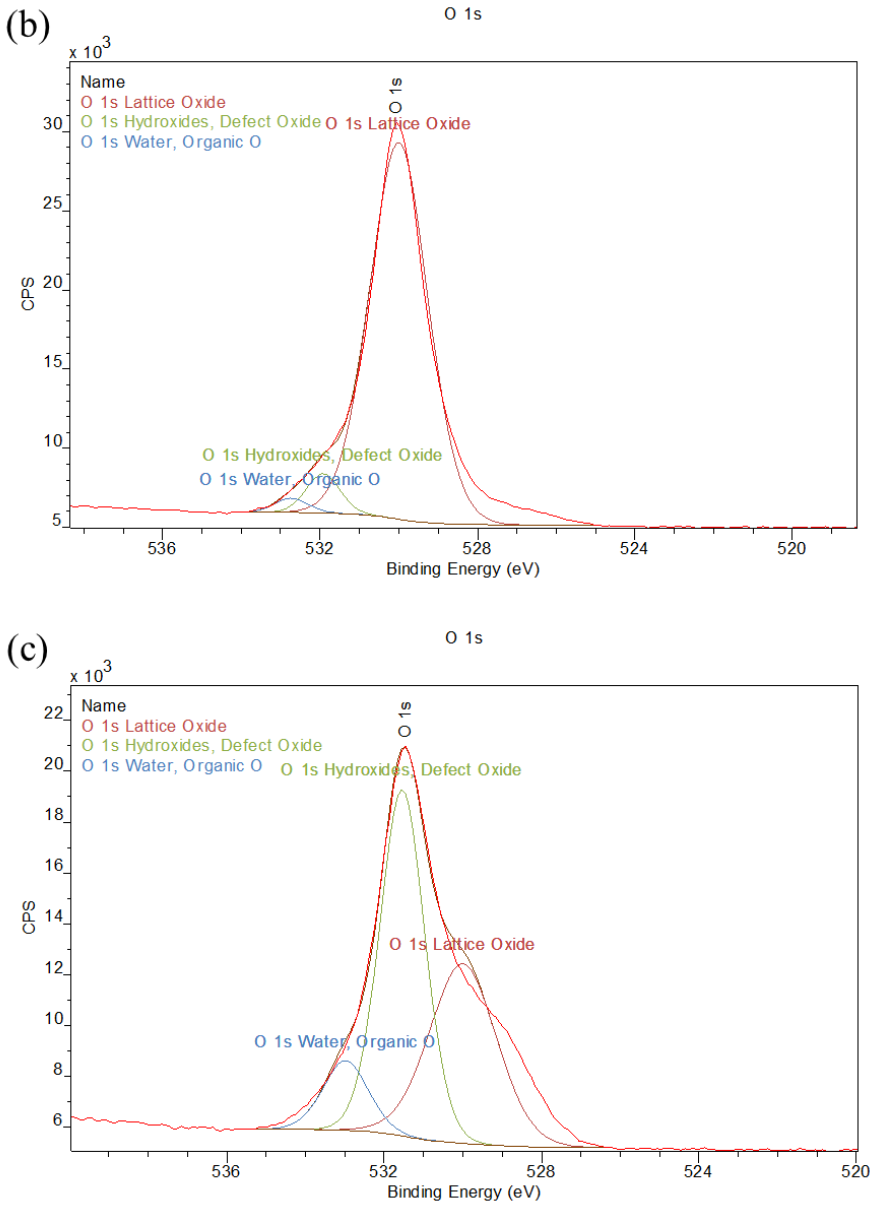

Figure 4-10 High resolution XPS spectra of O 1s region for laser treated Ti samples at line spacing of 4.8 μm that were stored (a) in air for 4 weeks (b) in air for 7 days, and (c) in ethanol for 1 day.

Table 4-6 Percentage of functional groups in O 1s region for Ti surfaces.

Functional groups/At%	Surface patterns and storage conditions							
	Air 4w		Air 7d			Ethanol 1d		
	4.8	G	4.8	G	P	4.8	G	P
Lattice O	91.17	90.80	92.38	90.17	87.36	39.15	30.34	88.65
Hydroxides (-OH)	6.10	6.84	5.59	6.85	9.17	50.66	33.66	7.84
O-C=O	2.73	2.35	2.03	2.99	3.46	10.19	36.00	3.51

4.2.5 Discussion

In terms of surface chemical composition, the XPS analysis indicated the presence of an oxide layer mainly consisting of TiO_2 for cp Ti, which was independent of the laser treatment and surface structure. In addition, minor amounts of sub-oxide, Ti_2O_3 and TiO, or even metallic Ti were observed for cp Ti before and after laser treatment. Oxides existed on the Ti surface since it is a highly reactive metal that can react with oxygen within a few seconds of being exposed to air [110]. Laser treatment in ambient environment can cause further oxidation of the titanium surface. Compared with the polished surface, laser treatment induced a small amount of Ti^{3+} and Ti^{2+}, which transformed to the most thermodynamically stable state, Ti^{4+}, during exposure to air. However, such transition of titanium valence states was slowed down by storing in ethanol, which isolated the laser machined area from the air. The laser induced oxidation may be due to the high temperature reached on the titanium surface during laser processing [111]. The presence of a titanium oxide layer would lead to better biocompatibility and higher corrosion resistance due to its low electrical conductivity and thermodynamic stability at physiological pH values [112].

It has been demonstrated that the carbon composition plays a key role on the surface wettability of laser treated metallic surfaces. Most carbon came from the accumulation during laser processing, which was carried out in air. For the samples under air storage, some of the carbon came from the absorption and decomposition of CO_2 from the air, while for samples stored in ethanol, the carbon contamination was due to the absorption and reaction of C_2H_5OH on the titanium surface [93][94]. A nanostructure with higher surface energy is created on the surface by laser texturing, which can increase the surface adsorption activities and may help to capture airborne hydrocarbons [114]. Although the relative C-C/H concentration on laser treated surfaces was lower compared to the polished surfaces, the presence of CH_3 groups was also responsible for the hydrophobicity of laser treated titanium surfaces. Moreover, femtosecond lasers have been shown to allow for the photo-dissociative ionization of the covalent bonds C-C and C-O, which increases the possibility of chemical reaction between Ti- and -C to form C-Ti bonds as observed here [108].

Another factor affecting surface chemistry is the storage environment. Although the

samples were stored in different storage media, they were not stored away from light. It has been shown that ultraviolet (UV) irradiation can induce photocatalytic oxidation and consequently a more hydrophilic TiO_2 [115]. One of these oxidation mechanisms suggests that the TiO_2 hydrophilicity is caused by structural changes at the surface. It has been reported that the UV irradiation can induce charge carriers (holes or electrons) that can react with lattice oxygen of metal oxides to create oxygen vacancies, which result in the absorption of water molecules or bonding with hydroxyl groups on the surface [95][96]. Other research demonstrated that Ti_2O_3/TiO_2 heterophase junctions displayed high photocatalytic activity of CO_2 reduction to yield CH_4, CO and O_2, where metallic Ti_2O_3 served as a reduction site to produce solar fuel, such as CO and CH_4, and TiO_2 served as an oxidation site to produce O_2 and protons with H_2O [117]. This is another possible explanation for why $-CH_3$ functional groups appeared on the surfaces after several days of exposure to air. Furthermore, the photooxidation of ethanol absorbed on anatase TiO_2 surfaces produces acetaldehyde (C=O) in the presence of O_2 [116]. Therefore, the formation and change in the oxide layer were guided by a variety of mechanisms, and the relative composition of elements fluctuated slightly.

4.2.6 Summary

The main conclusions of this part are summarized as follows:

1. Laser treatment led to further oxidation of cp Ti surfaces, which produced less metallic Ti and more titanium oxides and sub-oxides.
2. Relative carbon content for laser treated Ti increased over time when exposed to an ambient environment, which was mainly due to the formation of new functional groups and even reaction between Ti- and -C.
3. Sub-oxides of titanium were able to transform to the more thermodynamically stable state, TiO_2; however, this transition was slowed down by immersing the samples in ethanol.
4. Photocatalytic activity of TiO_2 was one mechanism for the observed changes in surface composition.

4.3 Surface Wettability

In this section, the effects of exposure time, surface morphology, and storing environment

on the wetting behavior of textured titanium surfaces is described, and the repeatability of surface wetting behavior is discussed.

4.3.1 Effect of storage time and groove spacing on wettability

Contact angle measurements were carried out on laser textured cp Ti samples as well as polished samples when stored in air for a period of time. The specific time points were from 0 day to 4 weeks. The contact angle of freshly laser textured surfaces and ultrasonically cleaned laser textured surfaces was measured and compared as well. The effect of storage time and surface structure on surface wettability is discussed first.

Figure 4-11 (a) shows a drop that had been deposited on a laser textured cp Ti surface right after machining. The drop spreads a lot on the sample surface and the measured contact angle is very low, approximate 5 degrees, which means that the laser treated surface is superhydrophilic. After ultrasonic cleaning in ethanol, the contact angle increased slightly and reached about 30 degrees as shown in Figure 4-11(b). This is because a layer of air is trapped into the microstructure and the debris. After ultrasonic cleaning in ethanol, some ethanol may remain inside the microstructure and nanostructure, which limits the spread of the droplet on the surface, so the contact angle increases slightly, but the surface is still hydrophilic.

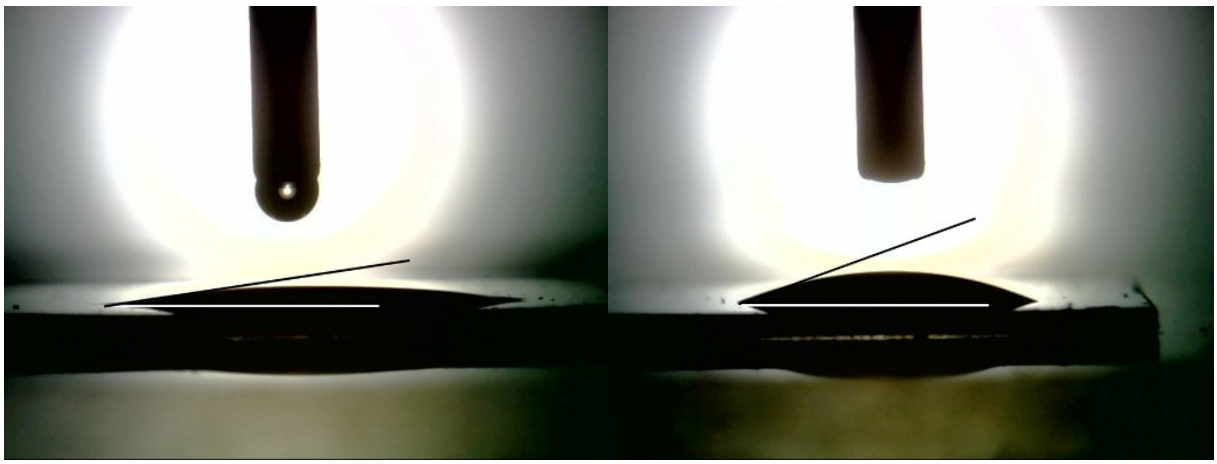

Figure 4-11 Images of contact angle measurement for cp Ti samples (a) right after laser machining and before ultrasonic cleaning, and (b) after laser machining and ultrasonic cleaning

Figures 4-12 and 4-13 show a clear increase of the contact angle over time when the samples are stored in air for up to a month. Overall, the contact angle increase was more significant in the first three to five days, while for narrower line spacing, the contact angle

increased significantly after only one day. For example, the change in contact angle was about 30° for grooves with line spacings of 10 μm, but for those with 1.2 μm line spacings, the change was more than 100°. When the laser treated samples were measured right after laser machining, the values of contact angle were about 35° for polished samples and laser grooved samples at line spacings of 10 μm and 4.8 μm, while for samples at line spacings of 2.4 μm and 1.2 μm, and for gradients, the contact angle started from about 20°. The effect of line spacing on contact angle was less obvious since the contact angle for samples at line spacings of 2.4 μm was lower than that of 4.8 μm in the first 5 days. After five to seven days, the increase in contact angle slowed down and plateaued. After 4 weeks, the contact angle of surfaces with line spacings of 10 um and 4.8 um reached about 123° and 126° respectively. Narrower line spacings appeared to lead to higher maximum contact angle values. The contact angle plateaued with 1.2 μm spaced grooves after reaching values higher than 135°. As for the surface covered with gradients, the contact angle increased to 135°, while that of the polished sample was closer to 100°. The presence of grooves accelerated the evolution of the contact angle to a higher value compared with polished surfaces, and the narrower the line spacing was, the higher values the contact angle could reach.

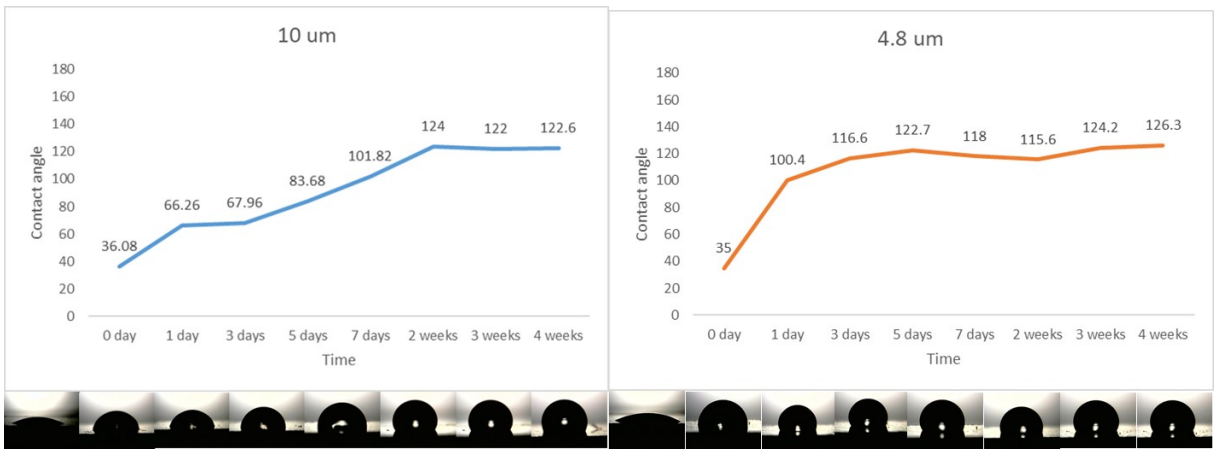

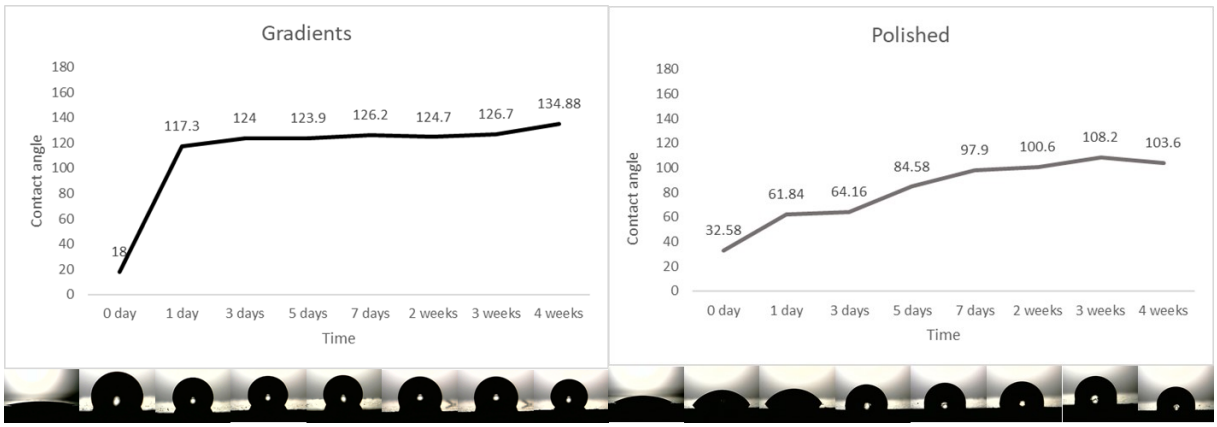

Figure 4-12 The evolution of contact angle over time for different surface patterns, (a) 10 μm, (b) Polished, (c) 4.8 μm, (d) gradients.

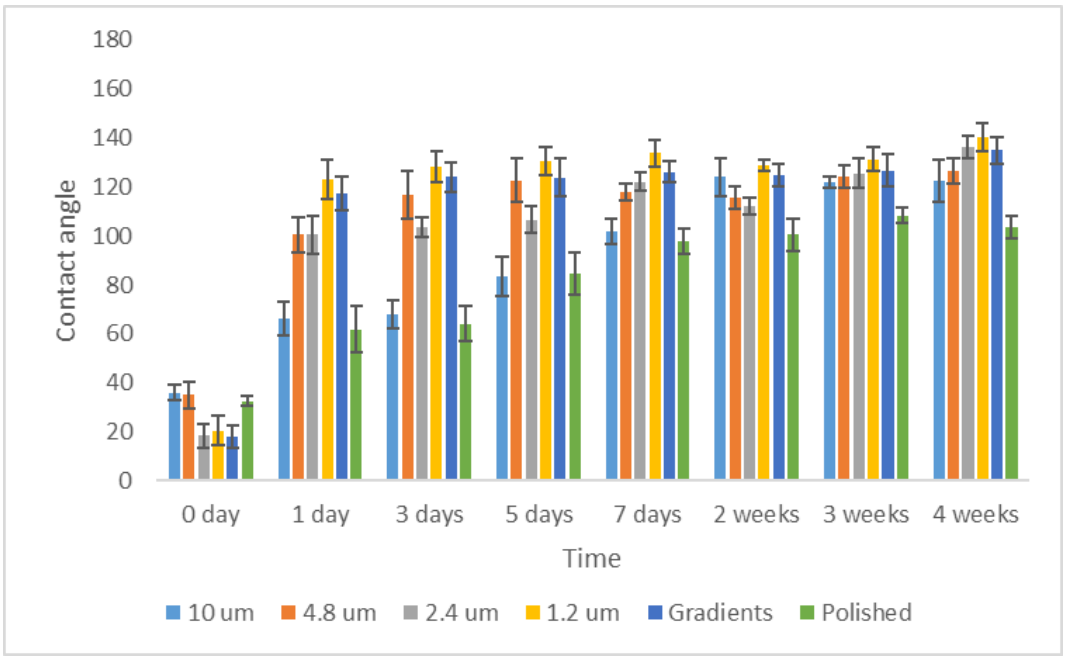

Figure 4-13 The bar chart for comparing the evolution of contact angle over time for polished samples and laser texture Ti samples at different line spacing. (Dark blue bar – 10 μm, Red bar – 4.8 μm, Green bar – 2.4 μm, Purple bar – 1.2 μm, Light blue – gradients, Orange bar – polished)

Another phenomenon caused by the presence of grooves is anisotropy of the wetting behavior. In the experiments, the laser treated cp Ti samples were observed from two directions, one was parallel to the direction of the grooves, and the other was perpendicular to the direction of the grooves as shown in Figure 4-14. When the observation direction was parallel to the groove direction, the drop was rounder, which led to a higher contact angle of over 100°. When the contact angle was observed perpendicular to the groove direction, the

droplet was more like a semicircle on the laser treated surface, where the contact angle was lower than 90°. The anisotropy of grooves on the surface caused an anisotropy of wettability.

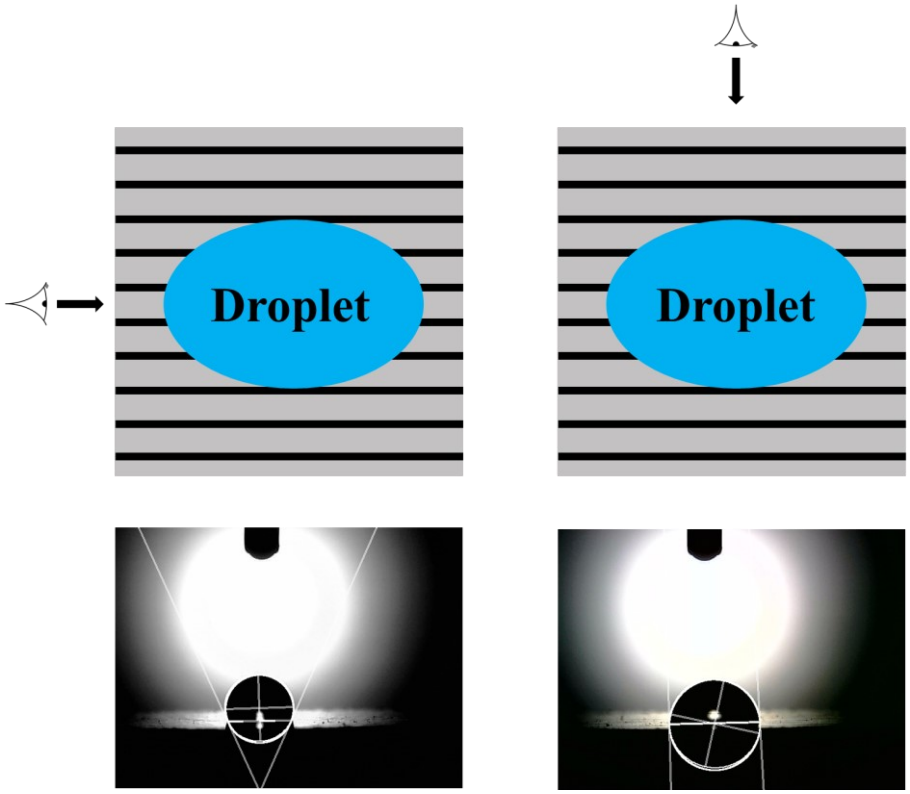

Figure 4-14 Schematic of two observation directions for contact angle measurement in Ti samples

Also, it was observed that the narrower line spacings led to a more anisotropic wetting behavior on laser treated cp Ti surfaces even when the surfaces were hydrophobic, as shown in Figure 4-15.

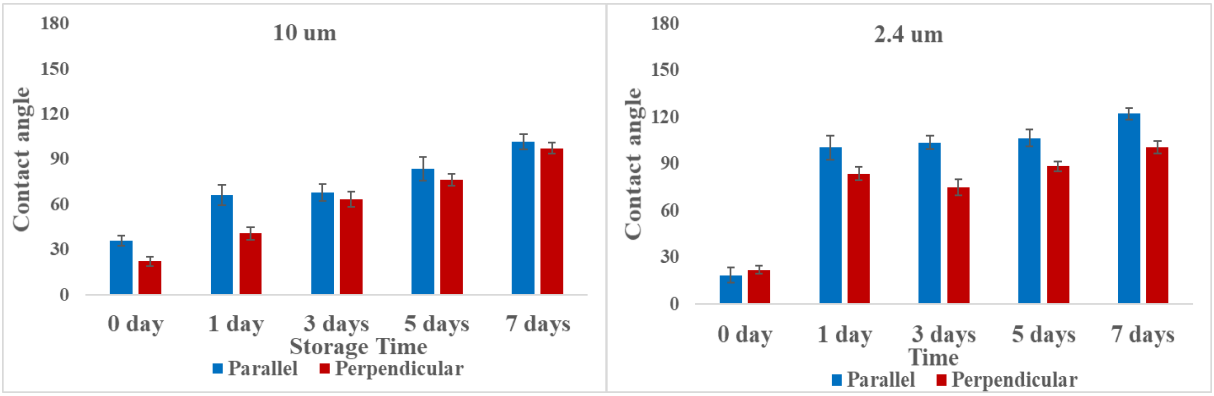

Figure 4-15 The evolution of contact angle observed from two directions on cp pure Ti samples at line spacing of (a)10 μm and (b) 2.4 μm from day 0 to day 7 (Dark blue bar – viewing direction is parallel to groove direction, Red bar – viewing direction is perpendicular to groove direction)

Overall, surfaces exhibited time-dependent wetting behavior with an increase in contact

angle with increased storage time. The evolution of contact angle was affected by the groove spacing, and anisotropy in surface patterns (groove orientation) led to anisotropy in wetting behavior. Moreover, when the line spacing was narrower, the anisotropy was more prominent.

4.3.2 Effect of storage environments and time on wettability

Different storage conditions had a significant impact on surface wettability. Laser treated cp Ti samples at line spacing of 10 μm were stored in air, ethanol and rough vacuum for a period of time, and the measured results are presented in Figure 4-16. As described above, the contact angle increased from about 35° to over 120° after a 4-week exposure to air. The samples stored in rough vacuum also showed a clear increase in contact angle over time, and the contact angle was even higher than the samples stored in air in the first five days. Such difference was reasonable since the change of contact angle was random in early period (less than 7 days), and the samples were tested in ambient environment, which may have led to contamination on Ti surfaces. The surface was hydrophobic whether stored in air or rough vacuum. For samples left in ethanol, the contact angle ranged from 40° to 50°, which means the surfaces were hydrophilic. Storage in ethanol can slow down the evolution to a hydrophobic state.

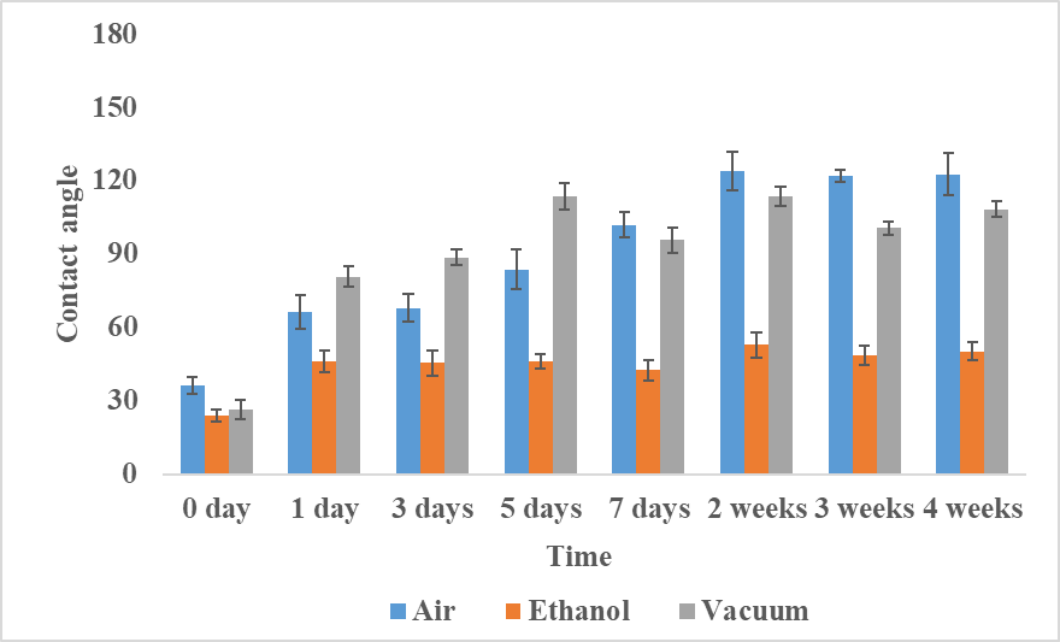

Figure 4-16 Time-dependent evolution of contact angle when cp pure Ti samples at line spacing of 10 μm stored in air (Blue bar), ethanol (Orange bar) and vacuum (Grey bar)

To sum up, the storage conditions are of vital importance to the surface wetting states. Hydrophilic surfaces can be obtained and maintained over long periods of time when stored in ethanol. The suitable storage environment can be selected according to different requirements.

4.3.3 Discussion

4.3.3.1 Surface topography

The existence of grooves hindered the spread of droplets on surfaces, especially in the direction perpendicular to the groove orientation, which resulted in contact angle anisotropy. This phenomenon can be explained by the fact that periodic grooves create an energy barrier to the movement of the three-phase contact line that is perpendicular to the groove orientation, and promote the movement in the direction of the grooves. As a result, the droplet elongated in the direction of the groove, because there was no contact line movement obstacle that caused pinning in this direction. It was also observed that the higher surface roughness obtained for the narrowest line spacing, accelerated both the evolution of surface wettability over time and the anisotropy of the wetting behavior.

Laser treatment enhanced the wettability of the surfaces right after laser texturing, as shown by the very low contact angle observed on laser treated surfaces with high surface roughness. The wetting behavior can be explained by the Cassie-Baxter model, as shown in Figure 2-14(c), where rough surfaces can be treated as two distinct components; the substrate and trapped air in nanostructure, which should lead to higher contact angles [1]. This phenomenon can be explained by capillary action, which drives the liquid into valleys between ridges and expels the trapped air when the liquid penetrates the surface.

4.3.3.2 Surface chemistry

According to the literature, the main component of the oxide layer on Ti surfaces is TiO_2, which is hydrophilic. Therefore, laser induced titanium oxides contributed to enhancing the hydrophilicity of surfaces. However, laser treatment also accelerated the contamination of carbon from the air during laser processing and storage, which led to more hydrophobic surfaces, where the functional groups that contribute to hydrophobic property are C-C/H, $-CH_3$ and C-Ti [109]. Unlike the ambient environment, limited carbon contaminations from

storage in ethanol helped retain a hydrophilic surface over time and the absorption of C-O-C and C=O bonds further contributed to the observed hydrophilic behavior, although surface oxidation which also promoted hydrophilicity was slowed down. Combining the analysis on surface chemistry and wettability, the laser treated Ti surfaces covered with gradients was more hydrophobic than the surfaces with grooves at line spacing of 4.8 μm and polished surfaces due to the higher concentration of C-C/H and -CH_3 bonds as well as the formation of C-Ti bond.

Due to the titanium oxidation by the formation of TiO_2, which promotes hydrophilicity, and the continuous accumulation of carbon, which promotes hydrophobicity, the surface wettability was difficult to predict. The fluctuations in contact angle were therefore due to several competing phenomena over time.

4.3.4 Summary

The main results introduced in this section are summarized as follows:

1. The surface wettability of laser textured surfaces was time dependent. The wetting state was transformed from hydrophilic to hydrophobic.
2. By controlling the laser process parameters, such as line spacing, specific wetting performance was realized. The depth of grooves had little effect on the contact angle while the line spacing was closely related to contact angle, where a decrease in groove spacing resulted in an increase in contact angle.
3. The anisotropy of surface topography (i.e. groove orientation) resulted in anisotropy in the spread of the droplet, especially when the surface coverage induced by laser texturing was high.
4. Storage conditions affected the surface wetting behavior, where samples remained in a hydrophilic state for a long period when stored in liquid, and the surfaces reached a superhydrophobic state after being exposed to air for several days.
5. The surface wettability was difficult to predict, especially for short time periods due to several competing phenomena over time (oxidation and carbon contamination).

4.4 MG 63s osteoblast-like cell responses to laser textured Ti surfaces

In this section, the cell response, including cell morphology and adhesion, cell number and cell area coverage are discussed. The results of cell behavior to laser-induced surfaces are from a collective effect of surface topography, surface chemistry and surface wettability. The cell diffusion and adhesion at early stages are important because they are considered the main determinants of long-term bone-implants interface response, which is related to the subsequent spread and growth of osteoblasts on the implant surface [118].

4.4.1 Stored in 99% ethanol for 1 day

In the experiments for biocompatibility of laser-textured titanium surfaces, all surface patterns were tested, which are uniform grooves with line spacings of 10 μm, 4.8 μm, 2.4 μm, 1.2 μm, gradients and polished surface as control. These Ti samples were stored at room temperature in 99% ethanol for 1 day before cell culture. The timepoints for cell incubation were 1 day, 3 days and 7 days.

4.4.1.1 Cell morphology, adhesion and spreading

Fluorescence images of all types of line spacing at three timepoints of cell culture are shown in Figure 4-17 at lower (10x) and higher (20x) magnifications. It could be observed that with increasing incubation time, the cell coverage and size was increased. After 1 day of culture, a few cells attached on the surface, part of them were connected with each other (see Figure 4-17, 1 day, 10x). When the incubation time increased to 3 days, the F-actin fibers spread on the entire surface, and the size of cell nuclei tended to be about 10% larger (see Figure 4-17, 3 days, 10x). When the Ti samples were cultured for 7 days, more cell growth and proliferation was observed, and some areas of the surface were covered with a thicker layer of F-actin fibers (see Figure 4-17, 7 days, 10x). Due to the growth and proliferation of cells, the cell number and the thickness of cell layers increased as well.

When the cell morphology was compared among all line spacings, no significant differences were observed. The spread of F-actin fibers was somewhat preferentially aligned

along the direction of grooves (see Figure 4-17, 1 day, 10x). There were more single cells attached on the laser treated Ti surfaces after 1 day of cell culture. For example, for the surfaces covered with grooves with a line spacing of 10 μm, the shape of cells was more slender, and they tended to align along grooves (see Figure 4-17, 10 μm, 1 day, 10x). However, when the line spacing was decreased to 1.2 μm, the effect of groove direction was reduced, where the F-actin fibers of a few cells spread perpendicular to groove direction (see Figure 4-17, 1.2 μm, 1 day, 10x). After 3 days and 7 days of incubation, the performance of cells was almost the same for all laser treated surfaces, the cells still spread parallel to the groove orientation, while the cells had no preferential orientation on polished Ti surfaces (see Figure 4-17, 3 days, 10x and 7 days 10x).

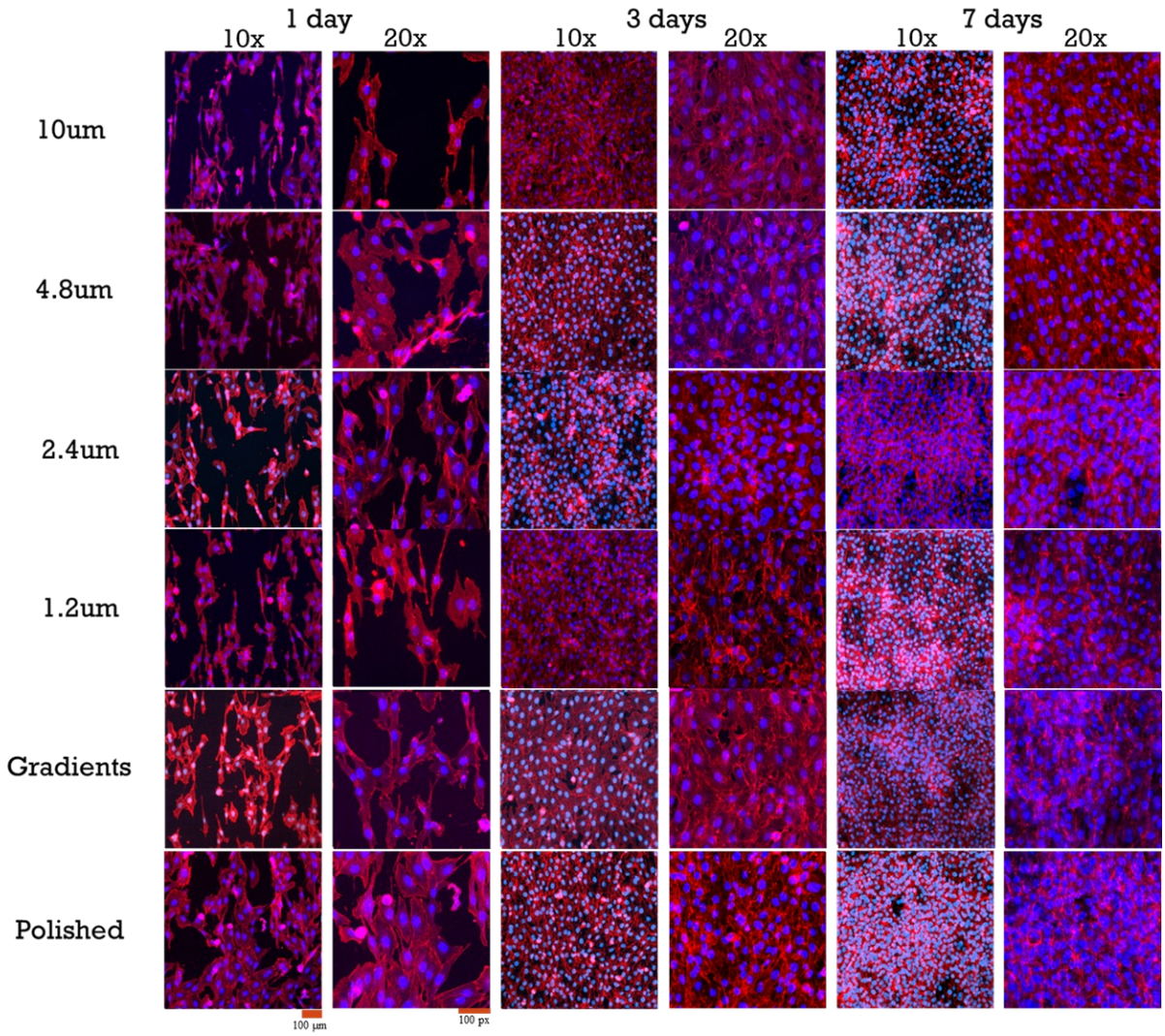

Figure 4-17 Fluorescence images at lower magnification of 10x and higher magnification of 20x of cp pure Ti samples at all types of line spacing with controlled samples that were stored in ethanol for 1 day, and the incubation time is 1 day, 3 days and 7 days.

Focusing on the images of higher magnification at 20x, more details are acquired on the effect of surface patterns on cell morphology. At 20x magnification, the direction of grooves was obvious, which was parallel to the vertical axis. In order to better visualize the image in Figure 4-17, a few samples were selected for which the images were magnified, regular groove spacing at 4.8 µm, gradient as well as polished surfaces. When the incubation time was 1 day (Figure 4-18), a few cells remained attached to the sample surface. For the surfaces with grooves, cells spread along the direction of grooves in an elongated shape. The randomness of cell orientation between grooves was positively related to the line spacing. In this experiment, samples were prepared with groove widths of 1 µm which was much smaller

than the size of the cells, which avoided cells depositing at the bottom of grooves. The distance of the spread of actin fibers was limited, so there were more empty areas without cells and more single cells. In addition, the shape of cell nuclei was somewhat elongated, and there were more small cells.

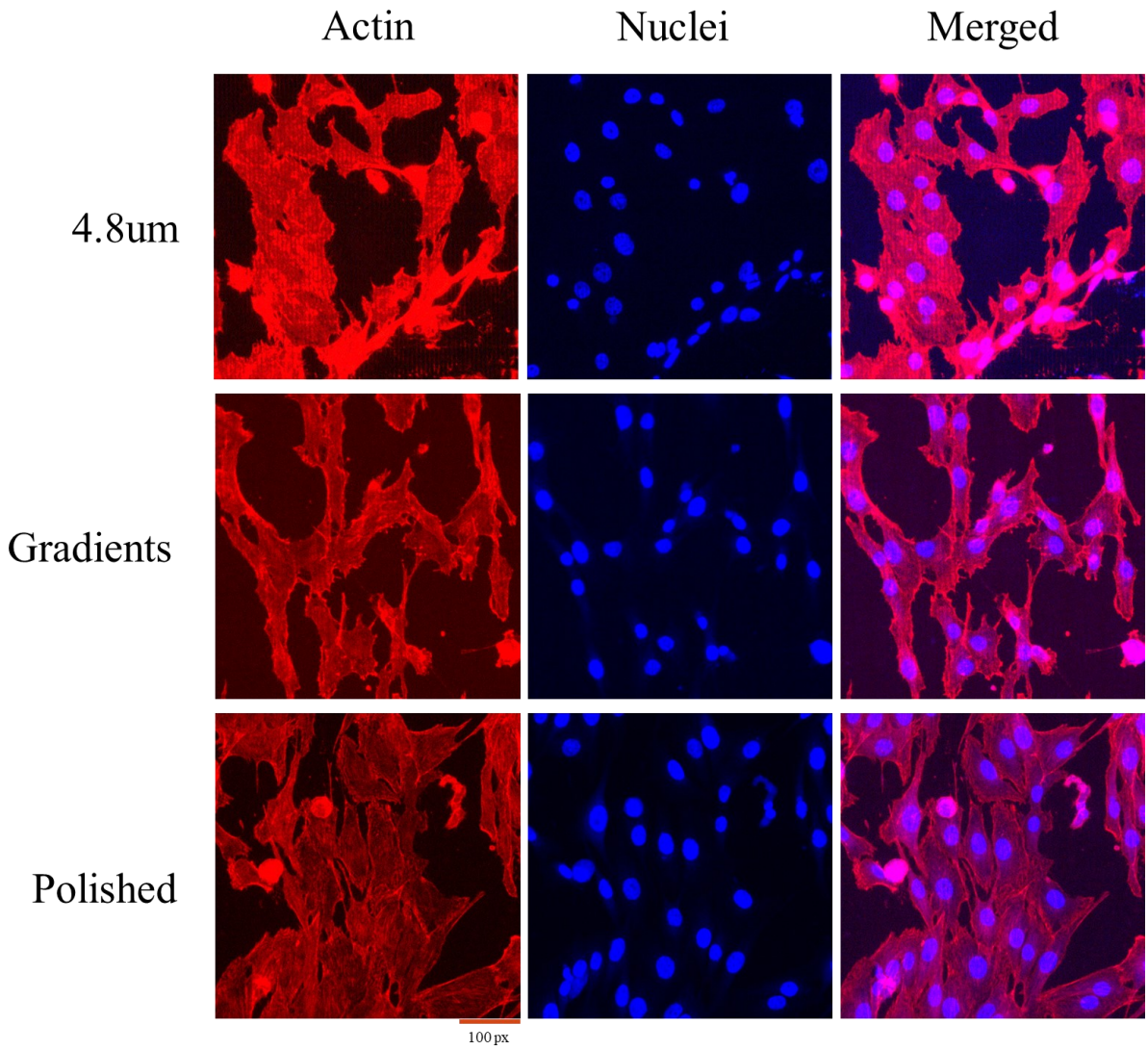

Figure 4-18 Fluorescence images of cp pure Ti samples with uniform grooves at line spacing of 4.8um and gradients and polished surfaces after 1 day of culture at 20 x. (Red – Actin, Blue – Nuclei, RGB – Merged)

Almost all cells aggregated together to form a cell membrane on the Ti surfaces after 3 days of culture as shown in Figure 4-19, although there were some little holes remaining in the membrane. At this moment, the shape of a single cell could not be recognized, however, the spread of F-actin fibers still followed the groove orientation on laser textured surfaces. There were more large cell nuclei, and the shape of the cell nuclei was more circular after long

incubation time compared to that after a shorter incubation time.

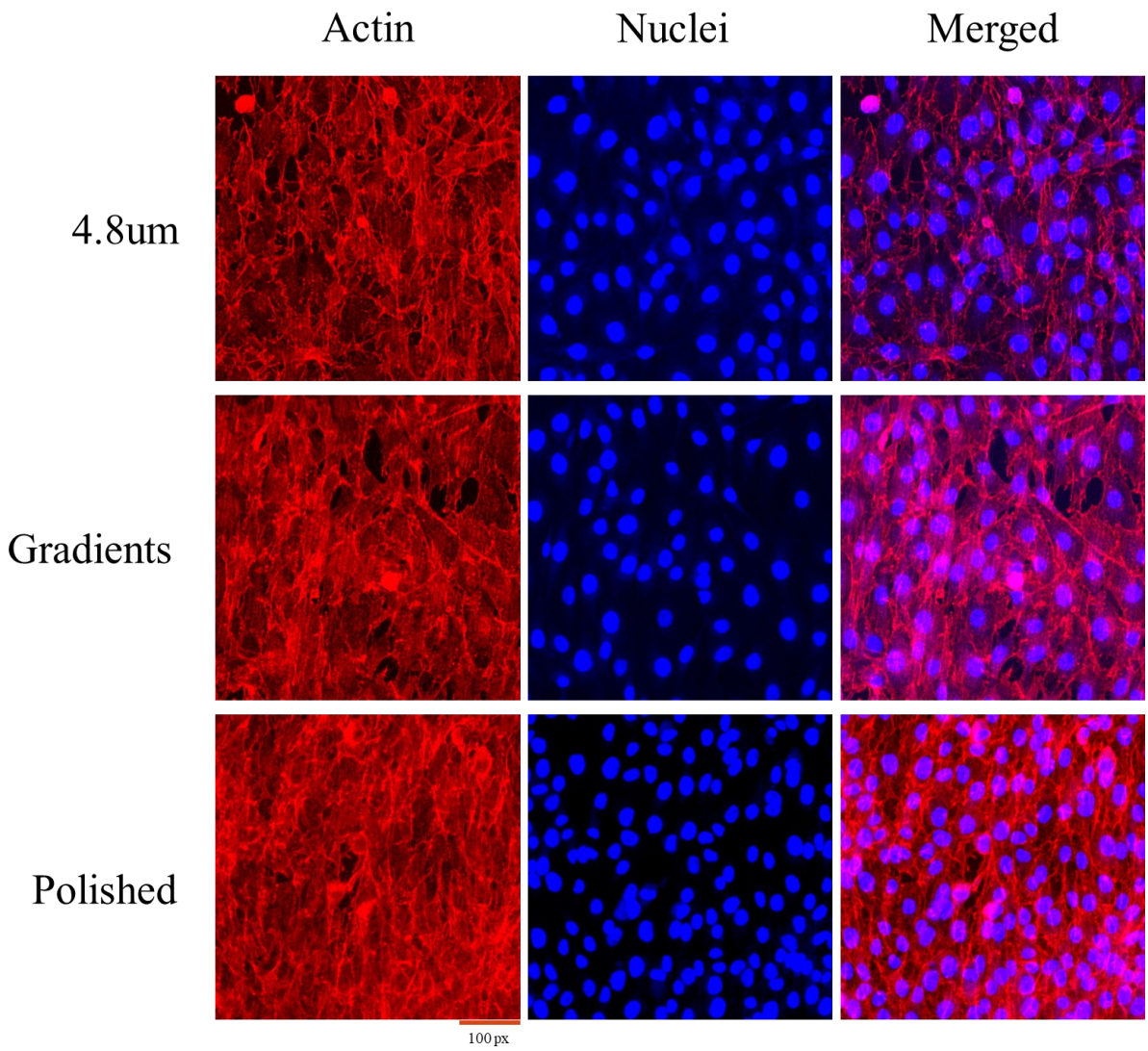

Figure 4-19 Fluorescence images of cp pure Ti samples with uniform grooves at line spacing of 4.8um and gradients and polished surfaces after 3 days of culture at 20 x. (Red – Actin, Blue – Nuclei, RGB – Merged)

The entire surface was covered in cells, and an integral cell layer was formed after the 7-day incubation, which is presented in Figure 4-20. From the nuclei-DAPI images, many cell nuclei appeared to touch each other resulting in a thicker cell layer. Note that even though a thicker cell layer was formed, the grooves were still visible on the images, and the spread of the F-actin fibers still followed the groove orientation. The shape of cell nuclei was almost round, meaning that it was no longer affected by the presence of the grooves.

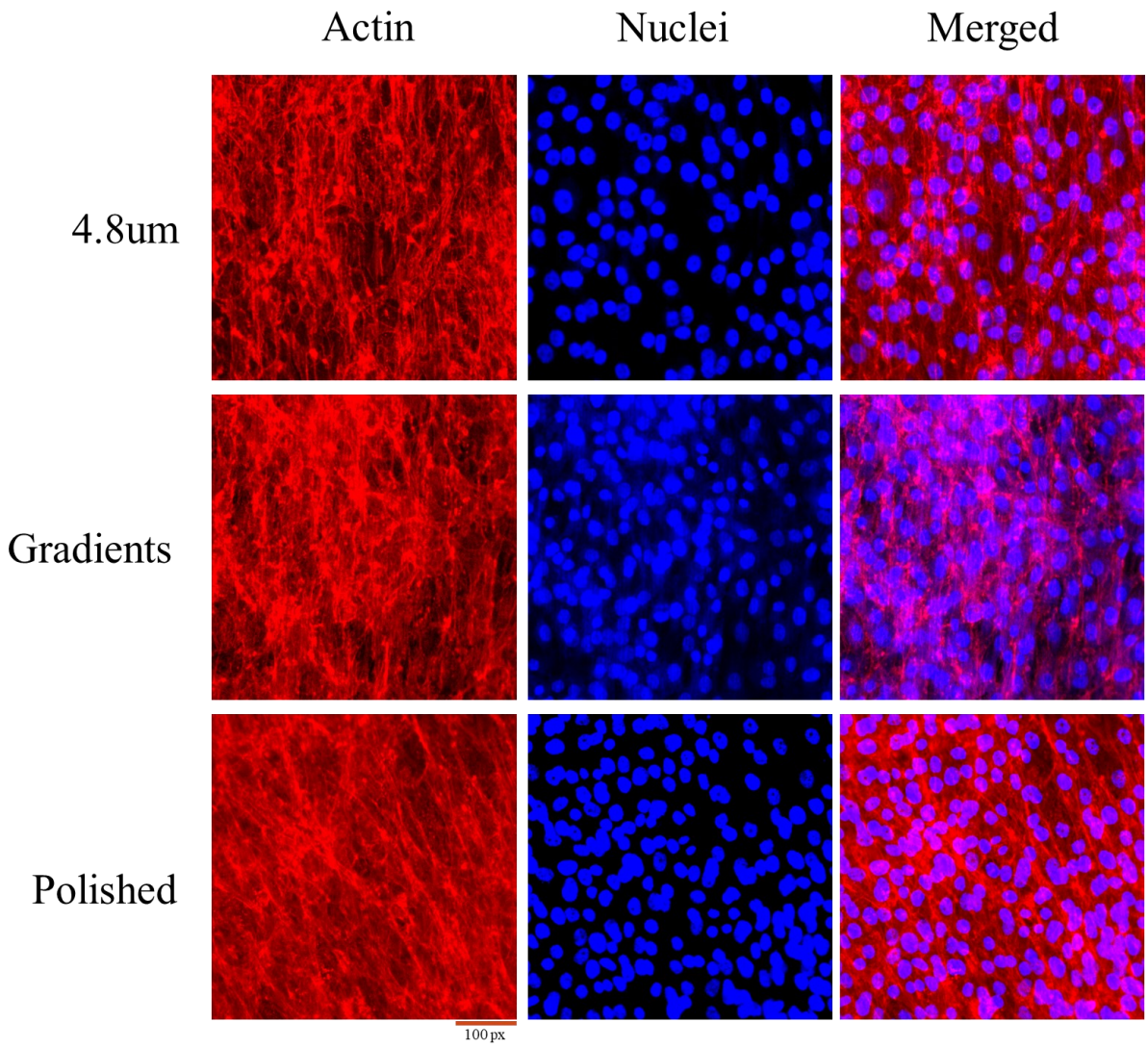

Figure 4-20 Fluorescence images at 20x magnification of cp pure Ti samples with uniform grooves at line spacing of 4.8um and gradients and polished surfaces after 7 days of culture (Red – Actin, Blue – Nuclei, RGB – Merged)

4.4.1.2 Cell number and area coverage

To quantify the amount of cells on the sample surface after incubation, both the number of cells and the area fraction of cells was extracted from the fluorescence microscope images Figure 4-21. The quantity of cells ballooned from 1 day to 3 days of incubation, where the cell number at 3 days was two to three times higher than that at 1 day. In particular, cell numbers for samples at a line spacing of 2.4 μm increased significantly from 1 day to 3 days of incubation. The change was more than 270%, while the change in cell number for samples covered with gradients was lowest at about 210%. The cell number was then observed to rise

slightly or to even decrease from 3 days to 7 days due to the accumulation and agglomeration of cell nuclei resulting in counting errors. To mitigate these counting errors, an analysis based on the area fraction of cell nuclei was used to demonstrate cell proliferation. Figure 4-21(b) shows the percentage of cell nuclei area, where from 3 days to 7 days, a dramatic increase was observed. Indeed, the 2.4 µm spaced grooves showed a cell number decrease from almost 400 to about 310, while the cell area increased from 25% up to 45%. This proved that cells keep proliferating on the surface even after a layer of cells had covered the entire surface. The error bars for the same group of samples under the same condition were introduced to analyze the scatter in collected data presented in all bar charts.

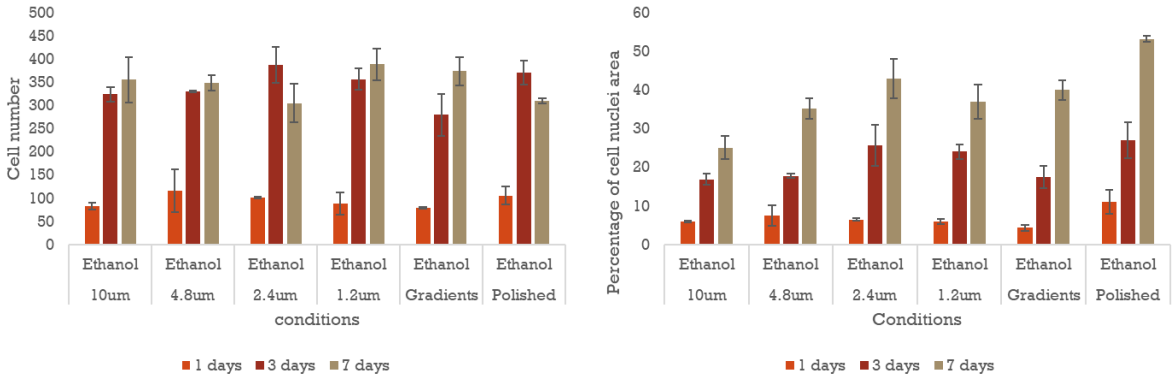

Figure 4-21 (a) Counting on cell number and (b) percentage of cell nuclei area of laser-grooved cp pure Ti samples with uniform grooves of all kinds of line spacing and gradients and polished cp pure Ti samples that were stored in ethanol for 1 day after 1, 3 and 7 days of cell culture.

4.4.2 Stored in air for 7 days

While in the previous section, samples were stored in ethanol and thus had a hydrophilic surface, in this section, the response of MG 63s cells to hydrophobic surfaces was investigated. Laser treated Ti samples as well as control samples were stored in air at room temperature for 7 days before cell culture. The cell adhesion and spreading were analyzed by fluorescence microscopy, and the cell proliferation was assessed based on the number and area of cell nuclei.

4.4.2.1 Cell morphology, adhesion and spreading

All fluorescence images of cells on polished and laser-textured Ti samples that were stored in air for 7 days are presented in Figure 4-22. The performance of cells, such as the spread

and shape of cells and the formation of cell membrane, was similar to the results for the samples stored in ethanol for 1 day.

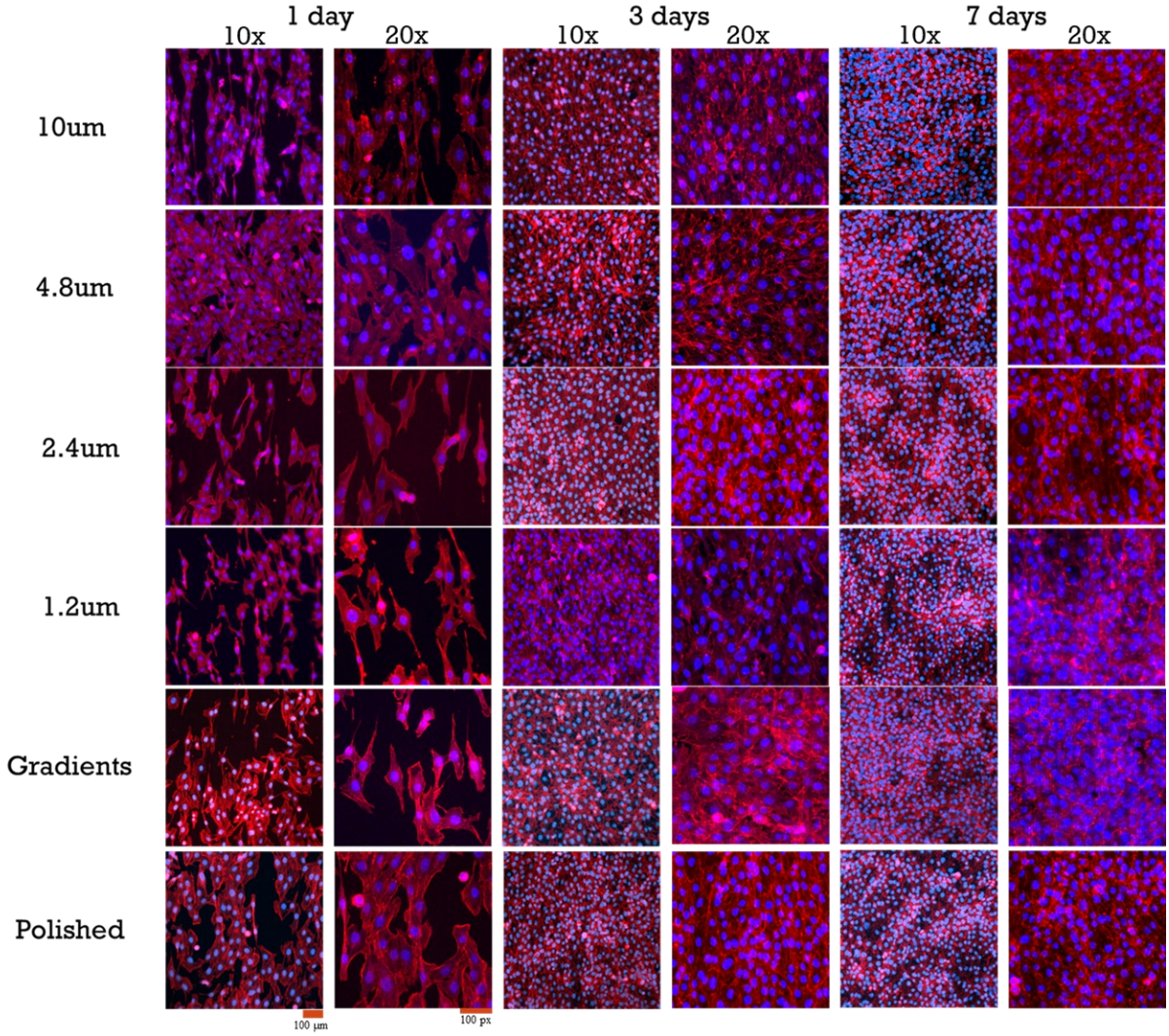

Figure 4-22 Fluorescence images at lower magnification of 10x and higher magnification of 20x of cp pure Ti samples at all types of line spacing with controlled samples that were stored in air for 7 days, and the incubation time is 1 day, 3 days and 7 days.

The grooves that were covered with a layer of cells are visible at 20x magnification. Not only did the F-actin fibers spread along the groove orientation, but the shape of cell nuclei was also elliptical along the direction of the grooves. The F-actin fibers of each cell started spreading and connecting with other cells. Compared with polished surfaces, the connection between cells was limited by the presence of the grooves.

After 3 days of cell culture, the difference between each condition was reduced. Due to the growth and proliferation of cells, a cell membrane formed on the surfaces. F-actin fibers

spread and covered the entire surface, and the cell nuclei tended to aggregate. As for the samples stored in ethanol, even though F-actin fiber filaments were intertwined and distributed all over the sample surface, the overall shape of the cell was still along the direction of the grooves (while the cells on the polished surface did not have a preferential growth direction). The shape of the nuclei was more circular after 3 days of cell culture than that after shorter incubation times, especially those of smaller size. As for the timepoint of 7 days, there was little difference between different conditions. The growth and proliferation of cells were not limited to the two-dimensional surface, they had the tendency to grow above the surface with increasing thickness of the cell layer. The F-actin layer where nuclei accumulated was found to be thicker than in other areas according to the change of red shade in the images.

4.4.2.2 Cell Number and area coverage

The number of cells as well as the area percentage of cell nuclei are presented in Figure 4-23. After 7 days, the number of cells was decreased since more cells proliferated and aggregated, which caused counting errors. The cell area however showed a continuous increase in the area fraction of cells with incubation time. The performance of cells at a line spacing of 2.4 μm was the best among all conditions, whether in air or in ethanol.

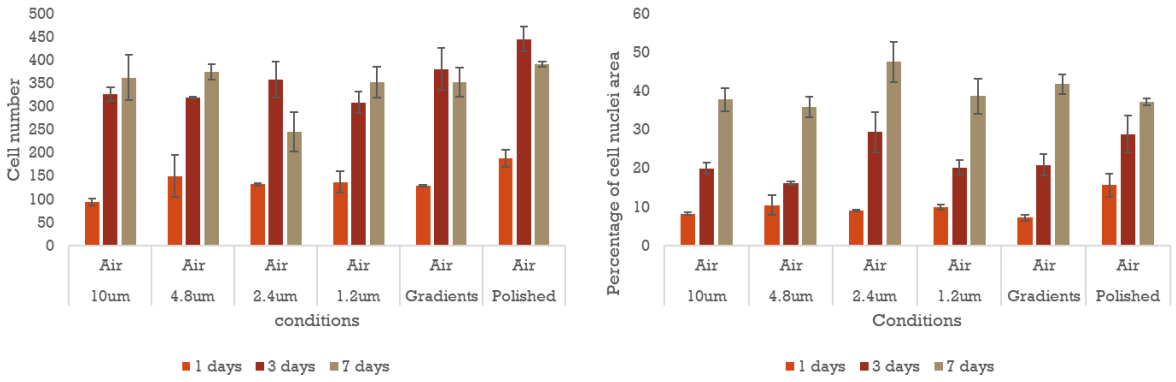

Figure 4-23 (a) Counting on cell number (b) percentage of cell nuclei area of laser-grooved cp pure Ti samples with uniform grooves of all kinds of line spacing and gradients and polished cp pure Ti samples that were stored in air for 7 days after 1, 3 and 7 days of cell culture.

4.4.3 Stored in air for 10 days

In order to investigate the effect of long storage times after laser texturing on cell behavior

three surface patterns, namely line spacings of 4.8 μm and 2.4 μm, and gradients, were chosen. The samples were left in ambient air for 10 days, and the time points for cell culture were 1 day and 3 days.

4.4.3.1 Cell morphology, adhesion and spreading

In these experiments, the Ti samples with surface patterns of gradients and uniform grooves with line spacings of 4.8 μm and 2.4 μm were tested. Samples were stored in air for 10 days before the cell culture. Fluorescence images of these samples are presented in Figure 4-24. According to these images, it was shown that the shape of cells and the spread of cells were affected by the orientation of the grooves. However, the performance of cells was not as good as that of the previous group. First of all, the size of each cell was much smaller, and more cells were independently distributed on the surface. Secondly, after 3-day incubation, the cells could not spread on the entire surface, and there were still some cells at small size.

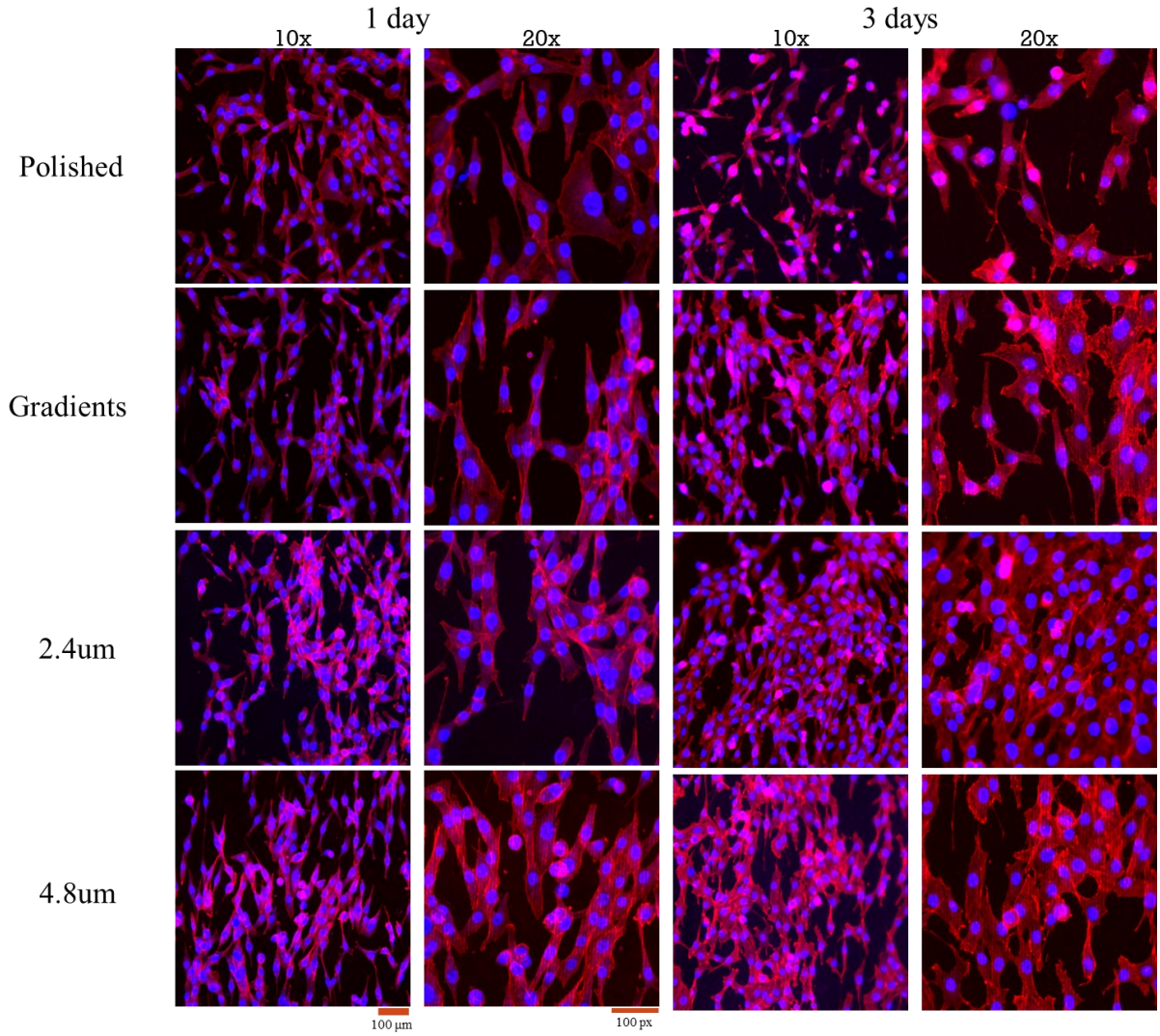

Figure 4-24 Fluorescence images at lower magnification of 10x and higher magnification of 20x of cp pure Ti samples at line spacing of 4.8 µm, 2.4 µm and gradients with controlled samples that were stored in air for 10 days, and the incubation time is 1 day and 3 days.

4.4.3.2 Cell number and area coverage

When it comes to the cell number and area percentage of cell nuclei (see Figure 4-25), they are not as high as those shown in Figure 4-23 but similar to those shown in Figure 4-21. In Figure 4-25 (a), although the cell numbers under every condition increased up to 100 from 1 day to 3 days, the number and area of cells were much smaller than for samples stored in air for 7 days. And unlike the results in Figure 4-21, the laser textured surfaces performed better than polished surfaces at more hydrophobic states. The standard deviation of 3 days of data was the largest, which means the randomness of cell behavior was increased.

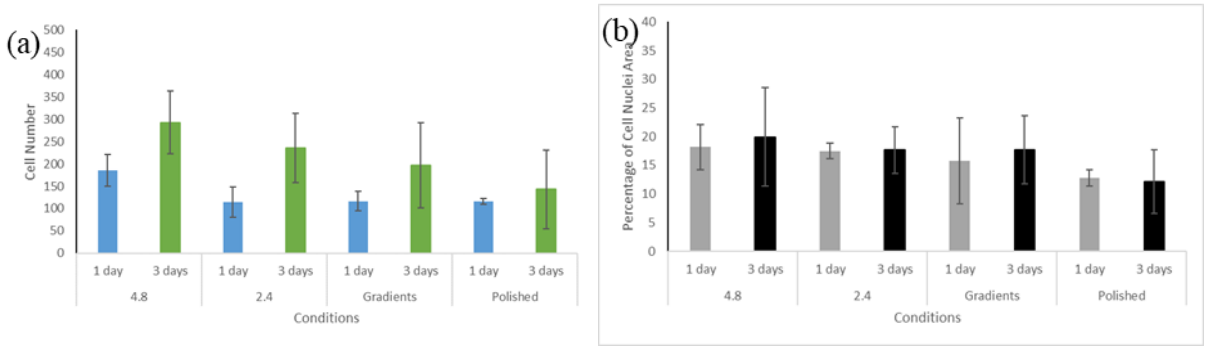

Figure 4-25 (a) Counting on cell number and (b) percentage of cell nuclei area of polished cp pure Ti samples and laser-textured cp Ti samples at line spacing of 4.8 μm, 2.4 μm and gradients that were stored in air for 7 days after 1 and 3 days of culture (including standard deviation of each condition)

4.4.4 Stored in air for 21 days

Laser treated cp Ti samples and polished samples were stored in air for 21 days before cell culture. The time point for these experiments is 1 day to discuss the number of adhered cells and percentage of cell nuclei area.

The average cell number under each condition is presented in Figure 4-26. The number of cells attached and adhered on the surfaces for line spacings of 4.8 μm and 2.4 μm dropped. The total number of cells attached and adhered on the surface for 4.8 μm spacing was reduced to about 50, while surfaces with gradients and polished surfaces attracted more cells where the number was close to 100. The average cell number for the 4.8 μm-groove-spacing was the lowest, while that for the polished was the highest. Compared with previous data, the longer those samples were left in air, the smaller the cell number after 1-day incubation was.

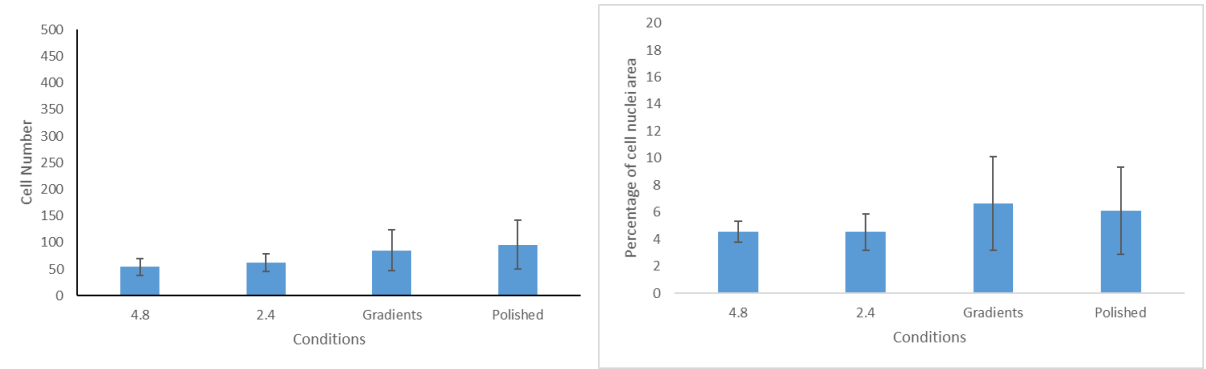

Figure 4-26 (a) Counting on cell number and (b) percentage of cell nuclei area of polished cp pure Ti samples and laser-grooved cp pure Ti samples with grooves at line spacing of 4.8 μm, 2.4 μm and gradients that were stored in air for 21 days after 1 day of cell culture.

In general, the longer the samples were stored in air, the less cells attach and adhere on the surfaces were.

4.4.5 Discussion

4.4.5.1 Surface topography

The existence of grooves affected the shape of the cells and the direction of cell spread. The narrower the line spacing was, the larger the effect of groove direction was. However, this effect became weaker when the line spacing was the narrowest, since the edges of two adjacent lines met and the inner surface of each line was smoother. When the cells were distributed over the entire surface after about 3 days, a layer of cells was formed which was less affected by surface patterns and storage conditions, only the thickness of this layer was further changed over time.

The surface roughness of all laser-treated surfaces was lower with the line width of 1 μm and line depth of 200-280 nm. Since the line spacing of grooves was no more than 10 μm that was smaller than the diameter of individual cells at about 20 μm, each of the cells covered at least 2 lines, which further had an impact on the spread and shape of cells. Because of the shallow and tightly spaced grooves, cells could not deposit at the bottom of the grooves.

It was also observed that the number of adhered cells on laser treated surfaces was lower than that on polished surfaces, which was different from most research findings since suitable surface roughness on nano and micro scales can successfully achieve osseointegration of titanium implants. It is reported that random or semi-random protrusions can hinder the effective integrin clustering and further hinder the formation of focal adhesion on the surfaces, which is crucial to cell adhesion [1]. Therefore, the change in periodicity and height of the grooves may increase or decrease the number of adhered cells.

4.4.5.2 Surface chemistry and wettability

During the early stages of bone formation, the absorption of biological fluids on the implant surface plays a key role in cell adhesion, proliferation, and differentiation [8]. In particular, cells react with the protein absorbed on the implant surface, and the proteinaceous film plays an essential role on cell behavior [51]. The formation of proteinaceous films is

affected by the absorbed water molecules. Therefore, controlling the surface wettability is crucial to ensure biocompatibility. According to previous description in surface chemistry and wettability, the contact angle of laser textured Ti surfaces increased over time when exposed to air at room temperature, and the wettability of Ti surfaces was switched from a hydrophilic state to a more hydrophobic state, while the Ti samples stored in ethanol retained their original surface state for a long period with a consistent low value of contact angle. After 7 days of storage in air at room temperature, the contact angle of laser textured Ti surfaces was between 100° and 120° approximately, which was caused by the absorption of hydrophobic groups, such as C-C/H, -CH_3, and even C-Ti. As for the samples immersed in 99% ethanol, the contact angle was still about 40° since storing in ethanol prevented carbon contamination from the air and enhance the absorption of hydrophilic groups, such as C-O and C=O. Besides, the formation of an oxide layer consisting of TiO_2 also plays an essential role on cell adhesion. The trend of increasing cell number with storage time is shown in Figure 4-27. With a change of wetting behavior from hydrophilicity to hydrophobicity on laser treated Ti surfaces, the number of cells first increased and then decreased, reaching a peak at about 7 days. There are two main factors affecting the number of adhered cells, TiO_2 and carbon contamination. TiO_2 and functional groups, C-O and C=O are beneficial for cell adhesion, while functional groups, C-C/H, -CH_3 and C-Ti, are not conducive to cell adhesion.[110] Although more C-O and C=O bonds were adsorbed on Ti surfaces when immersed in ethanol, the formation of TiO_2 oxide layer was slowed down, which resulted in the lower number of cells adhered on the surfaces compared to that on Ti surface aged in air. After 7 days of exposure to air, a TiO_2 layer formed on Ti surfaces, which resulted in more cell adhesion, although the surface was hydrophobic due to carbon contamination. As for the surfaces stored in air for a longer time, the number of cells lowered. This was probably because more carbon contamination from the air isolated the oxide layer from water molecules, which further affected the formation of proteinaceous film. Furthermore, such carbon contamination also led to a more hydrophobic surface which was detrimental for cell adhesion.

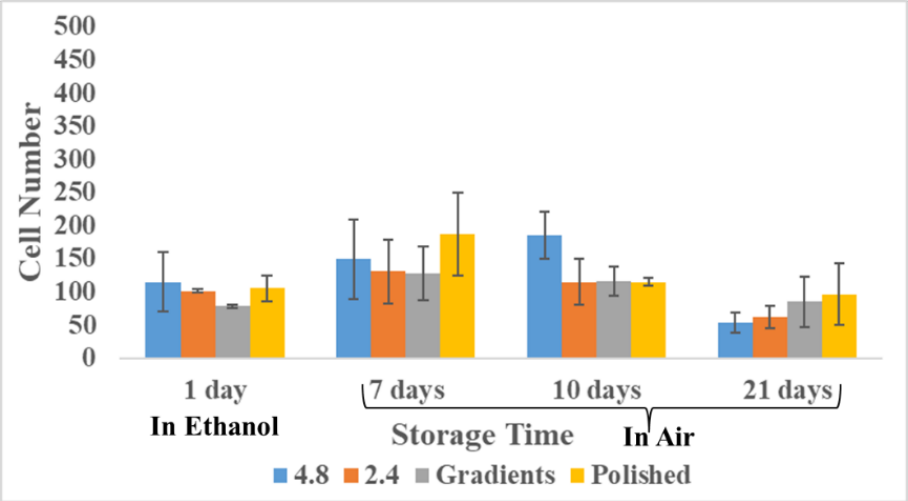

Figure 4-27 Comparation of cell number among four storage conditions (Incubation time – 1 day).

4.4.5.3 Cell culture time

The change in cell number did not follow the change in line spacing, but cells preferred to attach and adhere on the surface at line spacing in the middle values and gradients among all textured surfaces. When the incubation time was only 1 day, cell adhesion and attachment was affected by the chemical composition of the laser textured Ti surface, while after 3 days of culture, the membrane of the cells was formed, which weakened the effect of surface chemistry.

The shape of the cells, even cell nuclei, was related to the incubation time. When there were a few cells attached on the laser-grooved cp Ti surface, the cells were elongated with the grooves, and cell nuclei were oval. The formation of the cell membrane, where cells agglomerated and formed a cell layer, resulted in cells being less affected by the surface structure as the membrane layer thickens.

4.4.6 Summary

The main results from this section are summarized as follows:

1. The spread and shape of cells were closely related to the orientation and spacing of the grooves, especially when the spacing was smaller. However, when the groove spacing was reduced to the extent that lines were touching each other, the effect of line spacing was weakened.
2. Long-term cell culture reduced the effect of surface textures. Different surface patterns

had an influence on the earliest stage of cell attachment and adhesion and on the shape of cells.

3. More cells adhered to the Ti surface after exposure to air for 7 days due to the formation of a TiO_2 oxide layer and relatively little carbon contamination. High concentration of ethanol was not conducive to the early stage of cell adhesion but did not affect the long-term cell culture. The surface wetting behavior was important to the number of attached cells and subsequent growth and proliferation of cells.
4. The formation of an oxide layer consisting of TiO_2 was responsible for the better biocompatibility, and the absorption of functional groups contributed to a more hydrophilic behavior and the formation of proteinaceous film. However, the functional groups contributing to hydrophobicity (from carbon contamination for instance) were not conducive to cell adhesion.

4.5 Limitations of my work

In my study, there are some limitations. The first one is the reproducibility of laser induced structures. Due to the surface morphology of polished samples and the 0.2 mm^2 size of scanned point by point sensor, the laser beam was able to be not in-focus at some points, which resulted in the lower reproducibility of surface structures. The second one is the number of tests completed. Since the preparation time for each Ti samples could take up to 3 hours, only three samples were prepared per condition for contact angle measurements, as well as for every set of cell culture experiments. As for the XPS analysis, due to the transportation limitation (samples had to be shipped to Queen's University), only one sample of each surface parameter were prepared. The third one is the contact angle variation, the drop size. The drop size was calculated by manual, so there was a 1% ~ 5% error. Another limitation is caused by the ImageJ software during contact angle calculation and cell number counting, where more precise analytical software is needed.

5. Conclusion

In this thesis, surface texturing of cp Ti surfaces induced by a femtosecond laser surface direct writing technique was explored as a potential method to control wettability, surface chemistry and to improve osseointegration. By controlling the laser process parameters such as laser beam power and line spacing, two different surface textures composed of grooves were produced on Ti surfaces, which were uniform grooves spaced 10 μm, 4.8 μm, 2.4 μm and 1.2 μm as well as a gradient in groove spacings. The surface features were found to be very reproducible after introducing a chromatic confocal point sensor system before laser machining, to ensure that the laser is focused on the sample surface at all times during texturing.

X-ray Photoelectron Spectroscopy (XPS) confirmed that the main composition of the oxide layer on laser treated Ti surfaces was TiO_2. Laser texturing, which was carried out in air, promoted the oxidation of the Ti surfaces, which further enhanced the hydrophilicity of surfaces as demonstrated via contact angle measurements. However, carbon contamination from the air accumulated on the Ti samples over time, which led to a transition in wetting behavior from hydrophilic to hydrophobic. Polishing of the Ti surfaces prior to laser machining helped to remove the native oxide layer. The formation of titanium oxides and the continuous carbon absorption (via e.g. CO_2 decomposition) resulted in fluctuations in the surface chemistry on Ti surfaces as well as fluctuation in contact angle.

Laser texturing accelerated the evolution of wettability of distilled water on laser-grooved cp Ti surfaces compared with polished surfaces. The anisotropy of surface structures (i.e. unidirectional grooves) resulted in an anisotropy in wetting behavior, where drops elongated along the grooves resulting in a lower contact angle in the groove direction. Ti surfaces changed from hydrophilicity to hydrophobicity when exposed to air because of an increase in carbon content on the surface. However, Ti surfaces were retained their hydrophilic state if they were stored in ethanol.

The surface topography affected the spread, shape and attachment of MG 63s osteoblast-like cells. The presence of grooves resulted in a spread of the cells along the

groove direction. The number of adhered cells was found to be independent of surface textures, and there were no differences between all laser treated surfaces. However, the laser textured Ti surfaces decreased the number of adhered cells when compared with polished surfaces. The shape of cell nuclei was affected by surface structure at the early stage of cell culture, when there were few cells adhered on the surface. The cell nuclei shape was then independent of surface textures once a layer of cells was formed that covered the entire surface. Cell growth and proliferation were not affected by the surface structure, only by the incubation time. A cell membrane formed after 3 to 7 days of incubation. Cells preferred to attach to hydrophilic surfaces but can also attach to hydrophobic surfaces if an oxide layer was formed on these surfaces.

6. Future Work

Based on the results obtained in this thesis, some directions for future work are proposed here and cover three aspects of the research, namely, laser texturing, surface properties and cell behavior.

The generation of more complicated and novel surface structures needs to be explored to improve cell adhesion. For instance, the laser processing environment could be changed (e.g. vacuum, water, O_2) to tailor the surface chemistry (oxidation).

As for the surface properties, the mechanical properties of laser treated surfaces, such as hardness and Young's modulus, and the corrosion and friction resistance should be investigated, since they could determine the service life of implants. A critical step in cell adhesion is the formation of proteinaceous film on implant surfaces. Therefore, it is crucial to investigate the surface wetting behavior by protein solutions, and not only using distilled water as was done in this thesis. Another important effect that needs more work is the photocatalytic activities of TiO_2 generated by laser treatment and how this activity can affect the chemistry of laser treated surfaces.

Surface biocompatibility is a complex process that needs further exploration. For example, the cell attachment and detachment can be analyzed to study the focal adhesion on laser treated Ti surfaces. The formation of proteinaceous film on laser treated Ti surfaces can be studied as well by immersing samples in simulated proteinaceous solution. Besides, the toxicity of the oxide layer induced by the laser texturing can be inspected. Finally, the ultimate goal is to promote bone growth on Ti surfaces, and thus analysis of bone nodule formation on laser treated surfaces is a logical next step.

References

[1] A. Cunha, “Multiscale Femtosecond Laser Surface Texturing of Titanium and Titanium Alloys for Dental and Orthopaedic Implants,” no. JANUARY, pp. 1–294, 2015.

[2] J. W. Nicholson, “Titanium Alloys for Dental Implants: A Review,” *Prosthesis*, vol. 2, no. 2, pp. 100–116, 2020, doi: 10.3390/prosthesis2020011.

[3] M. Geetha, A. K. Singh, R. Asokamani, and A. K. Gogia, “Ti based biomaterials, the ultimate choice for orthopaedic implants - A review,” *Prog. Mater. Sci.*, vol. 54, no. 3, pp. 397–425, 2009, doi: 10.1016/j.pmatsci.2008.06.004.

[4] “Dental Implants,” *Nov 16, 2020*. https://hiossen.com/news/how-long-should-implants-last/.

[5] “Knee Replacement,” *Aug 27, 2020*. https://www.hss.edu/conditions_revision-total-knee-replacement-faqs.asp.

[6] “Hip Implants,” *Nov 16, 2011*. https://www.zimmerbiomet.com/patients-caregivers/article/hip/hip-replacement-longevity.html.

[7] D. M. Dohan Ehrenfest, P. G. Coelho, B.-S. Kang, Y.-T. Sul, and T. Albrektsson, “Classification of osseointegrated implant surfaces: materials, chemistry and topography,” *Trends Biotechnol. (Regular ed.)*, vol. 28, no. 4, pp. 198–206, 2009, doi: 10.1016/j.tibtech.2009.12.003.

[8] P. Koegler, A. Clayton, H. Thissen, G. N. C. Santos, and P. Kingshott, “The influence of nanostructured materials on biointerfacial interactions,” *Adv. Drug Deliv. Rev.*, vol. 64, no. 15, pp. 1820–1839, 2012, doi: 10.1016/j.addr.2012.06.001.

[9] K. Anselme, P. Davidson, A. M. Popa, M. Giazzon, M. Liley, and L. Ploux, “The interaction of cells and bacteria with surfaces structured at the nanometre scale,” *Acta Biomater.*, vol. 6, no. 10, pp. 3824–3846, 2010, doi: 10.1016/j.actbio.2010.04.001.

[10] F. Barrère, T. A. Mahmood, K. de Groot, and C. A. van Blitterswijk, “Advanced biomaterials for skeletal tissue regeneration: Instructive and smart functions,” *Mater. Sci. Eng. R. Rep.*, vol. 59, no. 1, pp. 38–71, 2008, doi: 10.1016/j.mser.2007.12.001.

[11] X. Liu, P. K. Chu, and C. Ding, “Surface modification of titanium, titanium alloys, and related materials for biomedical applications,” *Mater. Sci. Eng. R. Rep.*, vol. 47, no. 3, pp. 49–121, 2004, doi: 10.1016/j.mser.2004.11.001.

[12] J. J. Norman and T. A. Desai, “Methods for Fabrication of Nanoscale Topography for Tissue Engineering Scaffolds,” *Ann. Biomed. Eng.*, vol. 34, no. 1, pp. 89–101, 2006, doi: 10.1007/s10439-005-9005-4.

[13] A. Y. Vorobyev and C. Guo, “Direct femtosecond laser surface nano/microstructuring and its applications,” *Laser Photon. Rev.*, vol. 7, no. 3, pp. 385–407, 2013, doi: 10.1002/lpor.201200017.

[14] M. Saini, “Implant biomaterials: A comprehensive review,” *World J. Clin. Cases*, vol. 3, no. 1, p. 52, 2015, doi: 10.12998/wjcc.v3.i1.52.

[15] M. Devices, *Biomaterials in Clinical Practice*. 2018.

[16] S. Tharani Kumar, S. Prasanna Devi, C. Krithika, and R. Raghavan, “Review of metallic biomaterials in dental applications,” *J. Pharm. bioallied Sci.*, vol. 12, no. 5, pp. 14–19, 2020, doi: 10.4103/jpbs.JPBS_88_20.

[17] M. Plecko *et al.*, “Osseointegration and biocompatibility of different metal implants--a comparative experimental investigation in sheep,” *BMC Musculoskelet. Disord.*, vol. 13, no. 1, p. 32, 2012, doi: 10.1186/1471-2474-13-32.

[18] R. S. BOCKMAN, A. L. BOSKEY, N. C. BLUMENTHAL, N. W. ALCOCK, and R. P. J. R. WARRELL, “Gallium increases bone calcium and crystallite perfection of hydroxyapatite,” *Calcif. Tissue Int.*, vol. 39, no. 6, pp. 376–381, 1986, doi: 10.1007/BF02555174.

[19] K. Liao, “Performance characterization and modeling of a composite hip prosthesis,”

Exp. Tech. (Westport, Conn.), vol. 18, no. 5, pp. 33–38, 1994, doi: 10.1111/j.1747-1567.1994.tb00303.x.

[20] S. M. Kurtz and J. N. Devine, "PEEK biomaterials in trauma, orthopedic, and spinal implants," *Biomaterials*, vol. 28, no. 32, pp. 4845–4869, 2007, doi: 10.1016/j.biomaterials.2007.07.013.

[21] B. Lethaus *et al.*, "A treatment algorithm for patients with large skull bone defects and first results," *J. cranio-maxillo-facial Surg.*, vol. 39, no. 6, pp. 435–440, 2010, doi: 10.1016/j.jcms.2010.10.003.

[22] D. J. Kelsey, G. S. Springer, and S. B. Goodman, "Composite Implant for Bone Replacement," *J. Compos. Mater.*, vol. 31, no. 16, pp. 1593–1632, 1997, doi: 10.1177/002199839703101603.

[23] A. Schwitalla and W.-D. Müller, "PEEK dental implants: a review of the literature," *J. Oral Implantol.*, vol. 39, no. 6, pp. 743–749, 2013, doi: 10.1563/AAID-JOI-D-11-00002.

[24] C.-M. Han *et al.*, "The electron beam deposition of titanium on polyetheretherketone (PEEK) and the resulting enhanced biological properties," *Biomaterials*, vol. 31, no. 13, pp. 3465–3470, 2009, doi: 10.1016/j.biomaterials.2009.12.030.

[25] F. Mussano, T. Genova, L. Munaron, M. G. Faga, and S. Carossa, "Ceramic Biomaterials for Dental Implants: Current Use and Future Perspectives," *Dent. Implantol. Biomater.*, 2016, doi: 10.5772/62701.

[26] M. Geetha, A. K. Singh, R. Asokamani, and A. K. Gogia, "Ti based biomaterials, the ultimate choice for orthopaedic implants – A review," *Prog. Mater. Sci.*, vol. 54, no. 3, pp. 397–425, 2009, doi: 10.1016/j.pmatsci.2008.06.004.

[27] Q. Wang *et al.*, "Multi-scale surface treatments of titanium implants for rapid osseointegration: A review," *Nanomaterials*, vol. 10, no. 6, pp. 1–27, 2020, doi: 10.3390/nano10061244.

[28] S. A. Alves *et al.*, “Synthesis of calcium-phosphorous doped TiO 2 nanotubes by anodization and reverse polarization: A promising strategy for an efficient biofunctional implant surface,” *Appl. Surf. Sci.*, vol. 399, pp. 682–701, 2017, doi: 10.1016/j.apsusc.2016.12.105.

[29] R. D. Jamison and L. N. Gilbertson, *Composite Materials for Implant Applications in the Human Body; Characterization and Testing*, no. 1178. 1993.

[30] D. Bombač, M. Brojan, P. Fajfar, F. Kosel, and R. Turk, “Review of materials in medical applications,” *RMZ – Mater. Geoenvironment*, vol. 54, no. 54, pp. 471–499, 2007, [Online]. Available: http://www.rmz-mg.com/letniki/rmz54/RMZ54_0471-0499.pdf.

[31] T. W. Wright, “Definitions in Biomaterials: D. F. Williams (Ed.), Elsevier, Amsterdam, 1987, 72 pp,” *Journal of Biomechanics*, vol. 22, no. 1. Elsevier Ltd, p. 79, 1989, doi: 10.1016/0021-9290(89)90188-7.

[32] M. Long and H. J. Rack, “Titanium alloys in total joint replacement—a materials science perspective,” *Biomaterials*, vol. 19, no. 18, pp. 1621–1639, 1998, doi: 10.1016/S0142-9612(97)00146-4.

[33] K. Kieswetter, Z. Schwartz, D. D. Dean, and B. D. Boyan, “The role of implant surface characteristics in the healing of bone,” *Crit. Rev. oral Biol. Med.*, vol. 7, no. 4, pp. 329–345, 1996, doi: 10.1177/10454411960070040301.

[34] G. R. Holt, S. M. Parel, and P. I. Branemark, “Osseointegrated Titanium Implants,” *Facial Plast. Surg.*, vol. 3, no. 2, pp. 113–124, 1986, doi: 10.1055/s-2008-1064831.

[35] A. Carvalho, L. Cangueiro, V. Oliveira, R. Vilar, M. H. Fernandes, and F. J. Monteiro, “Femtosecond laser microstructured Alumina toughened Zirconia: A new strategy to improve osteogenic differentiation of hMSCs,” *Appl. Surf. Sci.*, vol. 435, pp. 1237–1245, 2018, doi: 10.1016/j.apsusc.2017.11.206.

[36] S. P. Leo Kumar and D. Avinash, “Review on effect of Ti-alloy processing techniques on surface-integrity for biomedical application,” *Mater. Manuf. Process.*, vol. 35, no. 8,

pp. 869–892, 2020, doi: 10.1080/10426914.2020.1748195.

[37] K. Wang, “The use of titanium for medical applications in the USA,” *Mater. Sci. Eng. A. Struct. Mater.*, vol. 213, no. 1, pp. 134–137, 1996, doi: 10.1016/0921-5093(96)10243-4.

[38] W. F. Cui, Z. Jin, A. H. Guo, and L. Zhou, “High temperature deformation behavior of α + β-type biomedical titanium alloy Ti–6Al–7Nb,” *Mater. Sci. Eng. A. Struct. Mater.*, vol. 499, no. 1, pp. 252–256, 2009, doi: 10.1016/j.msea.2007.11.109.

[39] W.-S. Lee and C.-W. Chen, “High temperature impact properties and dislocation substructure of Ti–6Al–7Nb biomedical alloy,” *Mater. Sci. Eng. A. Struct. Mater.*, vol. 576, pp. 91–100, 2013, doi: 10.1016/j.msea.2013.03.088.

[40] K.-H. Frosch and K. M. Stürmer, “Metallic Biomaterials in Skeletal Repair,” *Eur. J. trauma*, vol. 32, no. 2, pp. 149–159, 2006, doi: 10.1007/s00068-006-6041-1.

[41] O. A. Golosova, M. B. Ivanov, Y. R. Kolobov, and T. N. Vershinina, “Structure and properties of low modulus titanium alloy Ti-26Nb-7Mo-12Zr,” *Mater. Sci. Technol.*, vol. 29, no. 2, pp. 204–209, 2013, doi: 10.1179/1743284712Y.0000000128.

[42] Z. Lijian, C. Ti–Sheng, W. Wei, and C. Lei, “Study of commercially pure titanium implants bone integration mechanism,” *Eur. J. Plast. Surg.*, vol. 23, no. 6, pp. 301–304, 2000, doi: 10.1007/s002380000165.

[43] L. Sennerby, P. Thomsen, and L. E. Ericson, “Early tissue response to titanium implants inserted in rabbit cortical bone: Part II Ultrastructural observations,” *J. Mater. Sci. Mater. Med.*, vol. 4, no. 5, pp. 494–502, 1993, doi: 10.1007/BF00120129.

[44] Y. Bai *et al.*, “Characterization, corrosion behavior, cellular response and in vivo bone tissue compatibility of titanium–niobium alloy with low Young’s modulus,” *Mater. Sci. Eng. C*, vol. 59, pp. 565–576, 2016, doi: 10.1016/j.msec.2015.10.062.

[45] W. Elmay *et al.*, “Optimisation of mechanical properties of Ti-Nb binary alloys for biomedical applications,” *Comput. Methods Biomech. Biomed. Engin.*, vol. 14, no. sup1, pp. 119–120, 2011, doi: 10.1080/10255842.2011.593760.

[46] Y. Zhu *et al.*, “Superelastic and shape memory properties of Ti x Nb3Zr2Ta alloys,” *J. Mech. Behav. Biomed. Mater.*, vol. 12, pp. 151–159, 2012, doi: 10.1016/j.jmbbm.2012.02.010.

[47] H. G. Hanumantharaju and H. K. Shivanand, “Strength analysis & comparison of SS316L, Ti-6Al-4V & Ti-35Nb-7Zr-5Ta used as orthopaedic implant materials by FEA,” *ICBEE*. IEEE, pp. 101–105, 2010, doi: 10.1109/ICBEE.2010.5649282.

[48] W. Chrzanowski, E. A. A. Neel, D. A. Armitage, and J. C. Knowles, “Effect of surface treatment on the bioactivity of nickel–titanium,” *Acta Biomater.*, vol. 4, no. 6, pp. 1969–1984, 2008, doi: 10.1016/j.actbio.2008.05.010.

[49] N. Mitsuo, “Overview of Metals and Applications.” Elsevier, p. 2, 2019.

[50] P. Tengvall, A. Askendal, H. Elwing, and I. Lundström, “A model for the interaction between titanium and living systems,” *Biofouling (Chur, Switzerland)*, vol. 4, no. 1–3, pp. 219–223, 1991, doi: 10.1080/08927019109378212.

[51] B. Kasemo, “Biocompatibility of titanium implants: Surface science aspects,” *J. Prosthet. Dent.*, vol. 49, no. 6, pp. 832–837, 1983, doi: 10.1016/0022-3913(83)90359-1.

[52] S. Mohammadi, M. Esposito, L. Wictorin, B.-O. Aronsson, and P. Thomsen, “Bone response to machined cast titanium implants,” *J. Mater. Sci.*, vol. 36, no. 8, pp. 1987–1993, 2001, doi: 10.1023/A:1017518629057.

[53] H. Assender, V. Bliznyuk, and K. Porfyrakis, “How Surface Topography Relates to Materials’ Properties,” *Sci. (American Assoc. Adv. Sci.*, vol. 297, no. 5583, pp. 973–976, 2002, doi: 10.1126/science.1074955.

[54] J. M. Ayllón, C. Navarro, J. Vázquez, and J. Domínguez, “Fatigue life estimation in dental implants,” *Eng. Fract. Mech.*, vol. 123, pp. 34–43, 2014, doi: 10.1016/j.engfracmech.2014.03.011.

[55] R. Strietzel, A. Hösch, H. Kalbfleisch, and D. Buch, “In vitro corrosion of titanium,” *Biomaterials*, vol. 19, no. 16, pp. 1495–1499, 1998, doi:

10.1016/S0142-9612(98)00065-9.

[56] L. Reclaru and J.-M. Meyer, “Effects of fluorides on titanium and other dental alloys in dentistry,” *Biomaterials*, vol. 19, no. 1, pp. 85–92, 1998, doi: 10.1016/S0142-9612(97)00179-8.

[57] N. Schiff, B. Grosgogeat, M. Lissac, and F. Dalard, “Influence of fluoride content and pH on the corrosion resistance of titanium and its alloys,” *Biomaterials*, vol. 23, no. 9, pp. 1995–2002, 2002, doi: 10.1016/S0142-9612(01)00328-3.

[58] J. Löberg, I. Mattisson, S. Hansson, and E. Ahlberg, “Characterisation of Titanium Dental Implants I: Critical Assessment of Surface Roughness Parameters,” *Open Biomater. J.*, vol. 2, pp. 18–35, 2010, doi: 10.2174/1876502501002010018.

[59] W. D. Müeller *et al.*, “Evaluation of the interface between bone and titanium surfaces being blasted by aluminium oxide or bioceramic particles,” *Clin. Oral Implants Res.*, vol. 14, no. 3, pp. 349–356, 2003, doi: 10.1034/j.1600-0501.2003.00791.x.

[60] L. Hao and J. Lawrence, *Laser Surface Treatment of Bio-Implant Materials*. 2006.

[61] G. Marenzi, F. Impero, F. Scherillo, J. C. Sammartino, A. Squillace, and G. Spagnuolo, “Effect of different surface treatments on titanium dental implant micro-morphology,” *Materials (Basel).*, vol. 12, no. 5, 2019, doi: 10.3390/ma12050733.

[62] F. Wang, C. Li, S. Zhang, and H. Liu, “Tantalum coated on titanium dioxide nanotubes by plasma spraying enhances cytocompatibility for dental implants,” *Surf. Coatings Technol.*, vol. 382, no. October 2019, p. 125161, 2020, doi: 10.1016/j.surfcoat.2019.125161.

[63] G. Marenzi, G. Spagnuolo, J. C. Sammartino, R. Gasparro, A. Rebaudi, and M. Salerno, “Micro-scale surface patterning of titanium dental implants by anodization in the presence of modifying salts,” *Materials (Basel).*, vol. 12, no. 11, 2019, doi: 10.3390/ma12111753.

[64] A. Pimpin and W. Srituravanich, “Reviews on micro- and nanolithography techniques

and their applications," *Eng. J.*, vol. 16, no. 1, pp. 37–55, 2012, doi: 10.4186/ej.2012.16.1.37.

[65] M. J. Madou, *Fundamentals of microfabrication : the science of miniaturization* , Second edi. Boca Raton, FL: CRC Press, an imprint of Taylor and Francis, 2002.

[66] M. Altissimo, "E-beam lithography for micro-/nanofabrication," *Biomicrofluidics*, vol. 4, no. 2, pp. 26503–26506, 2010, doi: 10.1063/1.3437589.

[67] C. Vieu *et al.*, "Electron beam lithography: resolution limits and applications," *Appl. Surf. Sci.*, vol. 164, no. 1, pp. 111–117, 2000, doi: 10.1016/S0169-4332(00)00352-4.

[68] A. E. Grigorescu and C. W. Hagen, "Resists for sub-20-nm electron beam lithography with a focus on HSQ: state of the art," *Nanotechnology*, vol. 20, no. 29, p. 292001, 2009, doi: 10.1088/0957-4484/20/29/292001.

[69] R. F. Pease and S. Y. Chou, "Lithography and Other Patterning Techniques for Future Electronics," *Proc. IEEE*, vol. 96, no. 2, pp. 248–270, 2008, doi: 10.1109/JPROC.2007.911853.

[70] D. Banerjee and J. C. Williams, "Perspectives on Titanium Science and Technology," *Acta Mater.*, vol. 61, no. 3, pp. 844–879, 2013, doi: 10.1016/j.actamat.2012.10.043.

[71] F. J. C. Braga, R. F. C. Marques, E. de A. Filho, and A. C. Guastaldi, "Surface modification of Ti dental implants by Nd:YVO 4 laser irradiation," *Appl. Surf. Sci.*, vol. 253, no. 23, pp. 9203–9208, 2007, doi: 10.1016/j.apsusc.2007.05.048.

[72] J. Helenius, C.-P. Heisenberg, H. E. Gaub, and D. J. Muller, "Single-cell force spectroscopy," *J. Cell Sci.*, vol. 121, no. 11, pp. 1785–1791, 2008, doi: 10.1242/jcs.030999.

[73] K. C. Phillips, H. H. Gandhi, E. Mazur, and S. K. Sundaram, "Ultrafast laser processing of materials: a review," *Adv. Opt. Photonics*, vol. 7, no. 4, p. 684, 2015, doi: 10.1364/aop.7.000684.

[74] K. Ahmmed, C. Grambow, and A.-M. Kietzig, "Fabrication of Micro/Nano Structures

on Metals by Femtosecond Laser Micromachining," *Micromachines (Basel)*, vol. 5, no. 4, pp. 1219–1253, 2014, doi: 10.3390/mi5041219.

[75] H. Exir and A. Weck, "Mechanism of superhydrophilic to superhydrophobic transition of femtosecond laser-induced periodic surface structures on titanium," *Surf. Coatings Technol.*, vol. 378, no. May, pp. 3–8, 2019, doi: 10.1016/j.surfcoat.2019.124931.

[76] M. A. Arenas, J. I. Ahuir-Torres, I. García, H. Carvajal, and J. de Damborenea, "Tribological behaviour of laser textured Ti6Al4V alloy coated with MoS2 and graphene," *Tribol. Int.*, vol. 128, no. April, pp. 240–247, 2018, doi: 10.1016/j.triboint.2018.07.031.

[77] M. Tsukamoto *et al.*, "Periodic microstructures produced by femtosecond laser irradiation on titanium plate," *Vacuum*, vol. 80, no. 11, pp. 1346–1350, 2006.

[78] P. Bizi-Bandoki, S. Valette, E. Audouard, and S. Benayoun, "Time dependency of the hydrophilicity and hydrophobicity of metallic alloys subjected to femtosecond laser irradiations," *Appl. Surf. Sci.*, vol. 273, pp. 399–407, 2013, doi: 10.1016/j.apsusc.2013.02.054.

[79] M. Groenendijk and J. Meijer, "Microstructuring using femtosecond pulsed laser ablation," *Int. Congr. Appl. Lasers Electro-Optics*, vol. 2005, no. 1, p. M408, 2005, doi: 10.2351/1.5060548.

[80] J. I. Ahuir-Torres, M. A. Arenas, W. Perrie, G. Dearden, and J. de Damborenea, "Surface texturing of aluminium alloy AA2024-T3 by picosecond laser: Effect on wettability and corrosion properties," *Surf. Coatings Technol.*, vol. 321, pp. 279–291, 2017, doi: 10.1016/j.surfcoat.2017.04.056.

[81] A. Samanta, Q. Wang, S. K. Shaw, and H. Ding, "Roles of chemistry modification for laser textured metal alloys to achieve extreme surface wetting behaviors," *Mater. Des.*, vol. 192, p. 108744, 2020, doi: 10.1016/j.matdes.2020.108744.

[82] J. Long, M. Zhong, H. Zhang, and P. Fan, "Superhydrophilicity to superhydrophobicity

transition of picosecond laser microstructured aluminum in ambient air," *J. Colloid Interface Sci.*, vol. 441, pp. 1–9, 2015, doi: 10.1016/j.jcis.2014.11.015.

[83] B. Wu, M. Zhou, J. Li, X. Ye, G. Li, and L. Cai, "Superhydrophobic surfaces fabricated by microstructuring of stainless steel using a femtosecond laser," *Appl. Surf. Sci.*, vol. 256, no. 1, pp. 61–66, 2009.

[84] O. Raimbault *et al.*, "The effects of femtosecond laser-textured Ti-6Al-4V on wettability and cell response," *Mater. Sci. Eng. C*, vol. 69, pp. 311–320, 2016, doi: 10.1016/j.msec.2016.06.072.

[85] Z. Yu, S. Yin, W. Zhang, X. Jiang, and J. Hu, "Picosecond laser texturing on titanium alloy for biomedical implants in cell proliferation and vascularization," *J. Biomed. Mater. Res. - Part B Appl. Biomater.*, vol. 108, no. 4, pp. 1494–1504, 2020, doi: 10.1002/jbm.b.34497.

[86] A. S. Goldstein, "Cell adhesion," *Tissue Eng. Artif. Organs*, pp. 503–519, 2016, doi: 10.1007/springerreference_66410.

[87] M. C. Advincula, F. G. Rahemtulla, R. C. Advincula, E. T. Ada, J. E. Lemons, and S. L. Bellis, "Osteoblast adhesion and matrix mineralization on sol–gel-derived titanium oxide," *Biomaterials*, vol. 27, no. 10, pp. 2201–2212, 2006, doi: 10.1016/j.biomaterials.2005.11.014.

[88] Y. Zhang *et al.*, "Osteogenic properties of hydrophilic and hydrophobic titanium surfaces evaluated with osteoblast-like cells (MG63) in coculture with human umbilical vein endothelial cells (HUVEC)," *Dent. Mater.*, vol. 26, no. 11, pp. 1043–1051, 2010, doi: 10.1016/j.dental.2010.07.003.

[89] K. Anselme, "Osteoblast adhesion on biomaterials," *Biomaterials*, vol. 21, no. 7, pp. 667–681, 2000, doi: 10.1016/S0142-9612(99)00242-2.

[90] J. Lincks *et al.*, "Response of MG63 osteoblast-like cells to titanium and titanium alloy is dependent on surface roughness and composition," *Biomater. Silver Jubil. Compend.*,

vol. 19, pp. 147–160, 1998, doi: 10.1016/B978-008045154-1.50019-8.

[91] M. Otero *et al.*, “Human Cell Culture Protocols,” vol. 806, pp. 301–336, 2012, doi: 10.1007/978-1-61779-367-7.

[92] R. G. Flemming, C. J. Murphy, G. A. Abrams, S. L. Goodman, and P. F. Nealey, “Effects of synthetic micro- and nano-structured surfaces on cell behavior,” *Biomaterials*, vol. 20, no. 6, pp. 573–588, 1999, doi: 10.1016/S0142-9612(98)00209-9.

[93] M. Bachle and R. J. Kohal, “A systematic review of the influence of different titanium surfaces on proliferation, differentiation and protein synthesis of osteoblast-like MG63 cells,” *Clin. Oral Implants Res.*, vol. 15, no. 6, pp. 683–692, 2004, doi: 10.1111/j.1600-0501.2004.01054.x.

[94] A. Bagno and C. Di Bello, “Surface treatments and roughness properties of Ti-based biomaterials,” *J. Mater. Sci. Mater. Med.*, vol. 15, no. 9, pp. 935–949, 2004, doi: 10.1023/B:JMSM.0000042679.28493.7f.

[95] X. Zhu, J. Chen, L. Scheideler, R. Reichl, and J. Geis-Gerstorfer, “Effects of topography and composition of titanium surface oxides on osteoblast responses,” *Biomaterials*, vol. 25, no. 18, pp. 4087–4103, 2004, doi: 10.1016/j.biomaterials.2003.11.011.

[96] D. A. Puleo and A. Nanci, “Understanding and controlling the bone–implant interface,” *Biomaterials*, vol. 20, no. 23, pp. 2311–2321, 1999, doi: 10.1016/S0142-9612(99)00160-X.

[97] L. Hao, J. Lawrence, and K. S. Chian, “Osteoblast cell adhesion on a laser modified zirconia based bioceramic,” *J. Mater. Sci. Mater. Med.*, vol. 16, no. 8, pp. 719–726, 2005, doi: 10.1007/s10856-005-2608-3.

[98] M. I. Janssen, M. B. M. va. Leeuwen, T. G. va. Kooten, J. d. Vries, L. Dijkhuizen, and H. A. B. Wösten, “Promotion of fibroblast activity by coating with hydrophobins in the β-sheet end state,” *Biomaterials*, vol. 25, no. 14, pp. 2731–2739, 2004, doi: 10.1016/j.biomaterials.2003.09.060.

[99] R. E. Baier, “Surface behaviour of biomaterials: The theta surface for biocompatibility,” *J. Mater. Sci. Mater. Med.*, vol. 17, no. 11, pp. 1057–1062, 2006, doi: 10.1007/s10856-006-0444-8.

[100] F. Rupp, L. Scheideler, and J. Geis-Gerstorfer, “Effect of Heterogenic Surfaces on Contact Angle Hysteresis: Dynamic Contact Angle Analysis in Material Sciences,” *Chem. Eng. Technol.*, vol. 25, no. 9, pp. 877–882, 2002, doi: 10.1002/1521-4125(20020910)25:9<877::AID-CEAT877>3.0.CO;2-D.

[101] H. Zreiqat *et al.*, “The effect of surface chemistry modification of titanium alloy on signalling pathways in human osteoblasts,” *Biomaterials*, vol. 26, no. 36, pp. 7579–7586, 2005, doi: 10.1016/j.biomaterials.2005.05.024.

[102] D. Falconnet, G. Csucs, H. Michelle Grandin, and M. Textor, “Surface engineering approaches to micropattern surfaces for cell-based assays,” *Biomaterials*, vol. 27, no. 16, pp. 3044–3063, 2006, doi: 10.1016/j.biomaterials.2005.12.024.

[103] W. Senaratne, L. Andruzzi, and C. K. Ober, “Self-Assembled Monolayers and Polymer Brushes in Biotechnology: Current Applications and Future Perspectives,” *Biomacromolecules*, vol. 6, no. 5, pp. 2427–2448, 2005, doi: 10.1021/bm050180a.

[104] B. G. Keselowsky, D. M. Collard, A. J. García, and S. Weinbaum, “Integrin Binding Specificity Regulates Biomaterial Surface Chemistry Effects on Cell Differentiation,” *Proc. Natl. Acad. Sci. - PNAS*, vol. 102, no. 17, pp. 5953–5957, 2005, doi: 10.1073/pnas.0407356102.

[105] J. N. Barbosa, P. Madureira, M. A. Barbosa, and A. P. Águas, “The influence of functional groups of self-assembled monolayers on fibrous capsule formation and cell recruitment,” *J. Biomed. Mater. Res. A*, vol. 76A, no. 4, pp. 737–743, 2006, doi: 10.1002/jbm.a.30602.

[106] R. A. Gittens, R. Olivares-Navarrete, Z. Schwartz, and B. D. Boyan, “Implant osseointegration and the role of microroughness and nanostructures: lessons for spine implants,” *Acta Biomater.*, vol. 10, no. 8, pp. 3363–3371, Aug. 2014, doi:

10.1016/j.actbio.2014.03.037.

[107] M. Kubiak, W. Piekarska, and S. Stano, “Modelling of laser beam heat source based on experimental research of Yb:YAG laser power distribution,” *Int. J. Heat Mass Transf.*, vol. 83, pp. 679–689, 2015, doi: 10.1016/j.ijheatmasstransfer.2014.12.052.

[108] L. Jiao, Z. Y. Chua, S. K. Moon, J. Song, G. Bi, and H. Zheng, “Femtosecond laser produced hydrophobic hierarchical structures on additive manufacturing parts,” *Nanomaterials*, vol. 8, no. 8, 2018, doi: 10.3390/nano8080601.

[109] C. juan Yang, X. song Mei, Y. ling Tian, D. wei Zhang, Y. Li, and X. ping Liu, “Modification of wettability property of titanium by laser texturing,” *Int. J. Adv. Manuf. Technol.*, vol. 87, no. 5–8, pp. 1663–1670, 2016, doi: 10.1007/s00170-016-8601-9.

[110] Y. Oshida, *Bioscience and bioengineering of titanium materials*, 2nd ed. S.l: Elsevier, 2013.

[111] D. Bäuerle, *Laser Processing and Chemistry*, 4. Berlin, Heidelberg: Springer Berlin Heidelberg, 2011.

[112] Y.-T. Sul *et al.*, “Characteristics of the surface oxides on turned and electrochemically oxidized pure titanium implants up to dielectric breakdown:: the oxide thickness, micropore configurations, surface roughness, crystal structure and chemical composition,” *Biomaterials*, vol. 23, no. 2, pp. 491–501, 2002, doi: 10.1016/S0142-9612(01)00131-4.

[113] A.-M. Kietzig, S. G. Hatzikiriakos, and P. Englezos, “Patterned Superhydrophobic Metallic Surfaces,” *Langmuir*, vol. 25, no. 8, pp. 4821–4827, 2009, doi: 10.1021/la8037582.

[114] L. B. Boinovich, A. M. Emelyanenko, K. A. Emelyanenko, A. G. Domantovsky, and A. A. Shiryaev, “Comment on ‘Nanosecond laser textured superhydrophobic metallic surfaces and their chemical sensing applications’ by Duong V. Ta, Andrew Dunn, Thomas J. Wasley, Robert W. Kay, Jonathan Stringer, Patrick J. Smith, Colm

Connaughton, Jonathan D. Shephard (Ap," *Appl. Surf. Sci.*, vol. 379, pp. 111–113, 2016, doi: 10.1016/j.apsusc.2016.04.056.

[115] M. Stepien *et al.*, "Surface chemical analysis of photocatalytic wettability conversion of TiO 2 nanoparticle coating," *Surf. Coatings Technol.*, vol. 208, pp. 73–79, 2012, doi: 10.1016/j.surfcoat.2012.08.008.

[116] K. Katsiev *et al.*, "Mechanism of Ethanol Photooxidation on Single-Crystal Anatase TiO2(101)," *J. Phys. Chem. C*, vol. 121, no. 5, pp. 2940–2950, 2017, doi: 10.1021/acs.jpcc.6b12776.

[117] M. Xu, A. Zada, R. Yan, H. Li, N. Sun, and Y. Qu, "Ti2O3/TiO2 heterophase junctions with enhanced charge separation and spatially separated active sites for photocatalytic CO2 reduction," *Phys. Chem. Chem. Phys.*, vol. 22, no. 8, pp. 4526–4532, 2020, doi: 10.1039/c9cp05147c.

[118] J. Chen, J. P. Ulerich, E. Abelev, A. Fasasi, C. B. Arnold, and W. O. Soboyejo, "An investigation of the initial attachment and orientation of osteoblast-like cells on laser grooved Ti-6Al-4V surfaces," *Mater. Sci. Eng. C*, vol. 29, no. 4, pp. 1442–1452, 2009, doi: 10.1016/j.msec.2008.11.014.